A Novel Methodology for Iterative Image Reconstruction in SPECT Using Deterministic Particle Transport

Katherine Royston

Dissertation submitted to the Faculty of the
Virginia Polytechnic Institute and State University
in partial fulfillment of the requirements for the degree of

Doctor of Philosophy
in
Nuclear Engineering

Alireza Haghighat, Chair
Yue J. Wang
Mark R. Paul
Kenneth H. Wong
Celine Hin
Ce Yi

March 23, 2015
Arlington, Virginia

Keywords: deterministic transport, SPECT, image reconstruction

A Novel Methodology for Iterative Image Reconstruction in SPECT Using Deterministic Particle Transport

Katherine Royston

ABSTRACT

Single photon emission computed tomography (SPECT) is used in a variety of medical procedures, including myocardial perfusion, bone metabolism, and thyroid function studies. In SPECT, the emissions of a radionuclide within a patient are counted at a gamma camera to form a 2-dimensional projection of the 3-dimensional radionuclide distribution within the patient. This unknown 3-dimensional source distribution can be reconstructed from many 2-dimensional projections obtained at different angles around the patient. This reconstruction can be improved by properly modeling the physics in the patient, i.e., particle absorption and scattering. Currently, such modeling is done using statistical Monte Carlo methods, but deterministic codes have the potential to offer fast computation speeds while fully modeling particle interactions within the patient. Deterministic codes are not susceptible to statistical uncertainty, but have been over-looked for applications to nuclear medicine, most likely due to their own limitations, including discretization and large memory requirements.

A novel deterministic reconstruction methodology for SPECT (DRS) has been developed to apply the advantages of deterministic algorithms to SPECT iterative image reconstruction. Using a maximum likelihood expectation maximization (ML-EM) algorithm, a deterministic code can fully model particle transport in the patient in the forward projection step, without the need of a large system matrix. The TITAN deterministic transport code has a SPECT formulation that allows for fast simulation of SPECT projection images and has been benchmarked through comparison with results from the SIMIND and MCNP5 Monte Carlo codes in this dissertation. The TITAN SPECT formulation has been improved through a modified collimator representation and full parallelization. The DRS methodology has been implemented in the TITAN code to create TITAN with Image Reconstruction (TITAN-IR). The TITAN-IR code has been used to successfully reconstruct the source distribution from SPECT data for the Jaszczak and NCAT phantoms. Extensive studies have been conducted to examine the sensitivity of TITAN-IR image quality to deterministic parameter selection as well as collimator blur and noise in the projection data being reconstructed. The TITAN-IR reconstruction has also been compared with other reconstruction algorithms. This novel image reconstruction methodology has been shown to reconstruct images in short computation times, demonstrating its potential in a clinical setting with further development.

Dedication

To my parents and my husband

Acknowledgements

I would like to express my gratitude to Dr. Alireza Haghighat, my advisor, for his patience and guidance in this work. His advice enabled me to successfully overcome the many obstacles I encountered. I thank my advisory committee for their time and feedback, especially Dr. Ce Yi for taking the time to work with me and provide vital assistance in the use of the TITAN code. I would like to thank my fellow graduate students, Will Walters and Nate Roskoff, for providing advice and discussion of problems as they arose as well as many a good laugh. My family deserves acknowledgement for their endless support and encouragement of my academic studies. My parents have taught me to always do my best and provided me with the skills to succeed. I would like to thank my husband Sean for always being there and having in faith in me.

Contents

List of Figures

List of Tables

Chapter 1

Introduction

Single photon emission computed tomography (SPECT) is a valuable nuclear medicine imaging modality used in a variety of diagnostic procedures, including the measurement of myocardial perfusion, bone metabolism, and thyroid function[1]. In the United States, there were over 7,200 facilities in 2011 performing nuclear medicine procedures[2]. In 2010, an estimated 17.0 million procedures were performed on SPECT or SPECT/CT systems and 31% of these were dedicated cardiac systems.

SPECT is described as a *functional* imaging technique, versus other techniques like CT that image anatomy. It involves the ingestion or injection of a radionuclide bound to a pharmaceutical, which is designed to localize in a particular part of the body. The emitted radiation is then detected to produce a 2-dimensional projection of the 3-dimensional radionuclide distribution in the body. A gamma camera is used to obtain projections at different angles around the patient. A collimator placed in front of the gamma camera

provides spatial resolution. These projection images can then be reconstructed to form a 3-dimensional image of the radionuclide distribution.

Of the various common imaging modalities, SPECT has the worst spatial resolution[3]. Spatial resolution in SPECT is primarily determined by the collimator resolution. Unfortunately there is a trade-off between collimator resolution and detector efficiency. Projection images also suffer from blur due to photons scattered into the acceptance angle of the collimator. Reconstruction algorithms that model these processes before detection are able to improve the reconstructed image quality. However, reconstruction algorithms with long computation times can not be of use in the clinic. Recently, iterative reconstruction techniques have become fast enough to become prominent in the clinic, but most research uses Monte Carlo methods to model radiation transport to the detector. In general, deterministic methods are faster than Monte Carlo methods and provide more detailed information about a system, but require large amounts of memory. With modern parallel computers, this memory requirement is less of a difficulty and so parallel deterministic methods have the potential to provide an alternative to Monte Carlo methods. However, exact modeling of the collimator is still not feasible in a traditional deterministic code due to the high number of spatial and angular meshes required.

In this dissertation, a hybrid deterministic particle transport formulation is developed for iterative reconstruction of SPECT projection images. The reconstruction utilizes the TITAN[4] parallel, hybrid, deterministic transport code, which has been developed to efficiently simulate SPECT projection images. The Deterministic Reconstruction

for SPECT (DRS) methodology was created to make use of the TITAN code's computation speed as the forward projector in an iterative reconstruction algorithm. The TITAN code was modified to perform iterative image reconstruction and the resulting code is referred to as TITAN-IR. The speed of TITAN-IR and the image quality of reconstructions are analyzed to determine the potential for use in a clinical setting.

A review of the literature is given in Chapter 2. It discusses SPECT background, image reconstruction background, SPECT simulation, and iterative reconstruction research. Relevant theory is discussed in Chapter 3. The SPECT algorithm in TITAN is analyzed in Chapter 4 and enhancements are made in Chapter 5. The DRS methodology is described and tested in Chapter 6. The TITAN-IR formulation is presented in Chapter 7 and analyzed in Chapter 8. Chapter 9 discusses conclusions and future work.

Chapter 2

Literature Review

2.1 SPECT Background

Following the discovery of x-rays in 1895 by Wilhelm Roentgen, radioactivity by Henri Becquerel in 1896 and radium by Marie Curie in 1898, diagnostic x-ray imaging was quickly established; however, the field of nuclear medicine required more time and advancements. Georg de Hevesy developed and applied the principles of radioactive tracers in the early 1900s[5]. The artificial production of new radionuclides became possible in the 1930s due to the invention of the cyclotron by Ernest Lawrence[6]. Imaging technology advanced greatly in the 1950s. In particular, the Anger camera, also called a gamma camera, was developed by Hal Anger in 1958[7] and would become the standard for SPECT image acquisition. The use of I-131 for thyroid disorders dominated nuclear medicine until Paul Harper *et al.* used Technetium-99m (Tc-99m) in 1964[8]. Tc-99m provided the flexibil-

ity for labeling different pharmaceuticals so that a variety of different organs could be imaged. It also had excellent gamma ray properties in that the 140-keV energy was high enough to escape the body and low enough to be easily detected. In 1957, the first Tc-99m generator had been developed at Brookhaven National Laboratory[9] and so Tc-99m could be readily supplied. This facilitated a rapid increase in nuclear medicine procedures.

In 1964, Kuhl and Edwards developed the first scanner to produce longitudinal and transverse section images of a patient[10]. Three years later Anger created the tomoscanner, which imaged planes at different depths in a patient using a mechanical method[11]. In the mid 1970s, the first SPECT devices with a single rotating head were created[12, 13], followed by multihead SPECT devices with noncircular orbits in the 1980s. SPECT has been combined with Computed Tomography (CT) and Magnetic Resonance Imaging (MRI) in order to correlate anatomical and functional information. Image fusion techniques using software were used in the 1980s and the first commercial SPECT/CT system was developed in 1999[14, 15]. In the last decade, small-animal SPECT and molecular imaging have become active areas of research into the mechanisms of disease and for the development of new radiopharmaceuticals[16].

2.2 Image Reconstruction Background

In SPECT, the detector, i.e., gamma camera, obtains the 2-dimensional (2-D) projection of the 3-dimensional (3-D) radionuclide distribution in the patient. The Radon transform[17] mathematically defines the projection operator as the integral of a function over straight

lines. This projection image contains no information about depth and may overlap activities from different patient structures. If several projection images are obtained at different angles around the patient, the 3-D radionuclide distribution can be reconstructed from the 2-D projection images. This problem can be expressed mathematically as

$$\mathbf{p} = \underline{\underline{A}}\,\mathbf{f}, \tag{2.1}$$

where $\mathbf{p}$ is the projection data vector, $\underline{\underline{A}}$ is the projection matrix operator (also known as the probability or system matrix), and $\mathbf{f}$ is the source vector. Direct methods to solve for $\mathbf{f}$ exist but are not used often because $\underline{\underline{A}}$ is generally ill-conditioned[18]. The two main types of image reconstruction methods are analytic and iterative.

The traditional standard for image reconstruction is filtered backprojection (FBP), which is an analytic method. Applications for FBP[19] and iterative methods[20] were both first described in the 1960s, but for decades FBP was used for its computational speed. Projection data is commonly represented as a sinogram. A sinogram is a matrix of projection data in which the horizontal axis corresponds to detector bin location and the vertical axis corresponds to projection angle. In simple backprojection, the detected counts are attributed to all voxels in the patient that project onto the detector bin, which results in a blurred reconstructed image. To correct for this blur, in FBP the Fourier transform of the sinogram is first filtered using a ramp filter, which reduces the amplitude of low-frequency components, and then backprojected. While this does enhance sharp edges in

the image, i.e., high-frequency components, it also enhances the high frequency noise. Other filters can be used to help with this, but at the cost of spatial resolution.

Iterative reconstruction methods estimate the solution and compare the resulting projections with the measured projections. Based on the comparison, the solution estimate is then modified and the process is repeated. Each iterative reconstruction method has a criterion for selecting the best solution and an algorithm to calculate it. Iterative reconstruction methods gained popularity during the 80s and 90s. While initially too time consuming, as computer advances were made, these methods became more attractive. Iterative reconstruction techniques are now primarily used instead of analytic reconstruction for emission tomography in the clinic[16]. Iterative reconstruction algorithms can be grouped into constraint-based and statistical reconstruction techniques.

The algebraic reconstruction technique (ART)[21] (also known as the Kaczmarz method) is what constraint-based methods are generally known as. In the basic additive form of ART, Eq. 2.2, a new estimate of the source distribution is found by adding a correction term to the current estimate.

$$f_j^{(k+1)} = f_j^{(k)} + \frac{p_i - \sum_{j=1}^{N} f_{ji}^{(k)}}{N} \tag{2.2}$$

In Eq. 2.2, p_i is the projection data along ray i, $f_j^{(k)}$ and $f_j^{(k+1)}$ are the current and new estimates, and $\sum_{j=1}^{N} f_{ji}^{(k)}$ is the sum of the counts along ray i. Note that one projection ray at a time is considered and the correction term is the difference between the measured projection and the current estimate. There are many different versions of ART algorithms,

e.g., simultaneous iterative reconstruction technique (SIRT)[22] and multiplicative algebraic reconstruction technique (MART)[21].

Statistical reconstruction methods are currently the most popular for emission tomography and of these the maximum likelihood expectation maximization[23, 24] (ML-EM) and ordered subsets expectation maximization[25] (OS-EM) algorithms dominate[26]. The ML-EM algorithm seeks to maximize the probability that a source distribution would result in the observed projection images. OS-EM is an accelerated ML-EM algorithm in which the projections are divided into subsets and a full iteration is complete once all subsets are done. One subset is used for each sub-iteration so that fewer forward projections are required for each full iteration. This reduces reconstruction time by approximately the number of subsets while giving comparable image quality to ML-EM.

Like analytic methods, iterative reconstruction techniques have both advantages and disadvantages. One advantage of ML-EM algorithms is the use of Poisson statistics. The raw data obtained from SPECT contains Poisson noise and the inclusion of the Poisson nature of SPECT projection data allows iterative reconstruction to perform better than analytical algorithms in low count situations[27]. Iterative reconstruction methods also allow for improved modeling of the image acquisition process. Disadvantages include increasing noise for a high number of iterations, possible position-dependent convergence rates, and long calculation times.

2.3 SPECT Simulation and Reconstruction Codes

While there has been much research involving the simulation of SPECT, the focus has been primarily on Monte Carlo methods. Several Monte Carlo codes have been specifically designed to simulate SPECT, including GATE[28], SimSPECT[29], SimSET[30], and SIMIND[31]. GATE (Geant4 Application for Tomographic Emission) is based on the Geant4[32] software toolkit for the simulation of the passage of particles through matter and supports Positron Emission Tomography (PET), SPECT, CT, and radiotherapy experiment simulations. SimSPECT is based on the MCNP[33] Monte Carlo code. SIMIND was developed by Professor Michael Ljungberg and describes a standard clinical SPECT camera. Codes optimized for specific simulations, e.g., SIMIND, have the advantage of being much faster; however, they may also be difficult to modify or give limited output, e.g., SIMIND does not give uncertainties at this time.

Others have developed complex analytical methods based on the Klein-Nishina scatter equations for SPECT simulation[34, 35]. These methods usually are restricted in the scattering order and geometry detail that can be modeled.

There are also some codes available for SPECT image reconstruction. Mathwork's MATLAB includes a FBP function and the Image Reconstruction Toolbox[36] for MATLAB includes FBP, ML-EM, and OS-EM algorithms. The QSPECT open-source software[37] was designed to provide a freely available application that includes the standard ML-EM and OS-EM reconstruction algorithms and a system matrix calculation. STIR (Software for Tomographic Image Reconstruction)[38] is an open-source object-oriented library for PET

image reconstruction that has recently been extended to SPECT[39]. GPU-accelerated reconstruction tools for emission and transmission computed tomography are available with NiftyRec[40], which has MATLAB and Python interfaces.

2.4 Iterative Reconstruction Research

Iterative reconstruction techniques have overtaken FBP as the most popular technique in the clinic for emission tomography, but there is still plenty of room for their improvement. Current research in iterative image reconstruction emphasizes the optimization of algorithms while improving the accuracy of the models incorporated into them[26]. The application of iterative reconstruction algorithms to CT, for which FBP is still the preferred algorithm, is under active investigation[41]. There is also ongoing research into solving for motion during reconstruction, as well as simultaneous reconstruction of both the emission and attenuation distributions from emission data only. Consistent procedures for evaluating the wide variety of reconstruction algorithms are needed to help move research into the clinic and this is therefore an important area of development.

The noise in statistical methods increases with each iteration due to the noisy projection data and early stopping or post-reconstruction smoothing is frequently used to control this. Clearly, stopping at a lower number of iterations is not ideal since not all of the image volume may have converged. Smoothing can result in a loss of resolution, but is widely available and well understood. Bayesian algorithms have been used to introduce a 'prior' term in the maximum a-posteriori (MAP) algorithm using a one-step-

late process[42] that very closely resembles the ML-EM algorithm. The algorithm has an additional term to penalize noise and current research seeks to optimize the penalty term and its weighting constant[26].

In making the models more exact, the modeling of scatter is a particularly active area of research. If only attenuation is considered during reconstruction, i.e., projections are assumed to contain uncollided particles only, the activity distribution in the patient is over-estimated because the scatter counts contribute to the measured projections. Scatter causes blurring in projections, reduces contrast, and increases quantification uncertainty. However, a recent review by Hutton *et al* found that only basic scatter correction methods have made it into regular usage[43]. All methods must balance making a more exact model against increased computation time.

Incorporating scatter correction into reconstruction can be achieved by taking measurements, modeling the scatter, or a combination of both. The most common measurement-based scatter correction methods involve using narrow energy windows to estimate the scatter. Recently much development has been seen in modeling scatter with the help of advances in computing. Studies have shown improvement for accurate modeling of scatter over energy window-based scatter correction methods[44, 45]. Modeling does have the disadvantage of not including contributions from activity located outside of the reconstructed volume, e.g., the liver in cardiac imaging, but this issue is being worked on[46]. Methods have been developed that use scatter functions created from experimental measurements or Monte Carlo simulations of a slab of water and these were extended

into the effective scatter source estimation (ESSE)[47]. Good results have been seen with the ESSE method, but it does neglect photon transport from the source to the point of scatter. Full Monte Carlo simulation of patient scatter has recently become possible for iterative image reconstruction with the development of optimization methods[48]. One of these optimizations is convolution forced detection (CFD), which significantly reduces the number of photon histories necessary to produce a low-noise simulation[49].

The ML-EM algorithm can be viewed as a series of ”forward” projections and backprojections. In dual matrix ML-EM reconstruction, less detail is modeled in the backprojection than in the forward projection to reduce computation time. Modeling scatter in the forward projection only has been shown to give nearly the same signal-to-noise properties as including the scatter model in the backprojection step as well[44]. Zeng and Gullberg investigated the theoretical implications of using mismatched projectors and conducted studies[50]. They concluded that, while theoretically a valid backprojector should be chosen based on their criteria, in practical applications with noise present the choice of a valid backprojector is not crucial and initial convergent behavior with a method to stop the iteration process is more important.

In a review of the literature, no mention was found of the use of a deterministic code to solve the linear Boltzmann equation, with the analytic models being the closest comparison. Hutton *et al* comment that if accurate scatter models can be directly integrated into reconstruction the range of photon energies used could be widened and result in an improvement in the signal-to-noise ratio[43].

Chapter 3

Theory

Here, the theory pertaining to this work is discussed. The linear Boltzmann equation is described, the theory behind the TITAN code system is given with emphasis on pertinent features, the ML-EM reconstruction algorithm is explained, and a novel deterministic reconstruction methodology is introduced.

3.1 Solving the Linear Boltzmann Equation

The linear Boltzmann equation (LBE), also known as the transport equation, describes neutral particles in a system and is derived from the Boltzmann equation with the assumption that particle-particle interactions are negligible relative to particle-nucleus interactions. The time-independent integro-differential form of the LBE for a non-

multiplying medium is given in operator form by

$$H\psi(\vec{r}, E, \hat{\Omega}) = S(\vec{r}, E, \hat{\Omega}) \text{ in } V, \tag{3.1}$$
$$\text{where } H = \hat{\Omega} \cdot \nabla + \sigma_t(\vec{r}, E) - \int_0^\infty \mathrm{d}E' \int_{4\pi} \mathrm{d}\Omega' \sigma_s(\vec{r}, E' \to E, \hat{\Omega}' \to \hat{\Omega}).$$

In Eq. 3.1, ψ is the angular flux, σ_t is the macroscopic total cross-section, $\sigma_s(\vec{r}, E' \to E, \hat{\Omega}' \to \hat{\Omega})$ is the macroscopic differential scattering cross-section, and S is the independent source. The LBE is derived from a balance of particles in a phase space composed of spatial, energy, and angular domains ($\mathrm{d}^3r\mathrm{d}E\mathrm{d}\Omega$). The first two terms in H are the loss of particles from the differential volume in the phase space due to streaming and collision, respectively. The third term in H and S are gains of particles into the differential volume in the phase space due to the scattering source and independent source, respectively.

Deterministic codes solve the LBE numerically by discretizing the phase space. The energy domain is discretized using the multigroup approximation[51] and the angular domain is discretized using the numerical quadrature technique[52]. The spatial domain discretization can vary based on the method; two of the most common numerical methods are the discrete ordinates method (S_N) and the method of characteristics (MOC). In the S_N method, the spatial domain is divided into meshes and numerical differencing schemes are required to evaluate the streaming term of the LBE. The MOC uses arbitrarily-shaped material regions and solves the LBE along characteristic rays (straight, parallel lines) using the integral form of the LBE. Both methods solve for the angular flux along discrete directions. These directions and their associated weights make up the quadrature set and

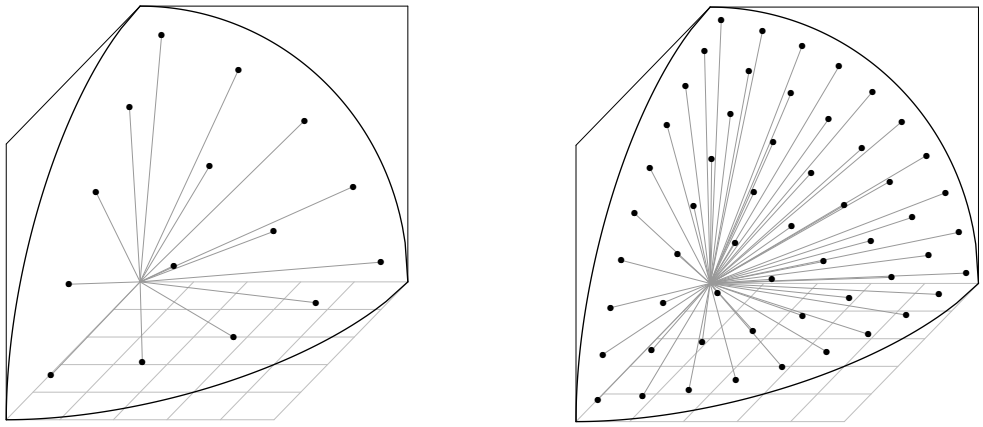

(a) S_{10} (120 directions) (b) S_{20} (440 directions)

Figure 3.1: Schematics of the directions in a quadrature set in one octant

are chosen to conserve flux moments, e.g., the zeroth moment or scalar flux as in Eq. 3.2:

$$\phi = \int_{4\pi} d\Omega \psi(\Omega) \cong \sum_{m=1}^{M} w_m \psi_m, \tag{3.2}$$

where ϕ is the scalar flux, ψ is the angular flux, and w_m is the m^{th} direction weight of M total directions. As an example, the directions in one octant of S_{10} and S_{20} quadrature sets are given in Fig. 3.1 as points on a unit sphere. For a quadrature order N, there are $M = N(N+2)$ directions in the quadrature set.

To develop the discrete ordinates formulation, the multigroup approximation is applied to Eq. 3.1 and the scattering source term is moved to the right-hand side and

written in terms of spherical harmonics to give the formulation of the LBE in Eq. 3.3.

$$\begin{aligned}&\left(\mu\frac{\partial}{\partial x}+\eta\frac{\partial}{\partial y}+\xi\frac{\partial}{\partial z}\right)\psi_g(x,y,z,\mu,\varphi)+\sigma_g(x,y,z)\psi_g(x,y,z,\mu,\varphi)=\\&\sum_{g'=1}^{G}\sum_{l=0}^{L}(2l+1)\sigma_{s,g'\rightarrow g,l}(x,y,z)\Bigg\{P_l(\mu)\phi_{g',l}(x,y,z)+\\&2\sum_{k=1}^{l}\frac{(l-k)!}{(l+k)!}P_l^k(\mu)\times\left[\phi^k_{Cg',l}(x,y,z)cos(k\varphi)+\phi^k_{Sg',l}(x,y,z)sin(k\varphi)\right]\Bigg\}+\\&S_g(x,y,z,\mu,\varphi)\end{aligned}\tag{3.3}$$

In Eq. 3.3, θ and φ are the polar and azimuthal angles, respectively, and a discrete ordinate is specified by (θ,φ) or (μ,η,ξ), where $\mu=cos(\theta)$, $\eta=sin(\theta)cos(\varphi)$, and $\xi=sin(\theta)sin(\varphi)$. $P_l(\mu)$ is the l^{th} Legendre polynomial and L is the Legendre expansion order. $P_l^k(\mu)$ is the l^{th},k^{th} associated Legendre polynomial. $\psi_g(x,y,z,\mu,\varphi)$ is the group g angular flux, G is the total number of energy groups, σ_g is the group macroscopic total cross-section, $\sigma_{s,g'\rightarrow g,l}$ is the l^{th} moment of the macroscopic differential scattering cross-section from group g' to g, and S_g is the independent fixed source. The flux moments are defined by

$$\phi_{g',l}(x,y,z)=\int_{-1}^{1}\frac{d\mu'}{2}P_l(\mu')\int_0^{2\pi}\frac{d\varphi'}{2\pi}\psi_{g'}(x,y,z,\mu',\varphi')\tag{3.4}$$

$$\phi^k_{Cg',l}(x,y,z)=\int_{-1}^{1}\frac{d\mu'}{2}P_l^k(\mu')\int_0^{2\pi}\frac{d\varphi'}{2\pi}cos(k\varphi')\psi_{g'}(x,y,z,\mu',\varphi')\tag{3.5}$$

$$\phi^k_{Sg',l}(x,y,z)=\int_{-1}^{1}\frac{d\mu'}{2}P_l^k(\mu')\int_0^{2\pi}\frac{d\varphi'}{2\pi}sin(k\varphi')\psi_{g'}(x,y,z,\mu',\varphi'),\tag{3.6}$$

where $\phi_{g',l}$ is the l^{th} Legendre flux moment for group g', $\phi^k_{Cg',l}$ is the l^{th},k^{th} cosine associated Legendre flux moment for group g', and $\phi^k_{Sg',l}$ is the l^{th},k^{th} sine associated Legendre

flux moment for group g'. Eq. 3.3 has energy and angular discretization since the angular flux is solved for energy group g in discrete directions (μ_n, ϕ_n) from the quadrature set of N total directions.

The spatial variable is discretized using the finite volume method[52] by integrating Eq. 3.3 over the fine mesh volume $V_{ijk} = \Delta x \Delta y \Delta z$ to form

$$\frac{\mu_n}{\Delta x}\left(\psi_{x,out} - \psi_{x,in}\right) + \frac{\eta_n}{\Delta y}\left(\psi_{y,out} - \psi_{y,in}\right) + \frac{\xi_n}{\Delta z}\left(\psi_{z,out} - \psi_{z,in}\right) + \sigma_{ijk}\psi^{(n)}_{gijk} = Q^{(n)}_{gijk}, \quad (3.7)$$

where $Q^{(n)}_{gijk} = S^{(n)}_{scat,gijk} + S^{(n)}_{gijk}$. In Eq. 3.7, $\psi_{x,in}, \psi_{y,in}$, and $\psi_{z,in}$ are the angular fluxes on the incoming boundaries of the fine mesh and $\psi_{x,out}, \psi_{y,out}$, and $\psi_{z,out}$ are the angular fluxes on the outgoing boundaries. $\psi^{(n)}_{gijk}$ is the average angular flux in fine mesh ijk along direction n for group g and $Q^{(n)}_{gijk}$ is the average angular source.

While the differential is removed, there are now additional unknowns in Eq. 3.7. The three incoming fluxes are obtained from boundary conditions and so three additional equations are needed to solve for $\psi^{(n)}_{gijk}$. These additional equations are provided by the chosen differencing scheme. The linear diamond differencing (DD) scheme is one of the simplest and is given by

$$\begin{aligned} \psi_{x,out} &= 2\psi_{x,in} - \psi^{(n)}_{gijk}, \\ \psi_{y,out} &= 2\psi_{y,in} - \psi^{(n)}_{gijk}, \\ \text{and } \psi_{z,out} &= 2\psi_{z,in} - \psi^{(n)}_{gijk}. \end{aligned} \quad (3.8)$$

The DD scheme assumes that the average flux is given by a linear average of the boundary fluxes. However, the DD scheme can give negative fluxes and for this reason is usually implemented with the zero fix-up approach and referred to as the DDZ scheme.

The LBE can be solved using the source iteration method. The source Q is calculated from the last iteration's results and taken as a constant while solving Eq. 3.7 for the angular flux ψ. The flux moments are then obtained from Eqs. 3.4-3.6 and used to update the source Q for the next iteration. This process is repeated until some convergence criterion is met, generally convergence of the 0^{th} flux moment, i.e., the scalar flux.

Deterministic methods can have numerical issues that lead to what are referred to as *ray effects* and *unphysical oscillations*. In situations with localized sources and little scatter, the uncollided flux is dominant and deterministic methods can result in oscillations in the scalar flux that are called ray effects[52]. Ray effects arise when the quadrature set cannot adequately approximate the scalar flux from the angular flux, as in Eq. 3.2. The simplest solution is to increase the quadrature order, i.e., the number of directions. Unphysical oscillations arise at source discontinuities from the differencing scheme not taking particle direction into account when obtaining coefficients for each axis[53].

As briefly mentioned earlier, the MOC is another popular method for solving the LBE. Unlike, the S_N formulation, the MOC can represent the model geometry exactly by filling arbitrarily shaped regions with characteristic rays along the directions of a quadrature set. The LBE along characteristic ray k in region i, energy group g, and direction n is

given by

$$\frac{d\psi_{gik}^{(n)}(l)}{dl} + \sigma_{gi}\psi_{gik}^{(n)}(l) = Q_{gi}^{(n)}. \tag{3.9}$$

In Eq. 3.9, l is the path length along characteristic ray k and constant cross sections and source are assumed within a region. If the incoming angular flux is known, Eq. 3.9 can be solved analytically. The angular flux out of region i is then calculated by

$$\psi_{gik,out}^{(n)} = \psi_{gik}^{(n)}(s_{ik}^{(n)}) = \psi_{gik,in}^{(n)} e^{-\sigma_{gi}s_{ik}^{(n)}} + \frac{Q_{gi}^{(n)}}{\sigma_{gi}}\left(1 - e^{-\sigma_{gi}s_{ik}^{(n)}}\right), \tag{3.10}$$

where $s_{ik}^{(n)}$ is the path length of ray k. For each region, the average angular flux is found by filling the region with characteristic rays along the quadrature set directions and taking a weighted average. The source iteration method can also be used with the MOC. To get accurate results, the flux must change slowly over the region and enough characteristic rays must be modeled to cover the region. The MOC method is also susceptible to ray effects, but is numerically more efficient in low scatter regions[4].

3.2 The TITAN Code

3.2.1 Hybrid Formulation

The TITAN code is a hybrid deterministic transport code that numerically solves the linear Boltzmann equation (LBE) for neutral particles[54]. The source iteration method described in Section 3.1 is implemented in TITAN as shown in Fig. 3.2 for a single energy

group and fixed source S_0. The transport sweep solves for the angular flux distribution, which is then used to obtain the scalar flux and calculate the flux moments. The flux moments are used to update the scattering source S_{scat} and add it to the total source Q and the process is then repeated.

The TITAN code is a "hybrid" code because it allows the use of different solvers in the spatial domain with its multi-block framework. In different regions (called coarse meshes) of a problem, the user can specify a discrete ordinates[52] (S_N) solver or a characteristics method[55] (CM) solver. There are two differencing schemes available in the TITAN code: diamond differencing with zero fix-up (DDZ) and directional theta-weighted (DTW)[56]. The CM discretizes the angular domain as in the S_N method, but instead of using spatial meshes, the integral form of the LBE is used to calculate the angular flux along parallel directions called characteristic rays. The CM does not require the use of a differencing scheme, but still can be memory intensive because of the need for a large set of characteristic rays.

3.2.2 Parallel Implementation

Parallel performance has become a vital attribute of modern algorithms in order for them to be applied to real-world problems. The TITAN code is parallelized by angular decomposition of individual ordinates, i.e., directions, in that each processor is assigned a set of ordinates and stores only those ordinates to partition memory. In each iteration in Fig. 3.2, a transport sweep is performed on each processor for its set of ordinates and

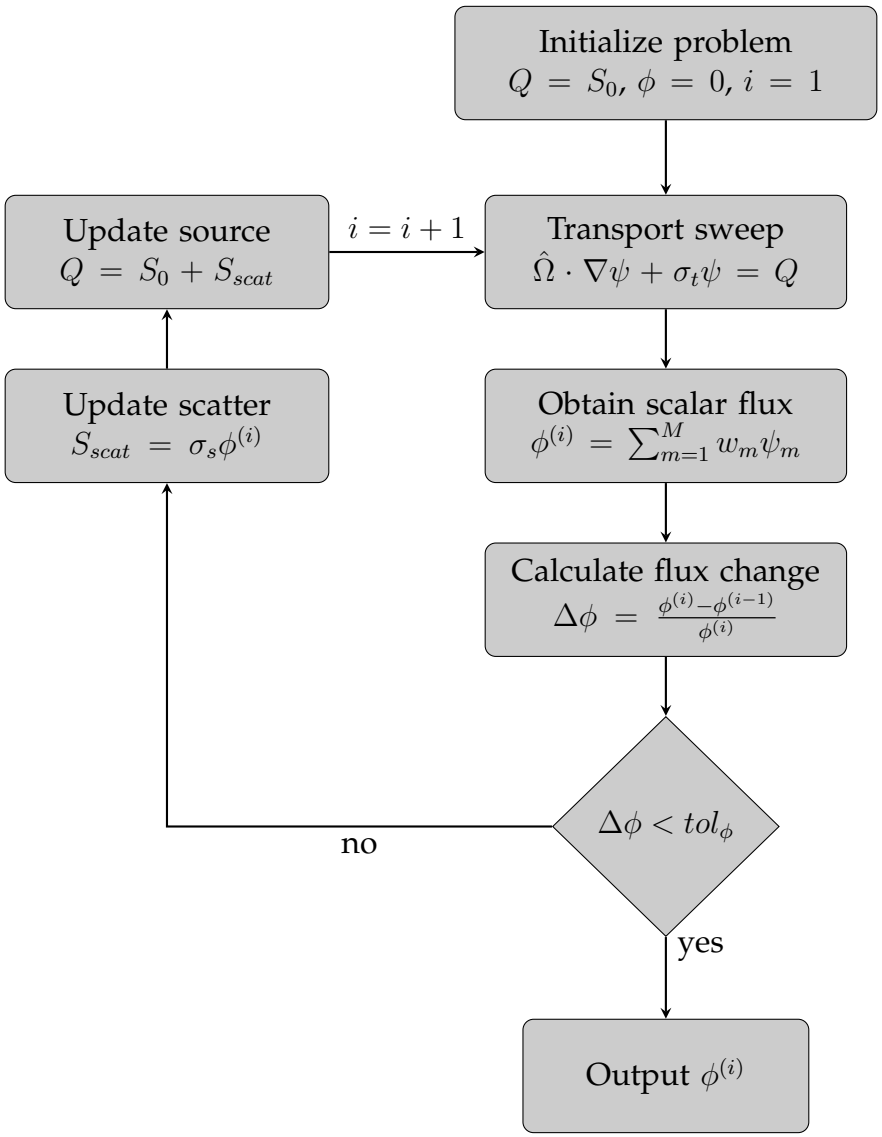

Figure 3.2: Source iteration in the TITAN code

the corresponding flux moments are calculated. At the end of the iteration, all processors communicate using MPI (Message Passing Interface) and the flux moments from all subsets are combined to get the total flux moments. If reflective boundary conditions are present, the number of processors is limited to the number of ordinates per octant, Fig. 3.1, so that all possible reflections of an ordinate to another octant are stored on the same processor. This allows reflective boundary conditions to be applied without any additional communication.

3.2.3 SPECT Formulation

To simulate SPECT, the TITAN code uses a four step hybrid S_N and simplified ray-tracing formulation[57]:

1. S_N transport calculation in the phantom, or patient, with a regular quadrature set
2. Generation of fictitious quadrature set[57] with circular ordinate splitting for a projection angle
3. One extra transport sweep in the phantom with the fictitious quadrature set using the converged flux moments from *Step 1* to evaluate the scattering source
4. Simulation of the projection image with the fictitious quadrature set using the simplified ray-tracing formulation outside of the phantom.

Step 1 only needs to be completed once and *Steps 2-4* are then repeated for each projection angle desired. Each voxel of the phantom is modeled as a fine mesh in TITAN. In *Step*

2, the fictitious quadrature set is created to represent the projection directions needed for a specific SPECT projection image. Fig. 3.3 demonstrates a fictitious quadrature set with forty projection angles and eight split directions per projection angle.

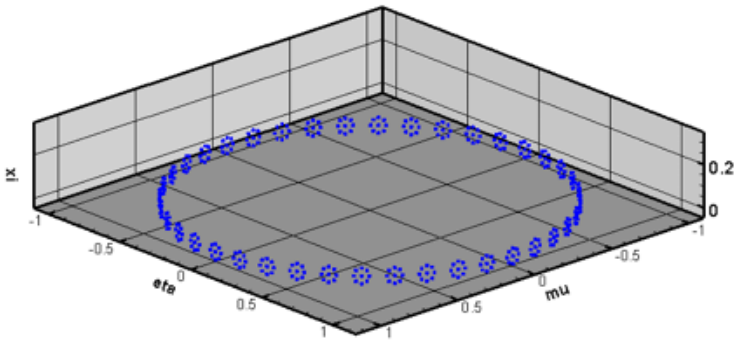

Figure 3.3: Example schematic of a fictitious quadrature set with circular ordinate splitting.

The ordinate splitting technique[58] was adapted in the TITAN code for use in simulating the collimator in SPECT to create the circular ordinate splitting (COS) technique. It is not reasonable to directly model the SPECT collimator due to the fine spatial and angular discretization that would be required. The COS technique is used to represent an acceptance angle about the detector normal within which incoming photons will reach the detector without interacting with the collimator. In the COS technique, split directions are made on a circle, or concentric circles, centered on the original projection direction, as depicted in Figs. 3.3 and 3.4. The radius of the outermost circle is chosen to match the desired collimator acceptance angle. The angular fluxes over the original and split directions are averaged to simulate the flux passing through the collimator.

The fictitious quadrature set is created to calculate the angular fluxes for certain directions and does not require flux moments to be conserved as in a regular quadrature

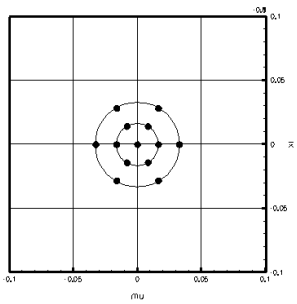

Figure 3.4: Circular ordinate splitting (COS) with 2 circles and 6 directions per circle.

set. Therefore, in *Step 3*, the scattering source and flux moments cannot be properly handled with a regular transport sweep. After the flux moments are converged in *Step 1*, the scattering source for the directions in the fictitious quadrature set is evaluated by Eq. 3.11.

$$S^{(e.s.)}_{scattering} = \sum_{g'=1}^{G}\sum_{l=0}^{L}(2l+1)\sigma_{s,g'\rightarrow g,l}\Bigg\{ P_l(\mu_n^{(fic)})\phi^{(con)}_{g',l} + 2\sum_{k=1}^{l}\frac{(l-k)!}{(l+k)!}P_l^k(\mu_n^{(fic)}) \times \left[\phi^{k,(con)}_{Cg',l}cos(k\varphi_n^{(fic)}) + \phi^{k,(con)}_{Sg',l}sin(k\varphi_n^{(fic)})\right]\Bigg\} \tag{3.11}$$

In Eq. 3.11, $(e.s.)$ indicates the *extra sweep*, (fic) refers to the *fictitious* quadrature set, and (con) is the *converged* flux moments. With the scattering source calculated, an extra sweep through the phantom is used to evaluate the angular fluxes in the fictitious quadrature directions. Note that the fictitious quadrature does not conserve flux moments and so the angular flux can no longer be directly related to the scalar flux.

In *Step 4*, particles are transported from the phantom surface, through the collimator holes, and to the detector using the simplified ray-tracing formulation. The simplified formulation uses the backward ray-tracing approach from the TITAN code's characteristics solver and assumes vacuum outside of the phantom. Characteristic rays are drawn

from each image pixel backward to the phantom surface along the projection angle and the split directions. Where a ray intersects with the phantom surface, the angular flux has already been calculated for the direction in *Step 3* and a bi-linear interpolation is used to evaluate the angular flux at that intersection point.

3.3 ML-EM Reconstruction

The simplified derivation of the maximum likelihood expectation maximization (ML-EM) formulation that follows is based on Bruyant's explanation in ref. 18. The ML-EM algorithm assumes that the number of emitted particles and detected particles are both Poisson random variables. Therefore the probability of detecting k counts in detector bin d is

$$P(n_d = k) = e^{-\bar{n}_d} \frac{\bar{n}_d^k}{k!}, \tag{3.12}$$

where $\bar{n}_d$ is the mean number of photons detected in bin d given by

$$\bar{n}_d = \sum_{b=1}^{B} p_{b,d} \bar{\lambda}_b. \tag{3.13}$$

In Eq. 3.13, $p_{b,d}$ is the probability that a photon emitted from voxel b is detected in detector bin d and $\bar{\lambda}_b$ is the mean number of emissions in voxel b for $b = 1, \ldots, B$ voxels and $d = 1, \ldots, D$ bins.

The likelihood, $L(\bar{\boldsymbol{\lambda}})$, is the conditional probability $P(\mathbf{n}|\bar{\boldsymbol{\lambda}})$ of observing $\mathbf{n}$ if the emission rate is $\bar{\boldsymbol{\lambda}}$. For D detector bins, the Poisson variables are independent and so the conditional probability is the product of the individual probabilities. Using Eq. 3.12, the

likelihood function is given by

$$L(\bar{\boldsymbol{\lambda}}) = P(\mathbf{n}|\boldsymbol{\lambda}) = \prod_{d=1}^{D} P(n_d) = \prod_{d=1}^{D} e^{-\bar{n}_d} \frac{\bar{n}_d^{n_d}}{n_d!}. \tag{3.14}$$

At this point, the natural logarithm of the likelihood function is taken to simplify the derivation. Recalling that $\ln(x_1 x_2 \dots x_n) = \ln(x_1) + \ln(x_2) + \cdots + \ln(x_n)$, the log-likelihood can be simplified to

$$l(\bar{\boldsymbol{\lambda}}) = \ln(L(\bar{\boldsymbol{\lambda}})) = \sum_{d=1}^{D} \ln\left(e^{-\bar{n}_d} \frac{\bar{n}_d^{n_d}}{n_d!}\right) = \sum_{d=1}^{D} \left[-\bar{n}_d + n_d \ln(\bar{n}_d) - \ln(n_d!)\right]. \tag{3.15}$$

Eq. 3.13 is now substituted into Eq. 3.15 to give

$$l(\bar{\boldsymbol{\lambda}}) = \sum_{d=1}^{D} \left[-\sum_{b=1}^{B} p_{b,d} \bar{\lambda}_b + n_d \ln(\sum_{b=1}^{B} p_{b,d} \bar{\lambda}_b) - \ln(n_d!) \right]. \tag{3.16}$$

Eq. 3.16 is the probability of observing a projection dataset $\mathbf{n}$ for mean image $\bar{\boldsymbol{\lambda}}$. The goal is to obtain the image that is most likely to produce $\mathbf{n}$ by finding the image $\bar{\boldsymbol{\lambda}}$ for which $l(\bar{\boldsymbol{\lambda}})$ is maximized. To find this maximum, the derivative of $l(\bar{\boldsymbol{\lambda}})$ is set to zero:

$$\frac{\partial l(\bar{\boldsymbol{\lambda}})}{\partial \bar{\lambda}_b} = -\sum_{d=1}^{D} p_{b,d} + \sum_{d=1}^{D} \frac{n_d}{\sum_{b'=1}^{B} p_{b',d} \bar{\lambda}_{b'}} p_{b,d} = 0. \tag{3.17}$$

Multiplying Eq. 3.17 by $\bar{\lambda}_b$ gives

$$-\bar{\lambda}_b \sum_{d=1}^{D} p_{b,d} + \bar{\lambda}_b \sum_{d=1}^{D} \frac{n_d}{\sum_{b'=1}^{B} p_{b',d} \bar{\lambda}_{b'}} p_{b,d} = 0, \tag{3.18}$$

which can then be rearranged to form

$$\bar{\lambda}_b = \frac{\bar{\lambda}_b}{\sum_{d=1}^{D} p_{b,d}} \sum_{d=1}^{D} \frac{n_d}{\sum_{b'=1}^{B} p_{b',d} \hat{\lambda}_{b'}} p_{b,d}. \tag{3.19}$$

Eq. 3.19 can be modified to give the iterative form of the ML-EM algorithm

$$\hat{\lambda}_b^{(i+1)} = \frac{\hat{\lambda}_b^{(i)}}{\sum_{d=1}^{D} p_{b,d}} \sum_{d=1}^{D} \frac{n_d^* p_{b,d}}{\sum_{b'=1}^{B} \hat{\lambda}_{b'}^{(i)} p_{b',d}}, \quad b = 1, \ldots, B, \tag{3.20}$$

where $\hat{\lambda}_b^{(i)}$ is the estimate of the unknown emission density in voxel b for iteration i, n_d^* is the measured data in detector pixel d, and $p_{b,d}$ is the probability or system matrix and gives the probability that an emission in voxel b is detected in detector pixel d.

3.4 Novel Deterministic Reconstruction Methodology

The ML-EM iterative algorithm given in Eq. 3.20 can be viewed as a series of projections and backprojections. The denominator $\sum_{b'=1}^{B} \hat{\lambda}_{b'}^{(i)} p_{b',d}$ is the projection of the current image estimate. Eq. 3.20 can then be rewritten as

$$\hat{\lambda}_b^{(i+1)} = \frac{\hat{\lambda}_b^{(i)}}{\sum_{d=1}^{D} p_{b,d}} \sum_{d=1}^{D} \frac{n_d^*}{n_d^{(i)}} p_{b,d}, \quad b = 1, \ldots, B, \tag{3.21}$$

where $n_d^{(i)}$ is the projection of the current estimate. The ratio of the measured projection data to the projection estimate is then backprojected so that Eq. 3.21 can be simplified into Eq. 3.22[18].

$$Emission^{(i+1)} = Emission^{(i)} \times Backprojection\ of \left(\frac{Measured\ Projections}{Estimated\ Projections} \right) \tag{3.22}$$

A deterministic code that generates projection images can then be used to provide the estimated projections. This methodology is referred to here as deterministic reconstruction for SPECT (DRS) and was developed to take advantage of the TITAN code's fast algorithm for simulating SPECT projection images.

DRS can be viewed as a modified version of dual matrix image reconstruction, in which different system matrices are used for the projection and backprojection steps. Dual matrix image reconstruction allows for the backprojection system matrix to model less detail than the "forward" projection system matrix to reduce reconstruction time. The system matrix can model attenuation, depth-dependent collimator response, and even scatter, but can become difficult to compute and prohibitively large with the addition of this detail. In DRS, a single system matrix is not used for projection and backprojection, but unlike dual matrix reconstruction only the simpler backprojection system matrix is needed. The deterministic code completes the projection step and is able to fully model particle transport, including scatter, in the patient or phantom without the need of a complicated system matrix.

Chapter 4

Analysis of SPECT Algorithm in TITAN

Studies were conducted to analyze the TITAN code for SPECT simulation before applying it to image reconstruction. TITAN projection images are compared with results from the SIMIND code, the MCNP5 code, and an experiment.

This work focuses on simulating a myocardial perfusion study using Technetium-99m (Tc-99m) and so a 140 keV photon source is used. Three-group multigroup cross sections generated using the CEPXS code[59] were used. The first energy group is 126.45-154.55 keV to account for a typical energy window of 20% and is the group of interest. The second energy group is 126.45-154.55 keV and the third is 10-126.45 keV. Projection images are normalized to the highest value pixel before comparison.

4.1 Projection Comparison with SIMIND

SPECT projection images generated by TITAN were compared with the SIMIND Monte Carlo code[60]. The NURBS-based cardiac-torso (NCAT) code[61] was used to generate a $64 \times 64 \times 64$ voxel phantom ($0.625 \times 0.625 \times 0.625\ cm^3$ voxel size) for use in both SIMIND and TITAN. The TITAN geometry for the NCAT phantom is shown in Fig. 4.1 with the the regions using the S_N and ray-tracing solvers indicated. A high intensity source was placed in the myocardium, i.e., heart muscle, and a low intensity source in the rest of the soft tissue to simulate Tc-99m uptake in the rest of the body.

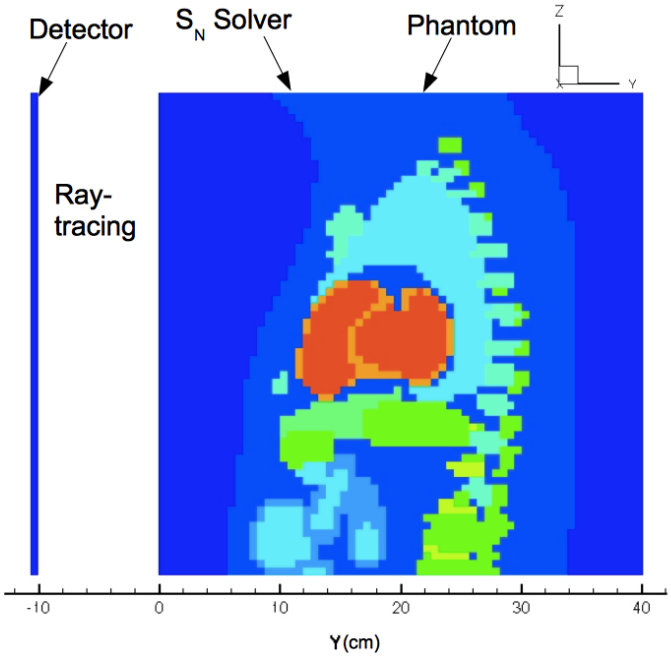

Figure 4.1: Sagittal slice through TITAN geometry on NCAT phantom with regions using the S_N and ray-tracing solvers indicated

Projection images were generated in both codes for anterior, left lateral, posterior, and right lateral views and are shown in Figs. 4.2 and 4.3 for SIMIND and TITAN, respec-

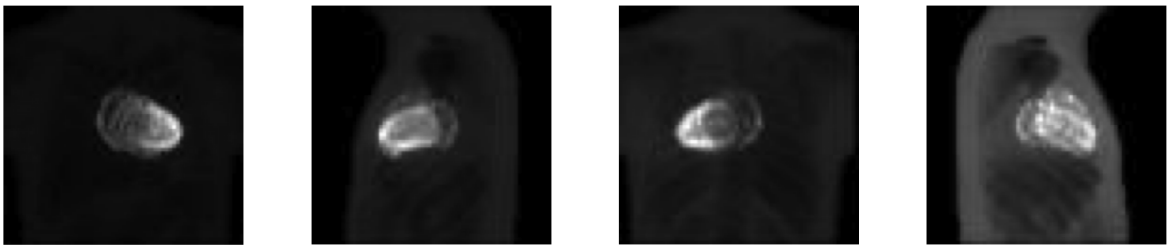

(a) (b) (c) (d)

Figure 4.2: Projection images generated by the SIMIND code for (a) anterior, (b) left lateral, (c) posterior, and (d) right lateral views

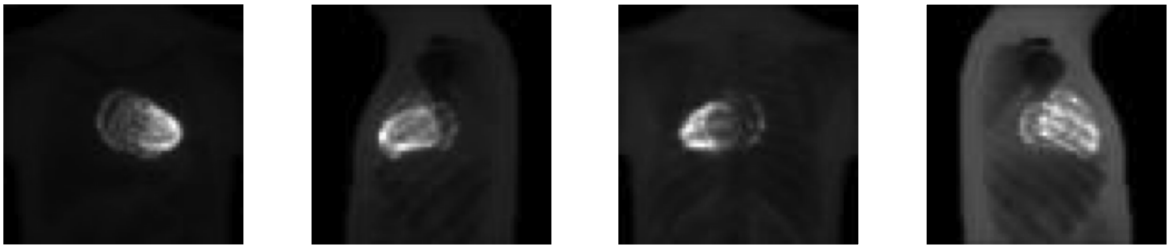

(a) (b) (c) (d)

Figure 4.3: Projection images generated by the TITAN code for (a) anterior, (b) left lateral, (c) posterior, and (d) right lateral views

tively. Visually, the TITAN projection images show excellent agreement with the SIMIND results for each view.

Examining profiles through the projection images verified that the normalized flux shape matched well, as seen in Fig. 4.4 for an anterior projection. Some differences in magnitude are observed, but the peaks line up in the TITAN and SIMIND results.

The projection images were numerically analyzed by comparing the high-count myocardium pixels in the normalized images. The maximum relative differences of the TITAN myocardium pixels relative to SIMIND are given in Table 4.1. In Table 4.1, significant differences are found between the two codes; however, the TITAN and SIMIND codes use different cross-section information so some differences are expected. Also, dif-

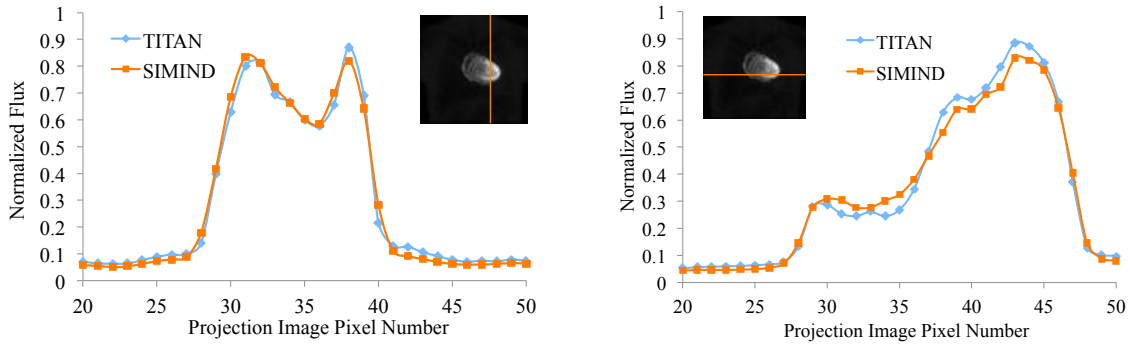

(a) (b)

Figure 4.4: (a) Vertical and (b) horizontal profiles through heart in anterior projections from TITAN and SIMIND.

ferent methods of representing collimation are used by the two codes. It is interesting to note that the largest relative differences are seen for the projection angles where the heart is deepest in the phantom. The SIMIND code has the user select a fixed number of photons to simulate per projection angle. This will result in fewer photons reaching the detector for the posterior and right lateral projections and therefore larger uncertainties in a Monte Carlo code like SIMIND.

Table 4.1: Maximum difference of TITAN results relative to SIMIND results for each projection

Anterior	Left Lateral	Posterior	Right Lateral
16.4%	-12.8%	-23.5%	-25.8%

The computation times of the SIMIND and TITAN codes for different numbers of projection angles on a single processor are compared in Table 4.2. The speed of the specialized SIMIND code is apparent for small numbers of projections; however, for the large numbers of projections that would be necessary for image reconstruction, the TITAN code shows a clear advantage over the SIMIND code. Recall from Section 3.2 that to simulate

SPECT projection images, TITAN completes the time-consuming phantom flux calculation once and is then able to generate the projection images at each angle with little additional computational cost. In contrast, the SIMIND code completes each projection angle calculation separately. The SIMIND results presented here used one million photons per projection image, but the SIMIND code does not output any statistical information about the solution. It is up to the user to verify that enough photons have been simulated and this has been done by plotting the infinity-norm and 2-norm as a function of photons simulated.

Table 4.2: SIMIND and TITAN computation times

Number of Projection Images	1	4	8	45	90
SIMIND Time (sec)	17	67	140	754	1508
TITAN Time (sec)	200	202	212	274	352

4.2 Projection Comparison with MCNP5

In a study[62] that focused on varying collimator acceptance angles, projection images generated by the TITAN code were compared with those generated by the MCNP5 Monte Carlo code. The NCAT code[61] was used to generate a voxel phantom for use in both codes, as in Section 4.1. The collimator acceptance angle of each case is given in Table 4.3.

Anterior projection images generated by the TITAN and MCNP5 codes can be visually compared for each collimator case in Figs. 4.5 and 4.6. For Case 1, the TITAN

Table 4.3: Collimator cases with different acceptance angles

Case number	Acceptance Angle
1	2.97°
2	1.42°
3	0.98°

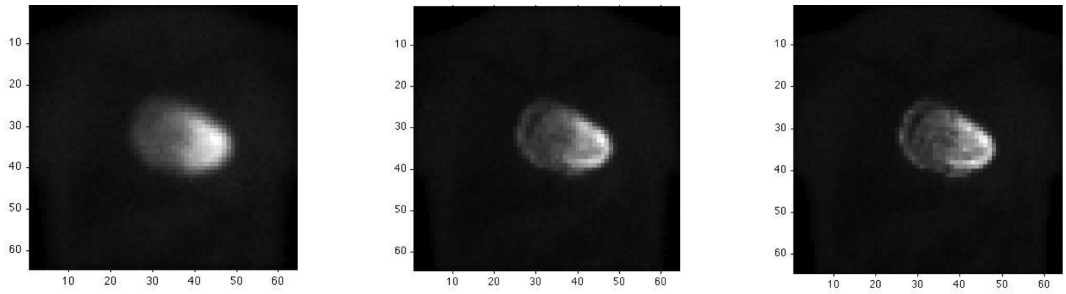

(a) Case 1 (b) Case 2 (c) Case 3

Figure 4.5: MCNP5 anterior projection images for collimator cases

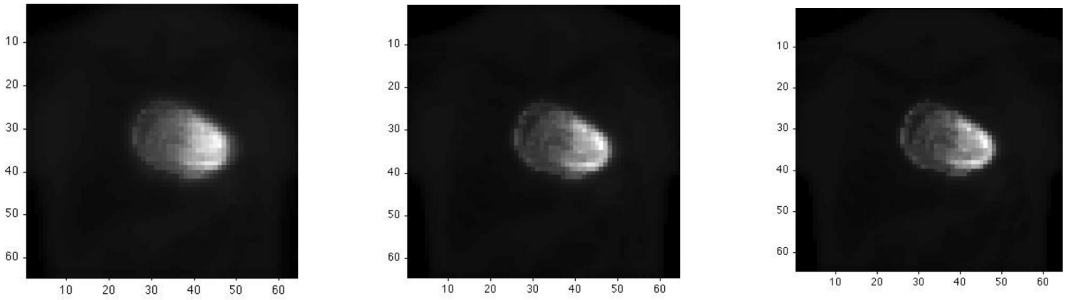

(a) Case 1 (b) Case 2 (c) Case 3

Figure 4.6: TITAN anterior projection images for collimator cases

image, Fig. 4.6a, appears less blurred than the MCNP5 image, Fig. 4.5a. As expected, the images become sharper as the acceptance angle decreases, i.e., the case number increases.

Table 4.4 gives the acceptance angle and maximum relative error in the heart corresponding to each collimator case. In Table 4.4, it is clear that the differences between the TITAN and MCNP5 projection images are reduced with decreasing acceptance angle.

This was attributed to limitations of the TITAN code's COS technique for simulating the collimator acceptance angle.

Table 4.4: Maximum difference of TITAN results relative to MCNP5 results for each collimator case

Case number	Acceptance Angle (degrees)	Maximum relative difference (%)
1	2.97	21.3
2	1.42	11.9
3	0.98	8.3

Profiles through the TITAN and MCNP5 projection images are plotted for each collimator case along with the relative difference in Figs. 4.7, 4.8, and 4.9. In Fig. 4.7a, discrepancies in the peak support the significant relative difference in Table 4.4. These are believed to be caused by the TITAN COS technique not creating sufficient collimator blur. As the collimator acceptance angle is reduced, Figs. 4.8a and 4.9a, the solutions match more closely.

The computation times for the TITAN and MCNP5 simulations are given in Table 4.5 for all three collimator cases on 16 processors. All simulations were performed on a PC-cluster using 2 nodes with 8 processors and 4 GB of RAM per node. The MCNP5 times are for a 1σ statistical uncertainty of $\leq 3.0\%$ in the heart and the TITAN times are for simulating 180 projection angles. The MCNP5 code simulated 3.6 billion, 13.6 billion, and 26.7 billion histories for Cases 1, 2, and 3, respectively, to achieve the aforementioned uncertainty. Even though a single detector position is being simulated in MCNP5, it would be possible to place detectors at other projection angles without significant change in the

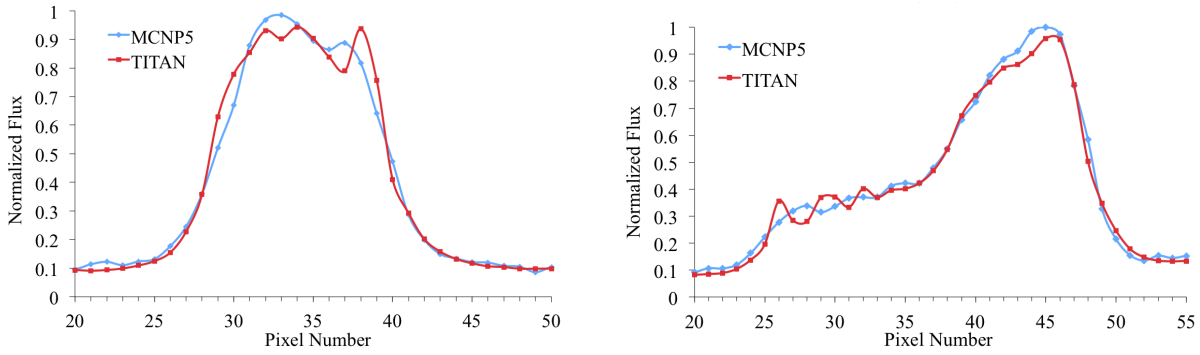

Figure 4.7: Case 1 profiles through MCNP5 and TITAN projection images: (a) vertical and (b) horizontal

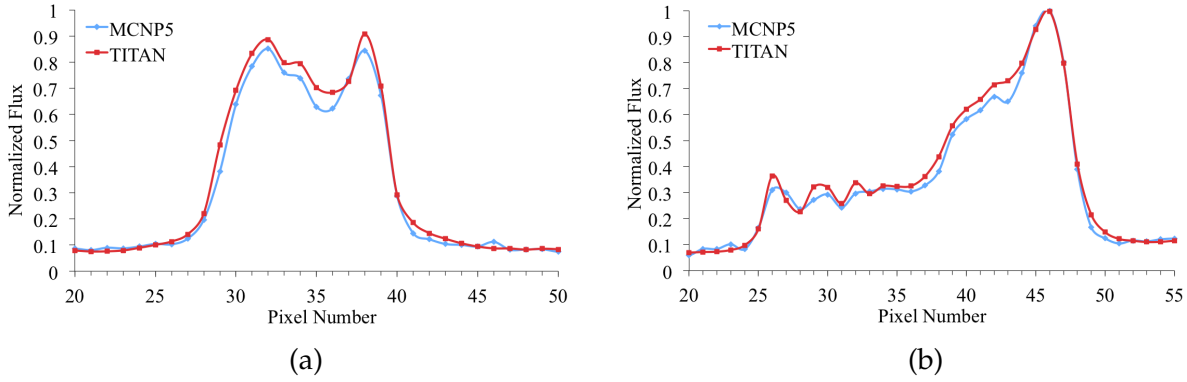

Figure 4.8: Case 2 profiles through MCNP5 and TITAN projection images: (a) vertical and (b) horizontal

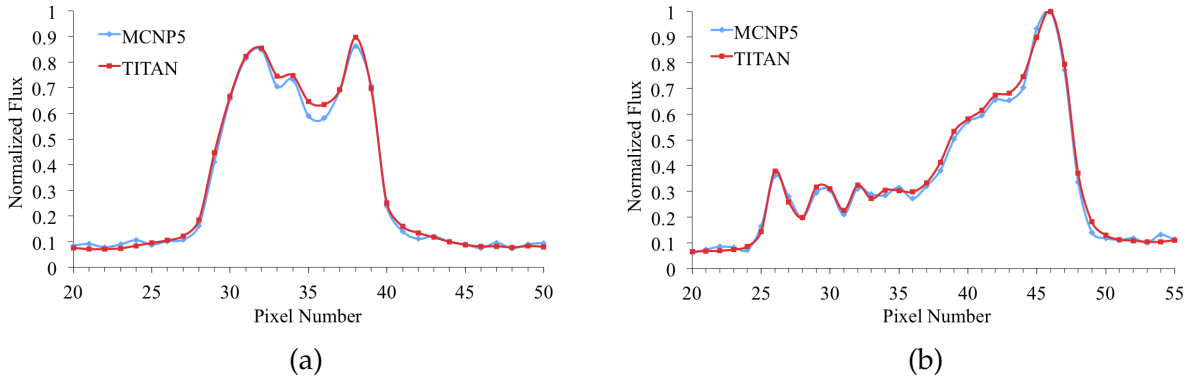

Figure 4.9: Case 3 profiles through MCNP5 and TITAN projection images: (a) vertical and (b) horizontal

calculation time. This is why 180 projection angles are being used in the TITAN simulation for the computation time comparison with MCNP5.

Table 4.5: Computation time comparison with MCNP5 and TITAN on 16 processors

Case number	Acceptance Angle (degrees)	MCNP5* (min)	TITAN† (min)	Speedup (MCNP5/TITAN)
1	2.97	313.8	0.82	382
2	1.42	1071.8	0.82	1304
3	0.98	2289.7	0.82	2787

* Time to achieve 1σ uncertainty of $\leq 3.0\%$ in the heart

† 180 projection angles

The results in Table 4.5 demonstrate an advantage of TITAN over MCNP5 in that a smaller collimator acceptance angle will not affect computation time in TITAN. As expected, in the MCNP5 code a significant increase in computation time is seen for smaller acceptance angles to achieve similar statistical uncertainties. For all cases, the TITAN code is significantly faster than MCNP5 with speedup factors ranging from 382 to 2,787.

4.3 Projection Comparison with Experiment

A study[60] comparing TITAN projection images with experimental SPECT data was done using the Data Spectrum Corporation's dynamic cardiac phantom. Tc-99m activities of 1 mCi and 2 mCi were placed in the myocardium and liver, respectively. The phantom was imaged using a prototype bedside cardiac SPECT system[63], Fig. 4.10, as well as by a CT machine to obtain a density distribution. The density distribution was contoured to

produce the voxel phantom used by the TITAN code, Fig.4.11. As an additional comparison, an MCNP5 model was created[64] using the same voxel phantom.

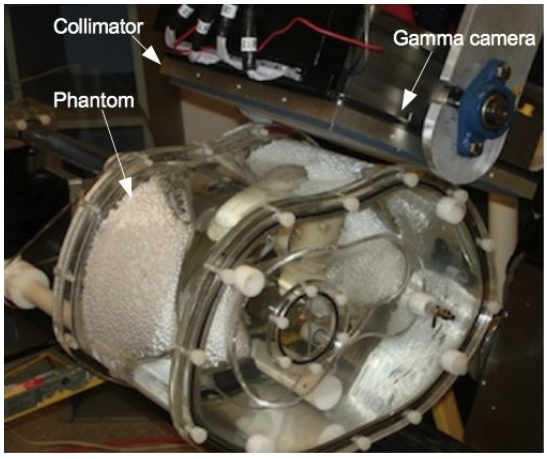

Figure 4.10: Dynamic cardiac phantom being imaged by a prototype bedside SPECT system.

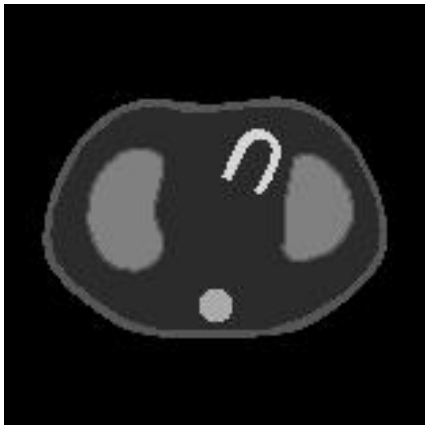

Figure 4.11: Slice through contoured CT scan of the dynamic cardiac phantom

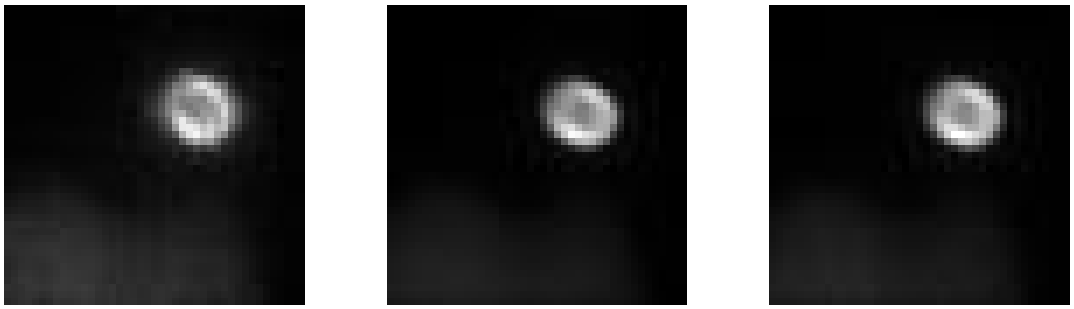

(a) Experiment (b) TITAN (c) MCNP5

Figure 4.12: Anterior projection images of the dynamic cardiac phantom.

Anterior projection images produced by the experiment, the TITAN code, and the MCNP5 code are given in Figure 4.12. Visual agreement is good between all three figures. When compared numerically, the TITAN anterior projection had a maximum difference in the myocardium of -10.0% relative to the MCNP5 projection and -20.7% relative to the experimental projection.

Profiles through the TITAN and MCNP5 images were examined[64] and matched well in shape, as seen in Figure 4.13a. Profiles through the TITAN and experiment anterior projections revealed that the size of the heart in the experiment was different from the voxel phantom used in the computation simulations. Figure 4.13b demonstrates this. Note that the heart in the phantom is rubber so that it can be used to simulate a beating heart and that the CT and SPECT images could not be obtained on the same day. It seems that the phantom was physically altered between the CT and SPECT image acquisitions. This limited the usefulness of the experiment and so it would be desirable to obtain new experimental data from a well-controlled environment.

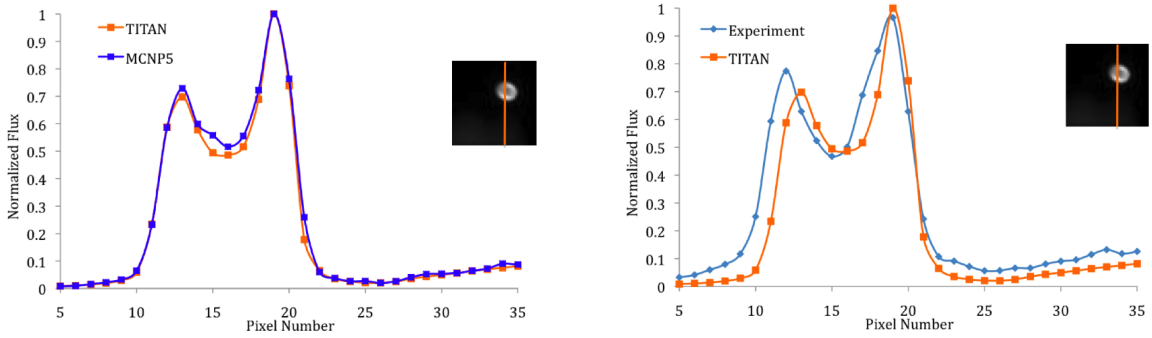

(a) TITAN and MCNP5 (b) TITAN and Experiment

Figure 4.13: Profiles through anterior projection images of the dynamic cardiac phantom

Chapter 5

Enhancement of SPECT Algorithm in TITAN

Two enhancements to the SPECT algorithm in TITAN are made in this section with regard to computation time and accuracy. The parallel behavior of the SPECT algorithm in TITAN is examined and improved. Based on the results of the collimator study in Chapter 4, improvements are made to the collimator representation in TITAN.

5.1 Parallel Computation

5.1.1 Parallel Processing Metrics

The parallel speedup, parallel efficiency, and parallelizable fraction can be calculated to give an indication of an algorithm's parallel performance. The parallel speedup (S_P) is

defined as the ratio of the wall-clock time for a single processor (T_s) to the wall-clock time in parallel. The parallel efficiency indicates the economic advantage of the parallelization and is the parallel speedup divided by the number of processors (P). Amdahl's Law[65] can be used to find the parallel fraction of a code by

$$S_P = \frac{1}{(1 - f_P) + f_P/P + T_c/T_s}, \tag{5.1}$$

where f_P is the parallelizable fraction of the code and T_c is the parallel communication time. If the parallel communication time is assumed to be much less than the serial computation time, Eq. 5.1 can be rewritten as

$$f_P = \frac{P(1 - S_P)}{S_P(1 - P)}. \tag{5.2}$$

The parallelizable fraction in Eq. 5.2 gives a lower limit on the actual parallelizable fraction.

Several factors impact and limit parallel performance. In the limit of infinite processors (and zero communication time), Eq. 5.1 gives $S_P = 1/(1 - f_P)$. However, this theoretical speedup will not be observed due to increasing communication overhead with the addition of processors, i.e., more processors will eventually lead to low efficiency. The load balance and granularity are also important to consider. Load balance refers to how evenly the work is distributed among processors. Granularity refers to the number of operations executed by processors before communication between them occurs.

5.1.2 Parallel Performance of SPECT Simulation

All of the following simulations were performed on a dedicated PC-cluster with 8 processors per compute node. Each processor is a 2 GHz Intel Xeon Quad Core processor with 4 GB of DDR2 SDRAM. Simulations are of the $64 \times 64 \times 64$ voxel NCAT phantom with collimator Case 1 from Section 4.2. The TITAN simulation uses S_6 quadrature.

The wall-clock time, parallel speedup, parallel efficiency, and parallelizable fraction are given in Tables 5.1 and 5.2 for different numbers of processors in MCNP5 and TITAN, respectively. Note that the MCNP5 parallel algorithm designates a master processor and then distributes the number of histories to be simulated over the remaining processors. The MCNP5 parallelizable fraction estimated is very high ($\sim 98\%$), as expected for a Monte Carlo code. TITAN was found to have a parallelizable fraction greater than 90% and, as expected, parallel efficiency decreased with increasing number of processors due to the increased communication time.

Table 5.1: MCNP5 parallel computation time analysis for 1 billion particle histories

Number of processors	Wall Clock Time (min)	Parallel Speedup	Parallel Efficiency	Parallelizable Fraction
1	1132.9	-	-	-
4	380.3	2.98	0.74	0.89
8	170.8	6.63	0.83	0.97
12	111.6	10.15	0.85	0.98
16	87.3	12.98	0.81	0.98

Table 5.2: TITAN parallel computation time analysis for 1 projection angle

Number of processors	Wall Clock Time (min)	Parallel Speedup	Parallel Efficiency	Parallelizable Fraction
1	3.33	-	-	-
4	0.94	3.53	0.88	0.96
8	0.63	5.29	0.66	0.93
12	0.51	6.49	0.54	0.92
16	0.48	6.89	0.43	0.91

The parallel speedup seen for increasing number of processors is plotted in Fig. 5.1 for MCNP5 and TITAN. The speedup for TITAN quickly levels off as the number of processors increases; however, the MCNP5 data still shows roughly linear behavior. This result is expected since the MCNP5 code does not need as much communication between processors as the deterministic TITAN code. Monte Carlo codes use indepen-

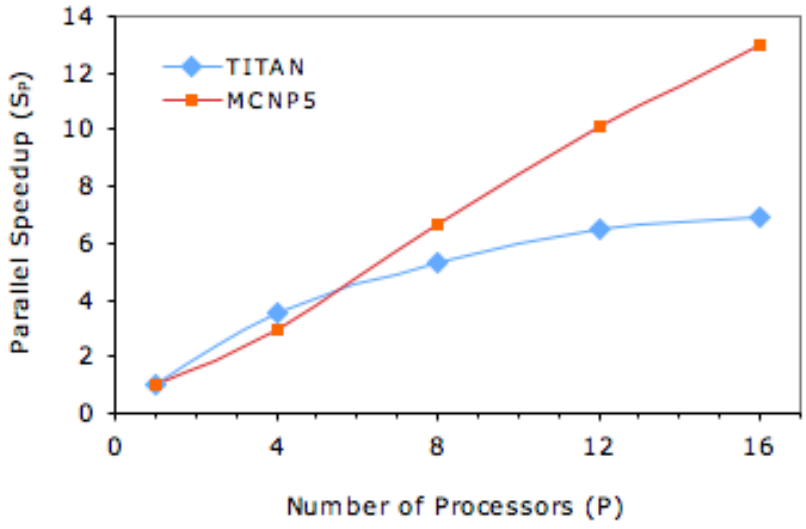

Figure 5.1: Parallel speedup for TITAN and MCNP5 as a function of number of processors

dent particle histories so if the number of histories is given the processors do not need to communicate until the end of the simulation. The parallel TITAN code uses angular decomposition, which requires the processors to communicate after each iteration to recalculate the scattering source. For S_6 quadrature, there are 48 ordinates or directions that TITAN can divide among processors.

5.1.3 Parallelized SPECT Projection Algorithm

When computing different projection angles in a SPECT simulation, TITAN's methodology has an advantage over other codes. Once the S_N method solves for the flux distribution within the phantom, any number of projection angles can be computed without needing to recalculate the phantom flux. The flux distribution is also independent of the collimator size so small acceptance angles do not take longer to solve for, as they would in a Monte Carlo code. Originally, the TITAN code ran in parallel up until the calculation of projection images, which was done in serial. This did not impact the computation time significantly for small numbers of projection images, but when enough projections are obtained for image reconstruction the time to compute projections dominated.

To make the TITAN SPECT simulation fully parallel, the calculation of projection angles was divided over the number of processor cores[62]. The total computation time was examined with the previous serial projection calculation and the new parallel projection calculation for varying numbers of projection images and processors, as shown in Table 5.3. In Table 5.3, the significant increase in computation time with increasing pro-

jection angles is evident when the projection calculation is in serial. For 180 projection images on 16 processors the total computation time is reduced by 85.5% if the projection image calculation is parallelized.

Table 5.3: TITAN computation time comparison for serial and parallel projection image computation

Number of processors	Number of projection images	Time with serial projection (sec)	Time with parallel projection (sec)
1	1	201	200
2	1	104	104
2	4	109	106
2	90	259	182
2	180	419	261
4	1	57	57
4	4	62	57
4	90	211	95
4	180	368	134
8	1	38	38
8	4	43	38
8	90	192	58
8	180	349	78
16	1	28	29
16	4	34	28
16	90	183	38
16	180	341	49

The time in TITAN to complete only the projection image calculation is given in Table 5.4 for different numbers of projection images and processors. This projection image computation time is the total computation time minus the time to calculate the flux distribution in the phantom region using the discrete ordinates method. Comparing

the serial and parallel projection calculations, as expected, the times scale very closely with the number of processors for the 2- and 4-processor cases. However, as was seen in Table 5.3, there is some loss of speedup due to increased communication in the cases with 8 and 16 processors.

Table 5.4: TITAN projection image computation time comparison for serial and parallel calculations

Number of processors	Number of projection images	Serial projection image calculation time (sec)	Parallel projection image calculation time (sec)
1	1	2.2	2.3
2	1	2.2	2.3
2	4	7.5	4.1
2	90	156.6	80.1
2	180	316.8	158.4
4	1	2.2	2.3
4	4	7.4	2.4
4	90	156.9	41.1
4	180	314.0	79.9
8	1	2.3	2.5
8	4	7.5	2.5
8	90	156.9	22.4
8	180	313.6	42.4
16	1	2.3	2.4
16	4	7.5	2.5
16	90	156.5	11.7
16	180	315.8	22.7

5.2 Weighted Circular Ordinate Splitting

As discussed in Section 4.2, the accuracy of the TITAN code's COS technique for simulating the collimator with different acceptance angles[62] has been examined. The work found the TITAN methodology to be accurate for small acceptance angles, but with decreasing accuracy apparent for larger angles. While much larger acceptance angles may not be practical for SPECT collimators, it is desired that the TITAN methodology be applicable to a wide range of geometries and, therefore, applications. For example, modeling streaming through ducts[66] in a nuclear reactor to estimate dose to workers. In addition, it would be desirable to further improve the accuracy for small acceptance angles and make the collimator representation more physical.

A new methodology based on the COS technique for collimator representation has been developed and implemented in the TITAN code: weighted circular ordinate splitting[67, 68] (WCOS). The original COS technique used a simple average of the angular flux of all split directions and allowed the user to specify a single value for the number of directions per concentric circle, referred to as the splitting order. The WCOS technique makes use of Riauka and Gortel's (1994) collimator representation, which is part of their analytical method to simulate SPECT[34]. In the new technique, the split directions specified within a collimator acceptance angle are used to calculate a geometry-based weighted average as shown in Figure 5.2. The weighting is determined by the overlap of the detector surface area projection along the direction to the front of collimator. The split

directions originate at the center of the back of each collimator hole, so this weighting approximates the effect of different positions within the collimator.

The new technique also allows different numbers of split directions per concentric circle, which the TITAN code did not previously permit. The user must specify the number of directions on the innermost circle and the number of directions for each remaining circle is scaled according to the circle area. An example is given in Fig. 5.3 for two concentric circles and a splitting order of 6. This representation of the collimator is expected to improve the accuracy of the TITAN code's SPECT simulation by sampling the collimator acceptance angle more uniformly.

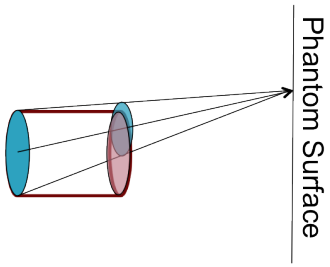

Figure 5.2: Projection of detector surface area to front of collimator along a split direction; flux is weighted by the overlapping area

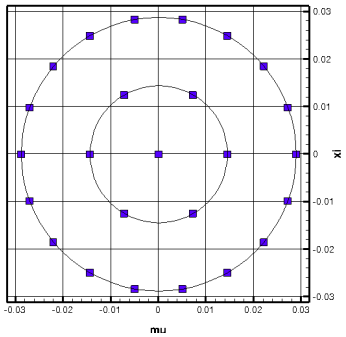

Figure 5.3: Example of splitting directions for two circles and a splitting order of 6

To test the WCOS technique, results were compared with MCNP5 projection images for a simple cube water phantom with a cube of Tc-99m located at its center, as shown in Fig. 5.4. The phantom edge is 10 cm and the model is symmetric so a single row of collimators is simulated. One-group cross sections (126.5-154.6 keV) were generated

using the CEPXS code. MCNP5 is run with the multigroup option and uses the same cross sections to minimize differences with TITAN.

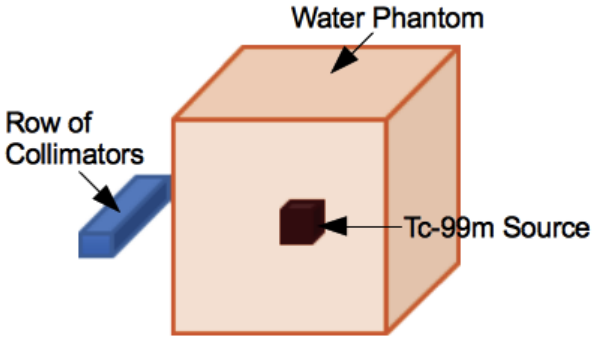

Figure 5.4: Phantom geometry for WCOS testing

Two collimator sizes are tested and the parameters are given in Table 5.5. These collimator parameters were chosen based on commercial collimators. The $1.65°$ collimator has parameters typical of a low energy, general purpose (LEGP) SPECT collimator. The $4.29°$ collimator is representative of a low energy, high sensitivity (LEHS) SPECT collimator and is expected to benefit the most from the WCOS technique. Meshing and quadrature studies determined that a mesh size of 0.156 cm is appropriate for the LEGP collimator and 0.3125 cm for the LEHS collimator, with S_{20} used for both collimators.

Table 5.5: Collimator parameters

Collimator	Acceptance Angle	Detector Pixel Size
LEGP	$1.65°$	0.21 cm
LEHS	$4.29°$	0.34 cm

Using the model geometry, the LEGP collimator acceptance angle will result in split directions spanning a diameter of 0.29 cm at the phantom surface. Given the mesh

size for this phantom, it is determined that 2 splitting circles are needed to ensure that enough voxels at the phantom surface are included to properly represent the collimator. The normalized flux distribution at the detector as calculated by the TITAN code is compared against MCNP5 results for the LEGP collimator in Fig. 5.5. MCNP5 1σ statistical uncertainties are $0.8 - 3.6\%$ for this data. For normalized fluxes greater than 0.1, the average difference between the TITAN and MCNP5 results is 2.3%. For this small collimator acceptance angle, no significant difference was observed between the original COS technique in TITAN and the new WCOS technique. As a further comparison, the full width at half maximum (FWHM) is compared between the codes. In MCNP5 the FWHM is 1.27 cm and in TITAN it is 1.25 cm, for a relative difference of -1.2%.

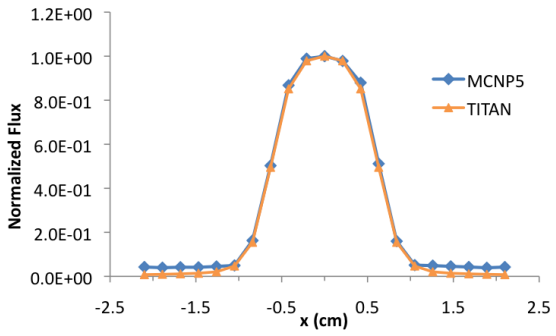

Figure 5.5: TITAN and MCNP5 (1σ $0.8 - 3.6\%$) flux distributions for LEGP collimator ($1.65°$)

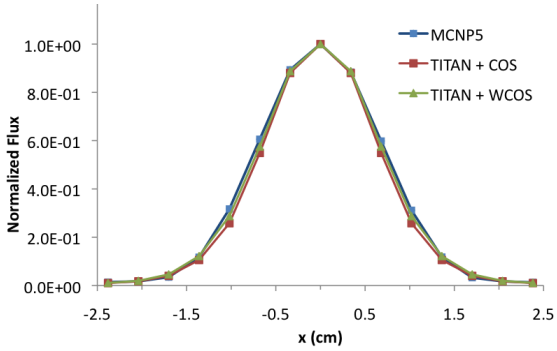

Figure 5.6: TITAN and MCNP5 (1σ $0.4 - 4.4\%$) flux distributions for LEHS collimator ($4.29°$)

Considering the LEHS collimator, projecting the collimator acceptance angle to the phantom surface, split directions will span 0.75 cm. Considering the phantom mesh size, it is determined that 2 splitting circles should be used for the LEHS case to include enough voxels at the phantom surface. The normalized flux distributions with the LEHS

Table 5.6: Comparison of MCNP5 and TITAN flux distributions for LEHS collimator

Code	FWHM (Relative Difference)	Average Relative Difference
MCNP5	1.60 cm	-
TITAN + COS	1.47 cm (-7.9%)	8.5%
TITAN + WCOS	1.54 cm (-4.0%)	3.8%

collimator are given in Fig. 5.6 as calculated by MCNP5, TITAN with the original COS technique, and TITAN with the new WCOS technique. The MCNP5 data 1σ statistical uncertainties are $0.4 - 4.4\%$. A difference in the slope on the sides of the peak can be seen between the different methods, in Fig. 5.6. The TITAN code with the WCOS technique improves the match with the MCNP5 results. Table 5.6 gives a quantitative comparison between the TITAN solutions and MCNP5 by comparing the FWHM and the average relative difference in detector pixels greater than 0.1. The WCOS technique is clearly improving the TITAN code's simulation of the SPECT data.

The performance of COS and WCOS for different numbers of splitting directions was also studied for 2.1° and 7.7° collimator acceptance angles[67] for the same phantom. Results for the 2.1° collimator with COS and WCOS matched the reference MCNP5 solution well and increasing the number of splitting circles and/or directions did not noticeably alter the results. For the 7.7° collimator, the WCOS technique showed improved accuracy over the original COS technique and consistent behavior with varying parameters.

Additional work has used the COS and WCOS techniques to simulate particle streaming in a nuclear power plant duct[66]. The duct acts as a collimator with an accep-

tance angle of 3.0°. Compared with an MCNP5 reference solution, TITAN with COS and TITAN with WCOS gave similar results, but the WCOS technique behaved more consistently with increasing number of split directions.

Chapter 6

Implementation of the Novel Image Reconstruction Methodology

In this chapter, a novel image reconstruction methodology that utilizes a deterministic transport code is developed. Next, a framework for implementing the methodology with any deterministic transport code is given in the form of a script. Finally, the methodology is applied to a 2-dimensional reconstruction as a feasibility study.

6.1 DRS Methodology

When seeking to model particle transport in SPECT reconstruction, Monte Carlo methods are the standard. Monte Carlo methods have the advantages of modeling exact geometry and continuous energy, but tend to require long computation times to achieve acceptable statistical uncertainties and provide limited information. In contrast, deterministic

methods solve the linear Boltzmann equation numerically. They generally have shorter computation times and provide large amounts of information, but the phase space is discretized and they can be memory intensive for achieving accurate results. With modern computers, this memory requirement is less of a difficulty, and so deterministic methods have the potential to provide an alternative to Monte Carlo methods.

This new deterministic reconstruction methodology for SPECT (DRS) was developed to take advantage of the TITAN deterministic transport code's fast algorithm for simulating SPECT projection images, but it could easily be used with other deterministic codes. As discussed previously, the ML-EM reconstruction algorithm is the most common for SPECT and will be used for this work; however, other iterative reconstruction algorithms should be possible to apply. Recall that the ML-EM algorithm[23] can be represented by

$$\hat{\lambda}_b^{(i+1)} = \hat{\lambda}_b^{(i)} \sum_{d=1}^{D} \frac{n_d^*}{n_d^{(i)}} p_{b,d}, \quad b = 1, \ldots, B, \tag{6.1}$$

where $\hat{\lambda}_b^{(i)}$ is the i^{th} estimate of the unknown source density in voxel b, n_d^* is the measured data in detector pixel d, $n_d^{(i)}$ is the projection data using the last source estimate, and $p_{b,d}$ (the system matrix) is the probability that a source particle emitted in voxel b is detected in detector pixel d. The denominator in Eq. 6.1 is the "forward" projection that is completed by a deterministic transport code and the summation is the backprojection.

The steps for the DRS methodology are outlined in a flowchart given in Fig. 6.1. In addition to the initial guess of the source distribution, the reference measured projection data and system matrix must be provided. Particle transport is then completed in the

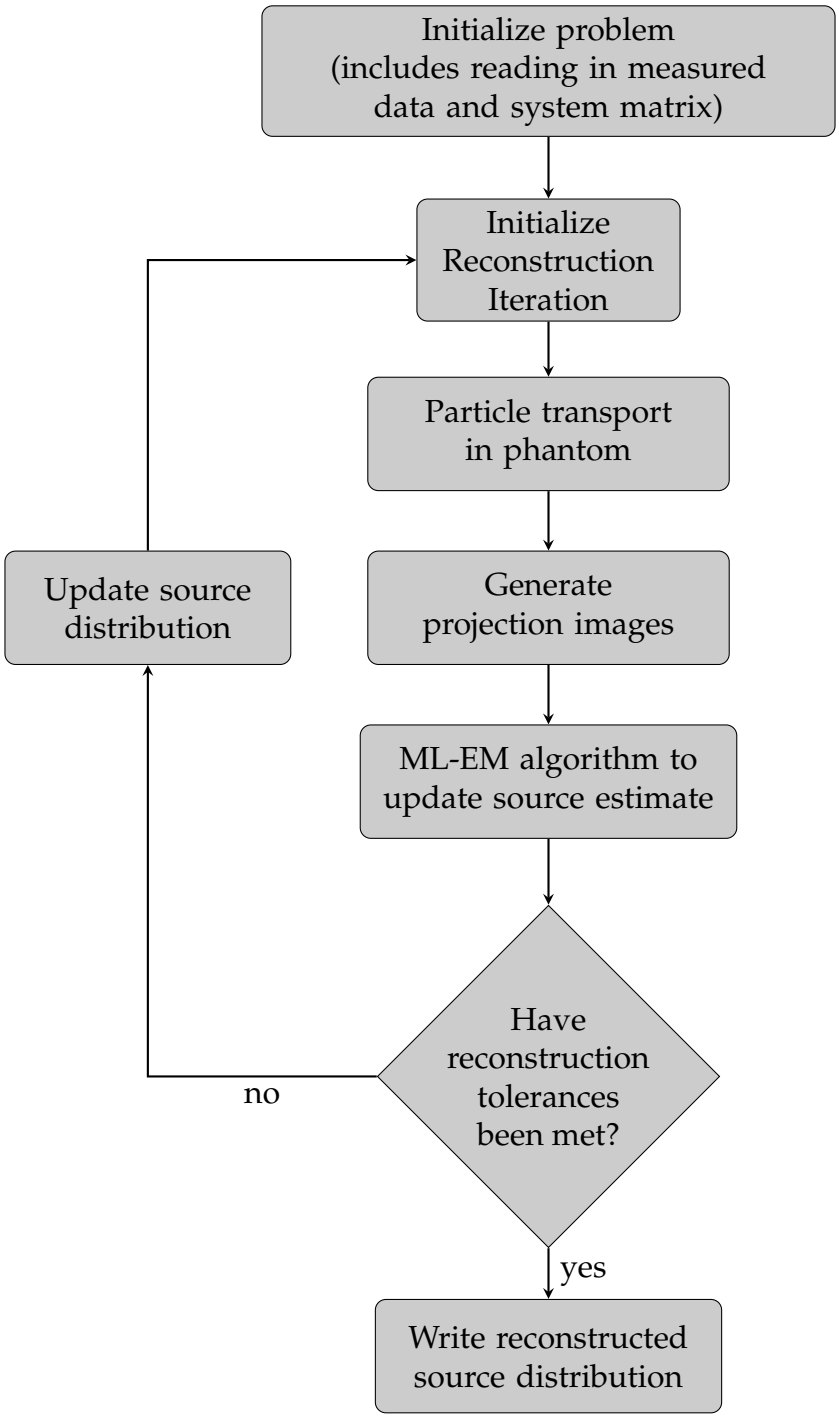

Figure 6.1: DRS methodology workflow

phantom and the projection images based on the current estimate of the source distribution are created. These projections are passed to the ML-EM algorithm, which compares them with the measured data and backprojects to update the source estimate. If tolerances have not been met, the processes is restarted with the updated source distribution.

6.2 Analysis of DRS methodology

6.2.1 Framework Implementation

A framework was created based on the DRS methodology in the form of an image reconstruction script. The script iteratively calls the TITAN code and feeds the output into an ML-EM algorithm. The script could be used to call any particle transport code that generates projections at a detector for a given source distribution. With this implementation, the TITAN transport calculation can be run in parallel, but all other calculations are in serial, including the ML-EM algorithm. Additional read/write times are associated with having an external script call TITAN iteratively; however, this script allows for preliminary testing and troubleshooting of issues that appear before implementing the reconstruction algorithm into the TITAN source code. This framework can be used to demonstrate reasonable reconstruction computation times while allowing the performance of a deterministic transport code as a forward projector to be analyzed.

Iterative reconstruction is implemented using a script with the following steps:

i. Initialize TITAN input file with a guess of the source distribution $\hat{\lambda}^{(0)}$

ii. Call the TITAN SPECT simulation to obtain projection data $n^{(i)}$

iii. Call the ML-EM algorithm to compare the generated projection data $n^{(i)}$ with the measured data n^* and generate the new updated source distribution $\hat{\lambda}^{(i+1)}$

iv. Update the estimated source distribution $\hat{\lambda}^{(i+1)}$ in the TITAN input file.

Steps ii-iv are repeated until the maximum number of iterations has been completed or some tolerance has been met. This procedure allows all interactions in the phantom to be simulated in the forward projection step by TITAN. The ML-EM algorithm called in *Step iii* is written in Fortran 95 and calculates the new source estimate using Eq. 6.1. The script and the ML-EM code that it calls are given in Appendix A.

6.2.2 Phantom Studies

A simple 2-dimensional elliptical water phantom is reconstructed with the DRS script as a feasibility study of the methodology. The water phantom has a background relative source strength of 1 and two circles with source strengths of 2 to represent lesions, as depicted in Fig. 6.2. The voxelized model has 64 by 64 voxels and is 22.4 cm by 22.4 cm. It is important to note that the TITAN code is a 3-dimensional code that is being used to complete a 2-dimensional reconstruction. This leads to some inefficiencies; in particular, a 3-dimensional cylinder with no variation along z is modeled in TITAN to simulate this 2-dimensional phantom, as shown in Fig. 6.3.

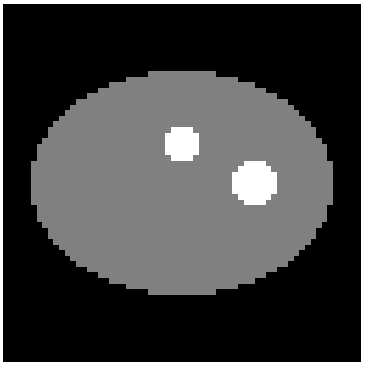

Figure 6.2: Reference source distribution with source strengths of 2 in white and 1 in gray

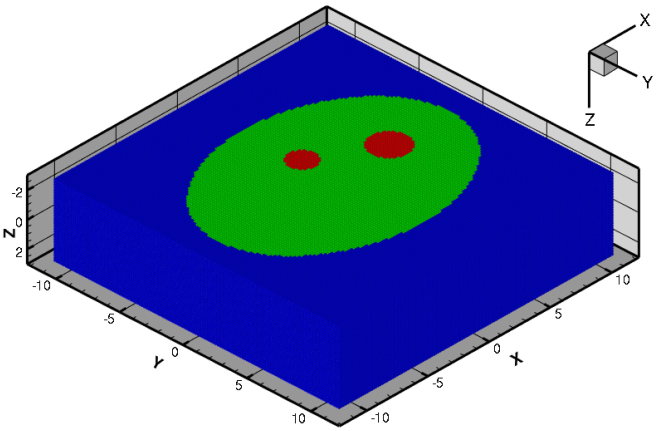

Figure 6.3: TITAN 3-dimensional model

A flat source distribution of one is used for the initial guess $\hat{\lambda}^{(0)}$. The system matrix, $p_{b,d}$, is obtained using Professor Jeff Fessler's Image Reconstruction Toolbox[36] for MATLAB and models attenuation only, i.e., not scatter. The SIMIND Monte Carlo code[31] is used to generate the measured projection data, which is displayed as a sinogram in Fig. 6.4. Recall from Section 2.2 that in a sinogram the detector elements are displayed along the horizontal axis and the projection angles are given along the vertical axis. In Fig. 6.4, 120 projection images are obtained over $360°$ counter-clockwise around the phantom with the initial angle located directly above the phantom in Fig. 6.2. Reconstructions with 60 projection images obtained over $180°$ counter-clockwise around the left-hand side of the phantom are also considered. The 60 projection reconstructions use the top half of Fig. 6.4 as the measured projection data. The SIMIND data is for a long simulation, such that the statistical uncertainty can be approximated as zero, and a perfect collimator, i.e., extremely narrow and no septal penetration, is simulated at this time.

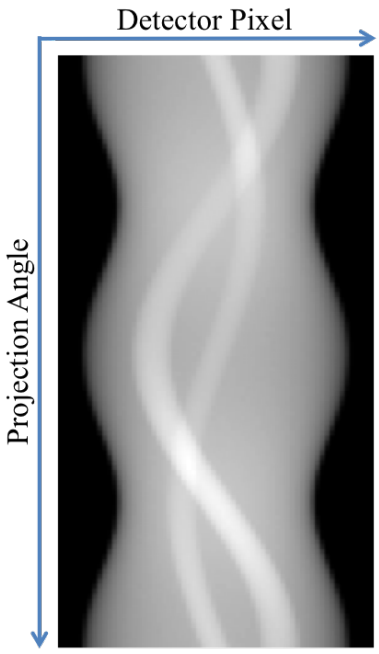

Figure 6.4: Reference sinogram for 120 projection angles produced by SIMIND

Parameter Selection

Deterministic discrete ordinates codes, e.g., TITAN, use discretization of space, energy, and angle to numerically solve the LBE and as a result are subject to discretization errors. To establish the appropriate deterministic parameters, initial studies are done using the solution as the source distribution in the TITAN model. One-hundred and twenty projection images are simulated over 360° around the phantom. The resulting sinograms are then compared for different parameter choices, including mesh size, quadrature order, and anisotropic scattering order. For comparison, the mean square error (MSE) is defined as

$$MSE = \frac{1}{N_v} \sum_{i}^{N_v} (I_i - R_i)^2 \,, \tag{6.2}$$

where I is the simulation result for a particular set parameters, R is the reference solution, and N_v is the number of detector pixels. The maximum relative difference is defined as

$$\text{Max. rel. diff.} = max\left(\frac{I_i - R_i}{R_i}\right) \quad \text{for } i = 1 \ldots N_v. \tag{6.3}$$

To examine the sensitivity of results to mesh size, the number of meshes is doubled in each dimension from each case number to the next, as shown in Table 6.1. The mesh parameter h is defined as the mesh size relative to Case 3 (the finest mesh size).

Table 6.1: Meshing parameters

Case	h	Mesh size	Number of meshes
1	4	3.50 mm	64 x 64
2	2	1.75 mm	128 x 128
3	1	0.875 mm	256 x 256

The detector flux at different projection angles was plotted to ensure that the mesh refinement was adequate. Selected plots are given in Fig. 6.5 for projection images at 21° and 141°. The match with the reference SIMIND solution is seen to improve as h decreases, i.e., decreasing mesh size, in the TITAN simulation. The $h = 4$ mesh shows a few unphysical oscillations; however, the improvement from $h = 2$ to $h = 1$ is minimal.

The quadrature order was also examined from S_{12} to S_{40}. The maximum relative difference and MSE of the TITAN sinogram relative to the S_{40} solution for different quadrature orders is given in Table 6.2. A large reduction in differences is seen when the quadrature is increased from S_{16} to S_{20}.

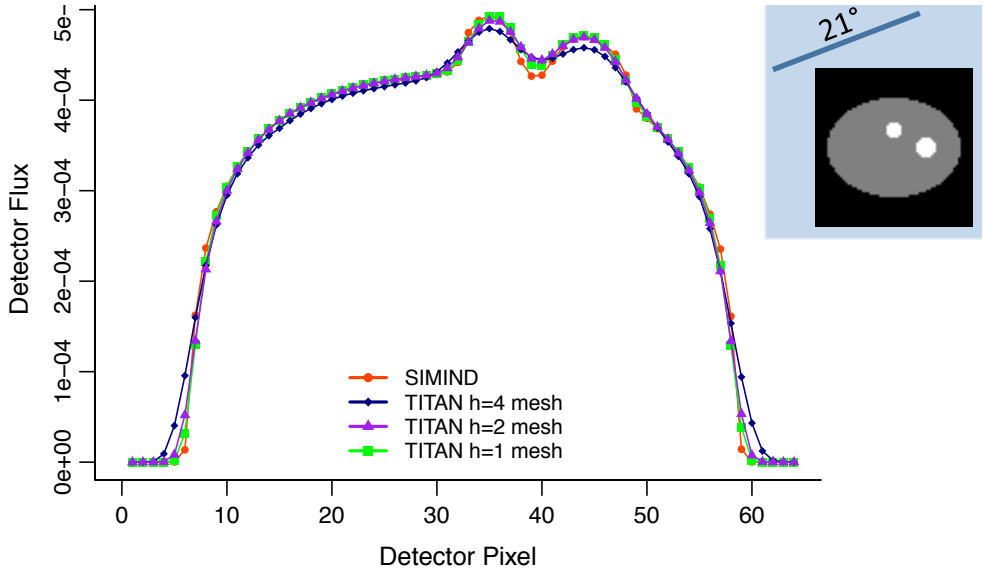

(a) 21°

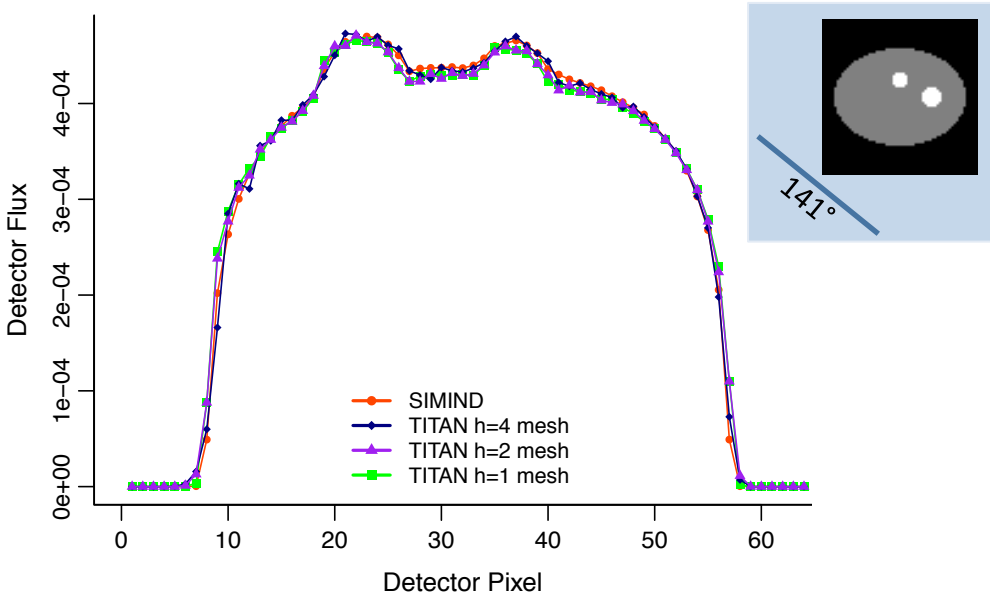

(b) 141°

Figure 6.5: Projection image comparison with SIMIND for different TITAN meshings

Table 6.2: TITAN sinogram maximum relative difference and MSE relative to S_{40}

S_N	Number of Directions	Max. Rel. Difference	MSE
12	168	-14.72%	1.09E-03
16	288	-7.40%	3.34E-04
20	440	-0.05%	9.94E-08
30	960	0.02%	1.91E-08

The dependency on anisotropic scattering order, L in P_L, was examined by comparing P_1 and P_3 sinograms with reference P_5 solutions. The maximum relative difference and MSE are given in Table 6.3. The P_1 sinogram has small differences from the reference solution and the P_3 sinogram matches the reference solution very closely.

Table 6.3: TITAN sinogram maximum relative difference and MSE relative to P_5 for different scattering orders

P_N	Max. Rel. Difference	MSE
1	3.3%	2.98E-04
3	0.3%	2.72E-06

Based on the sensitivity analysis conducted, the $h = 2$ meshing, S_{20} quadrature set, and P_1 scattering order are determined to be an appropriate set of parameters for the following iterative reconstruction studies. The impact of deterministic parameter selection on reconstruction will be examined in Chapter 8.

Reconstruction Results

Using the described script, the source distribution was reconstructed with a flat distribution of one as the initial source estimate. The following results examine the generated

sinograms and source distributions for measured data over 180° and 360°, as well as the convergence of the reconstruction.

Using measured projections over 180°, the sinograms generated by TITAN and the reconstructed source distributions after 5, 10, 20, and 40 iterations are given in Figs. 6.6 and 6.7, respectively. The TITAN forward projection uses the S_{20} quadrature set and the DDZ (diamond differencing with zero fix-up) differencing scheme, as discussed in Section 3.1. In Figs. 6.6a and 6.7a, the source distribution is already taking shape after 5 iterations; however, with additional iterations an artifact in the form of ripples near the right edge of the phantom is present. This artifact grows with increasing numbers of iterations and is attributed to the measured sinogram data being limited to the left-hand side of the phantom. The DTW (directional theta weighted) differencing scheme[56] should be less susceptible to unphysical oscillations than the DDZ differencing scheme for the same discretization. The sinograms generated by TITAN and the reconstructed source distributions after 5, 10, 20, and 40 iterations are given in Figs. 6.8 and 6.9, respectively, for S_{20} and the DTW differencing scheme. The ripple artifact is significantly reduced, compared to the DDZ result, but some oscillations are still present on the right-hand side of the reconstruction. A bright ring of source is also appearing around the phantom edge with increasing iterations.

Reconstruction is now done using 120 projection angles over 360° around the phantom to determine if the artifacts seen in Figs. 6.7 and 6.9 are due to a lack of information about the right-hand side of the phantom. The reconstructed source distributions

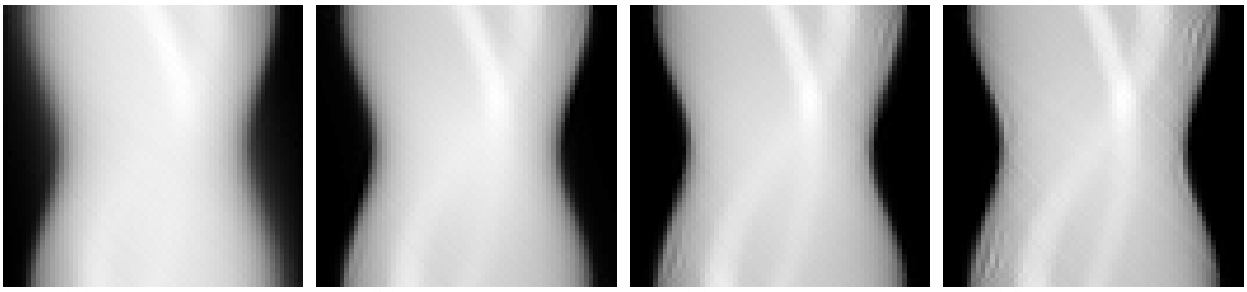

(a) 5 iterations (b) 10 iterations (c) 20 iterations (d) 40 iterations

Figure 6.6: Sinograms generated by TITAN (S_{20} DDZ) over $180°$

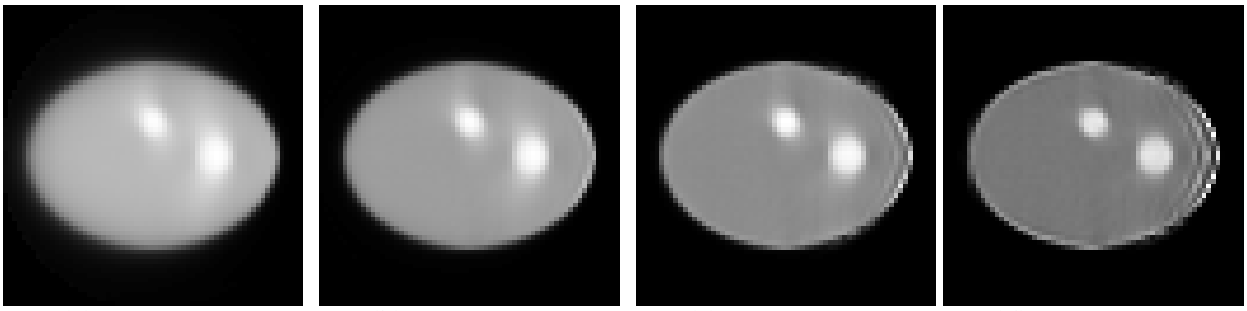

(a) 5 iterations (b) 10 iterations (c) 20 iterations (d) 40 iterations

Figure 6.7: Reconstructed source distributions from TITAN $180°$ sinograms (S_{20} DDZ)

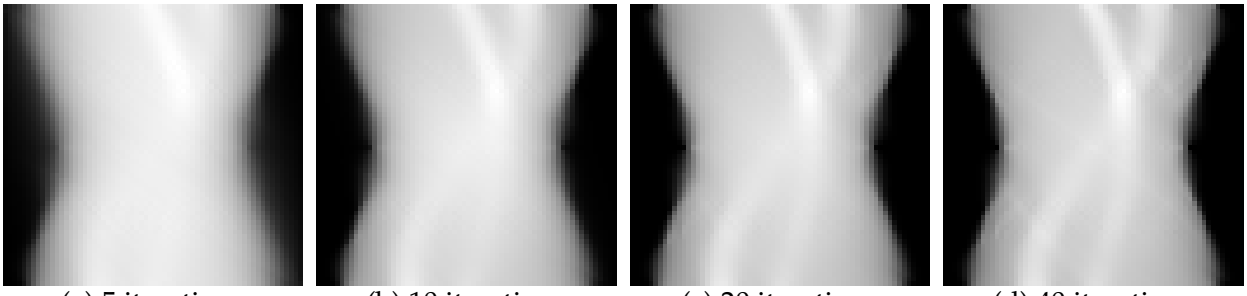

(a) 5 iterations (b) 10 iterations (c) 20 iterations (d) 40 iterations

Figure 6.8: Sinograms generated by TITAN (S_{20} DTW) over $180°$

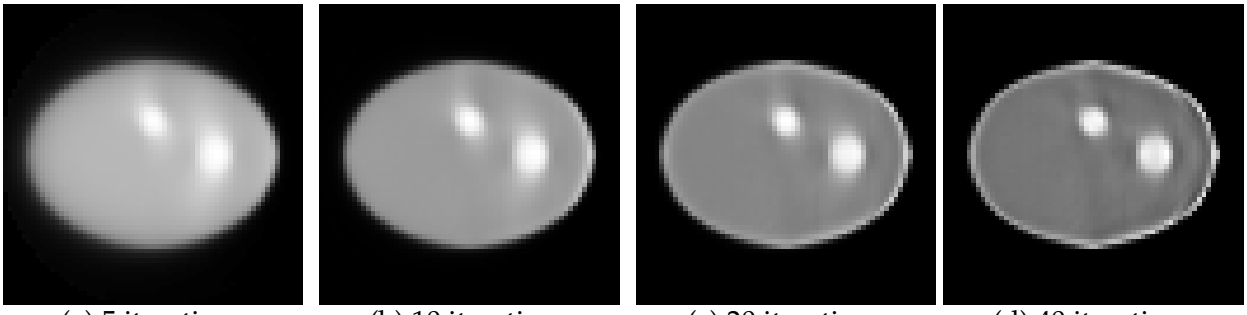

(a) 5 iterations (b) 10 iterations (c) 20 iterations (d) 40 iterations

Figure 6.9: Reconstructed source distributions from TITAN $180°$ sinograms (S_{20} DTW)

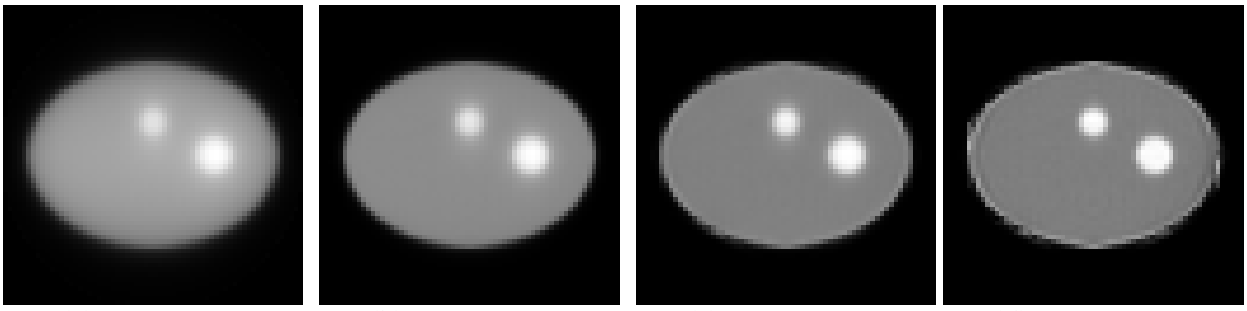

(a) 5 iterations (b) 10 iterations (c) 20 iterations (d) 40 iterations

Figure 6.10: Reconstructed source distributions from TITAN 360° sinograms (S_{20} DDZ)

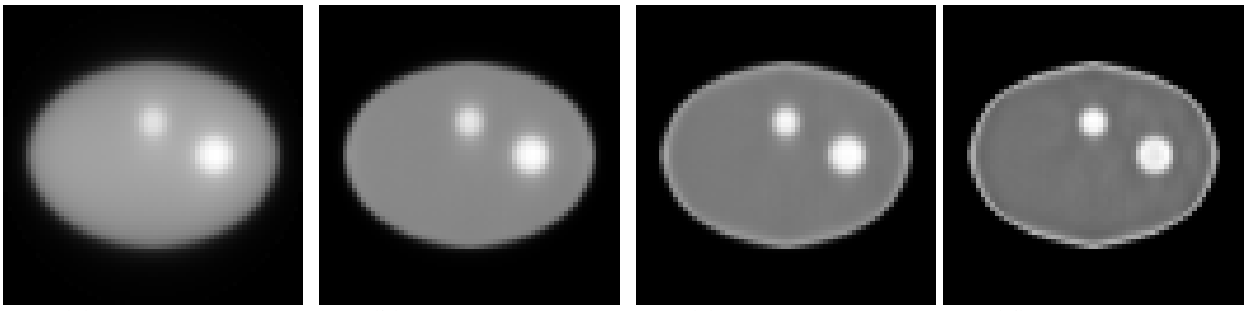

(a) 5 iterations (b) 10 iterations (c) 20 iterations (d) 40 iterations

Figure 6.11: Reconstructed source distributions from TITAN 360° sinograms (S_{20} DTW)

for 5, 10, 20, and 40 iterations are given in Figs. 6.10 and 6.11 for DDZ and DTW, respectively. Using measured projection data over 360° has removed the ripple artifact from the reconstructed source and generally improved the reconstruction visually, but the bright ring of source around the phantom edge persists above 20 iterations.

The edge, or ring, artifact was initially thought to be caused by the differencing scheme used by TITAN being inadequate at source discontinuities. Petrovic and Haghighat[53] showed that unphysical oscillations, that are not ray effects, can occur at discontinuities due to the inconsistency between particle direction and the spatial differencing axis. These oscillations can not be removed by mesh refinement. The DTW differencing scheme[69] was developed to minimize oscillations by incorporating particle

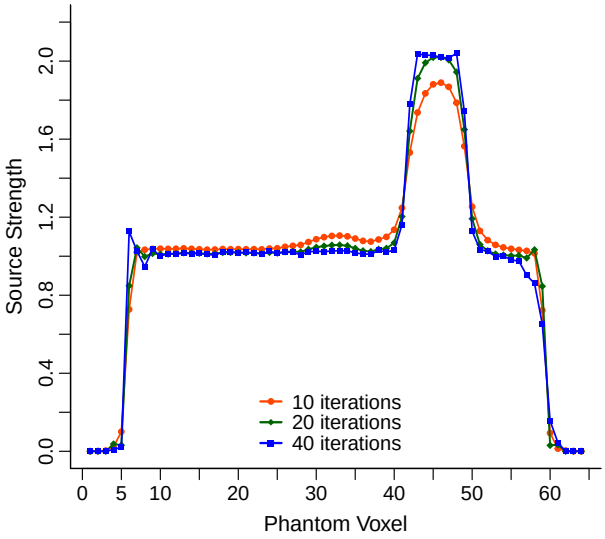

Figure 6.12: Horizontal profile through reconstructed source distribution with DDZ scheme

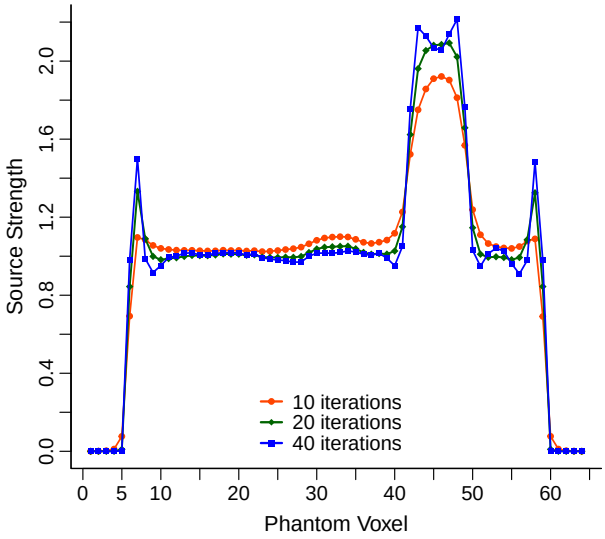

Figure 6.13: Horizontal profile through reconstructed source distribution with DTW scheme

direction into the differencing scheme. It may be that the oscillations at the edge of the phantom are magnified over the iterations to create the ring artifact.

To further examine these results, horizontal profiles through the center of the reconstructed source distributions are given in Figs. 6.12 and 6.13 for DDZ and DTW, respectively, at 10, 20, and 40 iterations. Fig. 6.12 shows some oscillation at the phantom edge and an excellent representation of the source distribution within the phantom, as the number of iterations reaches 40 using DDZ. The reconstruction with DTW, Fig. 6.13, overshoots the source at the edge of both the phantom and the circle of increased source strength. This issue begins to appear for as few as 10 iterations and becomes larger with additional iterations. The DDZ solution appears to be adequate for this model and will be used in the following analysis, but in Section 8.1 the limitations of DDZ will be encountered and DTW will be used.

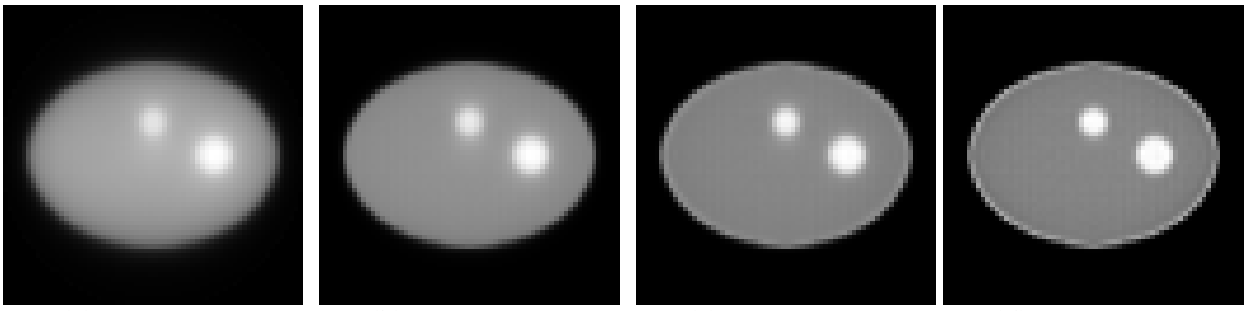

(a) 5 iterations (b) 10 iterations (c) 20 iterations (d) 40 iterations

Figure 6.14: Reconstructed source distributions using the system matrix only

A literature search revealed that edge artifacts that resemble the Gibb's phenomenon are inherent to the ML-EM algorithm where source discontinuities occur[70]. Snyder et al. concluded that these artifacts can be caused by the numerical precision of the computer, small mismatches between model and simulation, and other effects. To test this possible origin of the ring artifact, an ML-EM reconstruction was done using the system matrix only, i.e., without TITAN. The reconstructed source distributions for 5, 10, 20, and 40 iterations are given in Fig. 6.14 and closely resemble those produced using TITAN. The ring artifact begins to appear in iteration 20 and becomes brighter by 40 iterations.

Horizontal and vertical profiles through the center of the reconstruction after 40 iterations are shown in Figs. 6.15 and 6.16, respectively, for reconstruction with TITAN and with the system matrix (SM) only. In the phantom interior, the TITAN reconstruction better represents the true source distribution. At the edge of the phantom, while both reconstructions show oscillations, the oscillations do appear to be larger in these particular profiles for the reconstruction with TITAN. This leads to the conclusion that the edge artifact may be contributed to by both the differencing scheme and the oscillations inherent to ML-EM.

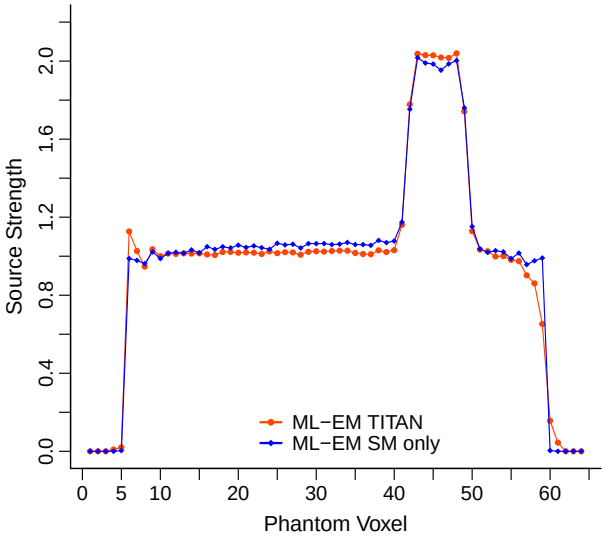

Figure 6.15: Horizontal profile through reconstructed source distribution using TITAN and using the system matrix only

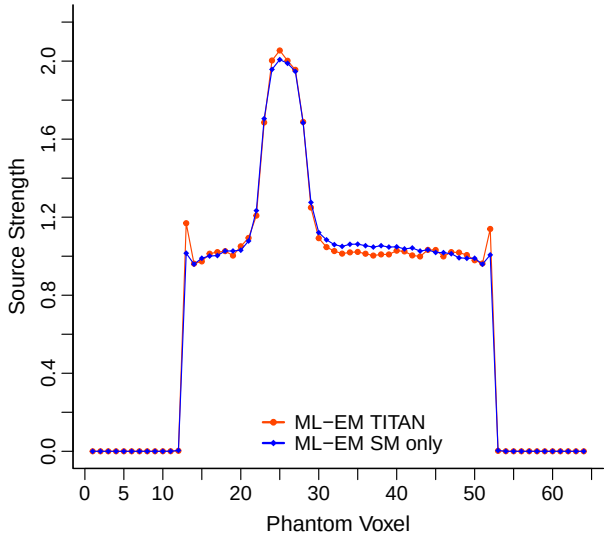

Figure 6.16: Vertical profile through reconstructed source distribution using TITAN and using the system matrix only

As a quantitative measure of reconstruction quality, the contrast can be calculated. The contrast in a region l is defined as

$$C_l = \frac{\bar{I}_l - \bar{I}_0}{\bar{I}_0}, \tag{6.4}$$

where $\bar{I}_l$ is the average source intensity in a region of interest and $\bar{I}_0$ is the average reference background intensity in a region of the same size. The contrast in the larger circle of source (right-most circle) is given as a function of iteration number in Fig. 6.17 for reconstruction with TITAN and with the system matrix only. Note that the contrast for the reference solution is 1.0. In Fig. 6.17, the contrast increases at a faster rate and to a higher value when TITAN is used in the reconstruction. Recall that the system matrix does not fully model particle transport in the phantom, i.e., does not include scatter, while TITAN does. The advantage of fully modeling the physics in the phantom is clear in the contrast

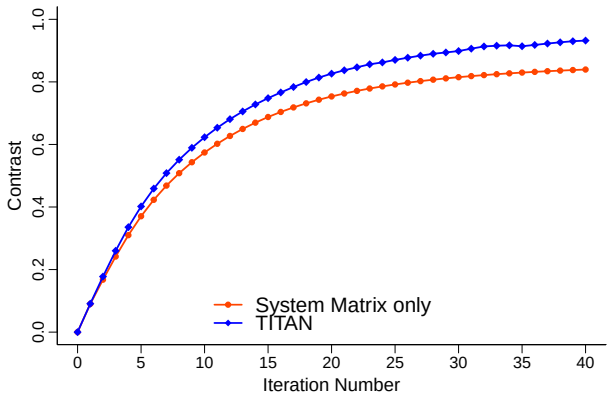

Figure 6.17: Contrast of large circle in reconstructed source distribution using TITAN and using the system matrix only

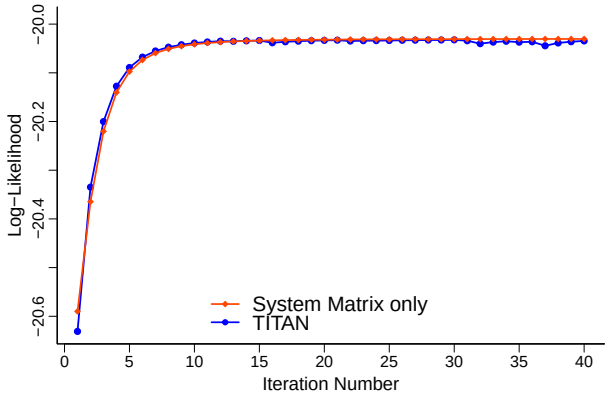

Figure 6.18: Log-likelihood of reconstructed source distribution using TITAN and using the system matrix only

recovered in Fig. 6.17. After 40 iterations, the contrast is 0.84 using the system matrix only and 0.94 using TITAN.

Since the ML-EM algorithm seeks to maximize the likelihood of observing the measured data, the likelihood function is a natural choice to examine reconstruction convergence. The log-likelihood, excluding terms that are independent of iteration number, is given by

$$l(\hat{\lambda}) = \sum_{d=1}^{D} n_d^* log(\hat{n}_d) - \sum_{d=1}^{D} \hat{n}_d, \tag{6.5}$$

where n^* is the measured projection data, $\hat{n}$ is the projection data from the source estimate $\hat{\lambda}$, and there are D total detector elements. The log-likelihood as a function of iteration number is given in Fig. 6.18 for reconstruction with TITAN and with the system matrix only. The log-likelihood is very similar between the two reconstructions and levels off quickly, which unfortunately makes it an ineffective indicator of convergence.

Computation Time

All calculations in this chapter were completed on a dedicated computer cluster with Intel Xeon E5 2.6 GHz processors and 16 GB of memory per processor core. The reconstruction script calls TITAN in parallel on 16 cores and the rest of the ML-EM reconstruction is done in serial. Each forward projection of 120 projection images in TITAN took approximately 15 seconds. The computation time for reconstruction with 120 projection angles at different numbers of iterations is given in Table 6.4 along with the corresponding contrast in the large circle of source.

Table 6.4: Contrast and computation time of the reconstructed source distribution at different iterations

Iteration	Contrast	Computation Time
5	0.40	2.9 min
10	0.63	6.3 min
20	0.83	13.4 min
40	0.94	27.4 min

Most of the computation time in Table 6.4 is spent reading and writing files, because the script externally calls TITAN for each iteration with the updated source distribution. The computation time is expected to be significantly reduced by incorporating the ML-EM algorithm directly into the TITAN source code. In addition to removing the repeating reading and writing of files, this will also allow the ML-EM algorithm to be parallelized.

Chapter 7

Development of TITAN-IR Algorithm

In this chapter, the steps involved in implementing the DRS methodology into the TITAN source code are discussed, including the parallelization of the code. The modified version of TITAN is called TITAN-IR (TITAN with image reconstruction).

7.1 TITAN-IR Algorithm

The image reconstruction process implemented in TITAN-IR is outlined in Fig. 7.1. For the case of ML-EM reconstruction, there is one subset, i.e., $\mathrm{N}_{subsets} = 1$, which contains all projection angles. The initial source estimate $\hat{\lambda}^{(0)}$ is given in the input file and usually specified as a uniform source. The measured projection data and system matrix must be provided. A transport calculation is then completed based on the current source estimate to find the converged flux moments for the phantom. Next, as described in Section 3.2.3, the fictitious quadrature directions $(\mu^{(fix)}, \varphi^{(fic)})$ are generated for each projection angle

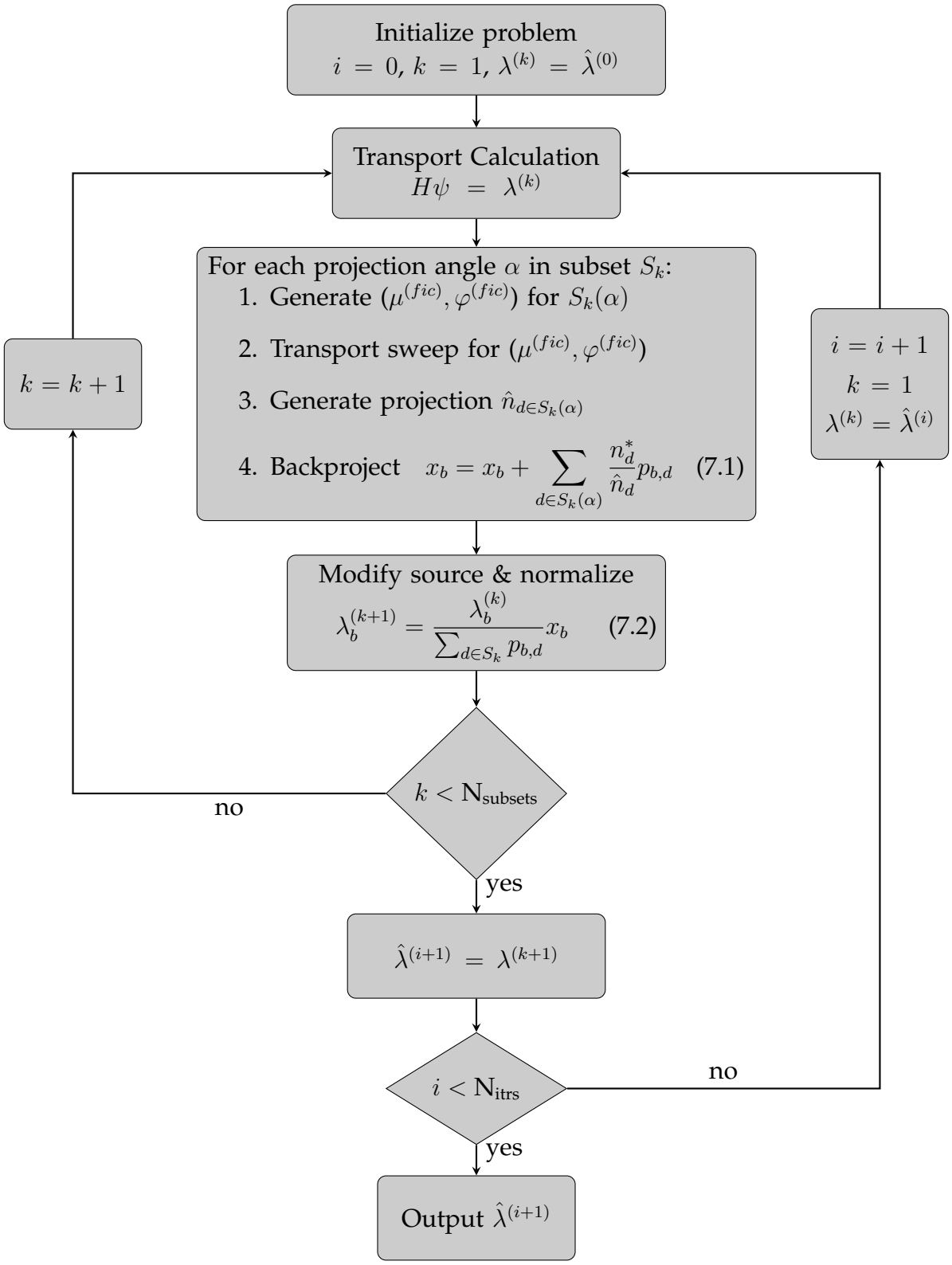

Figure 7.1: The TITAN-IR workflow

α, a transport sweep is completed for each fictitious direction, and ray-tracing is used to generate the projection images $\hat{n}$. For each angle, the projection $\hat{n}$ is normalized to the same total number of counts as the measured data. The resulting projection is then compared with the measured data n^* and backprojected using the system matrix p in Eq. 7.1. These backprojections x are summed over all projection angles. Once all angles have been iterated through, in Eq. 7.2 the backprojections are normalized and used to update the source estimate. Other tolerances could be used, but generally ML-EM reconstruction is terminated after a set number of iterations N_{itrs} have been completed.

7.2 TITAN-IR Implementation

Details on TITAN-IR input specifications are given in Appendix B. Deterministic codes already tend to require large amounts of memory so the additional memory required for the reconstruction should be considered. The primary additional memory requirement is the system matrix which has dimensions of the number of phantom voxels by the total number of detector elements over all projection angles. The code in Appendix B.3 converts a system matrix into the appropriate sparse matrix format, but for some 3-D simulations the system matrix size can still be on the order of gigabytes.

A low-pass filter has been implemented in the TITAN-IR algorithm to filter out the high-frequency noise common to ML-EM reconstructed images. The Butterworth filter was chosen because it is a popular filter for SPECT, but additional filter options could easily be added. The Butterworth filter is a low-pass filter, i.e., it does not alter low fre-

quencies and blocks high frequencies. The FFTW free-software library is used to compute the discrete Fourier transform[71] of the image. The Butterworth filter is given by

$$B(f) = \frac{1}{\sqrt{1 + \left(\frac{f}{f_c}\right)^{2n}}}, \tag{7.3}$$

where f is the frequency, n is the order, and f_c is the cutoff frequency. The cutoff frequency defines the frequency at which the filter amplitude begins to drop and the order changes the rate at which the filter amplitude goes to zero.

7.2.1 Parallel Implementation

In parallel transport calculations, the TITAN code divides the directions specified in the quadrature set over the available processor cores in what is referred to as *angular decomposition*. The parallel calculation is most efficient if the directions can be divided evenly over the available processors, but this is not a requirement. After determining the particle distribution in the phantom, each processor core calculates the projection images for its assigned angles in parallel. The processors then communicate to merge the projection images calculated on each processor into one complete sinogram, which is written to a file. Any time a parallel code must communicate amongst processors, the parallel efficiency is reduced.

To take advantage of the parallelization of the projection image calculation, the TITAN-IR backprojection step is also split across the processor cores and takes place after each projection image is calculated, but before the cores communicate. For each angle,

the projection image is backprojected to the source distribution contribution from that particular angle in Eq. 7.1 of Fig. 7.1. After all processor cores have completed their assigned angles, the contributions x are summed across the cores to update the final source distribution estimate.

7.2.2 OS-EM Implementation

Ordered-subsets expectation-maximization (OS-EM) is a common modification of the ML-EM algorithm where the projection angles are grouped into subsets. The standard ML-EM procedure to update the source estimate is followed for the first subset, i.e., using only the angles in the first subset. The new source estimate is then used as the initial source for ML-EM reconstruction using the angles in the second subset, and so on until all subsets have been passed through. At this point, all of the projection angles have been used once and the first iteration is done. Essentially, the advantage of OS-EM is updating the source at sub-iterations while moving through the projection angles instead of waiting until all angles have been considered to update the source. In matrix-based iterative reconstruction, this results in a computation time speedup nearly proportional to the number of subsets.

Unfortunately, one of the primary advantages of using the TITAN code for image reconstruction negates the gains from OS-EM. Recall that the TITAN algorithm for SPECT simulation first computes the particle distribution within the patient and then generates the projection images without having to redo this time-consuming first step for each an-

gle. This procedure allows TITAN to rapidly simulate a large number of projection angles, but means that breaking the angles into subsets saves only a small amount of computation time. OS-EM was still implemented in TITAN-IR because of its wide-spread use and because some modest reduction in computation time is expected.

To implement OS-EM in TITAN-IR, a loop was added within the outer reconstruction iteration loop to step through the subsets $S_1, S_2, \ldots, S_{N_{subsets}}$ as depicted in Fig. 7.1. Each loop through a subset S_k is referred to as a sub-iteration k and a full iteration i is only completed when all of the subsets have been iterated through. The angles can be grouped into subsets in any number of ways, but dividing the angles equally into subsets of opposing angles was recommended in the literature and, therefore, chosen for this application. The TITAN-IR code groups the opposing angles into subsets and only uses the angles assigned to the current subset for each sub-iteration. The source estimate $\lambda^{(k)}$ is updated after each sub-iteration k. Note that the number of subsets must divide evenly into the number of projection angles. A traditional ML-EM reconstruction can be done by specifying 1 subset.

7.3 Quality Metrics

Several quality metrics are calculated for each iteration in TITAN-IR to assist in evaluating how well the reconstruction algorithm is functioning. Image quality in nuclear medicine is typically measured by spatial resolution, contrast and noise[1]. Spatial resolution indicates the image sharpness or detail and is primarily limited by collimator resolution.

Collimator resolution can be improved with smaller collimator holes, but this is at the expense of collimator efficiency and, therefore, increased noise. While it is important that the model properly represents the collimator resolution, this is not a relevant metric for evaluating the new image reconstruction algorithm; however, contrast and noise are important values to consider, in particular with relation to iteration number. The following image quality metrics are calculated by TITAN-IR.

Differences in image intensity in adjacent regions of an image are referred to as contrast[3]. In nuclear medicine, these differences in intensity correspond to levels of radioactive uptake in the patient and, therefore, number of disintegrations. The contrast in a region *l* can be defined as

$$C_l = \frac{\bar{I}_l - \bar{I}_0}{\bar{I}_0} \tag{7.4}$$

where $\bar{I}_l$ is the average image intensity in a region of interest, e.g., a lesion, and $\bar{I}_0$ is the average reference background intensity, e.g., normal tissue. For contrast calculations, TITAN-IR allows the user to specify multiple circular regions of interest and a reference background region, as described further in Appendix B. The TITAN-IR code prints out the contrast for each lesion for every iteration.

In ML-EM or OS-EM reconstruction, the increase of noise with number of iterations is an important metric to consider. The noise is estimated for a background region of the reconstructed image as a measure of this and is given by

$$noise = \frac{1}{\bar{I}_0}\sqrt{\frac{\sum_{i=1}^{N_V}(I_i - \bar{I}_0)^2}{N_V - 1}} \tag{7.5}$$

where the I_i is the value in voxel i of the measured background region, $\bar{I}_0$ is the average intensity, and N_V is the number of voxels in the background region. This metric is output for every iteration.

The above metrics are used to directly evaluate the reconstructed image. The sinogram generated by the forward projection step was also evaluated by considering the mean squared error (MSE) and mean relative error (MRE) relative to the measured sinogram data. The MSE is given by

$$MSE = \frac{1}{N_d} \sum_{d}^{N_d} \left(\hat{n}_d^{(i)} - n_d^* \right)^2, \tag{7.6}$$

where $\hat{n}_d^{(i)}$ is the counts in detector element d at iteration i, n_d^* is the measured counts in detector element d, and N_d is the total number of detector pixels. The MRE is given by

$$MRE = \frac{1}{N_d} \sum_{d}^{N_d} \left| \frac{\hat{n}_d^{(i)} - n_d^*}{n_d^*} \right|, \tag{7.7}$$

where the variables are the same as in Eq. 7.6.

Chapter 8

Analysis of TITAN-IR

In this chapter, the TITAN-IR code is used to reconstruct the source distribution of two phantoms: a quality assurance phantom and an anatomical torso phantom. The sensitivity of the reconstruction to deterministic parameters, noisy projection data, and collimator blur is considered. Results will also be compared with FBP and ML-EM reconstruction with the system matrix only.

8.1 Jaszczak Phantom with Cold Spheres

The Data Spectrum Corporation's Jaszczak phantom is a popular phantom for quality assurance in nuclear medicine. This cylindrical phantom consists of two regions: the lower half with numerous rods of varying sizes and the upper half with six spheres of different radii. The upper half of the phantom is modeled for this research with cold

spheres, i.e., spheres with no source, in a uniform background source of Tc-99m. A 3-dimensional depiction of this geometry is given in Fig. 8.1. A slice through the center of the source distribution is shown in Fig. 8.2.

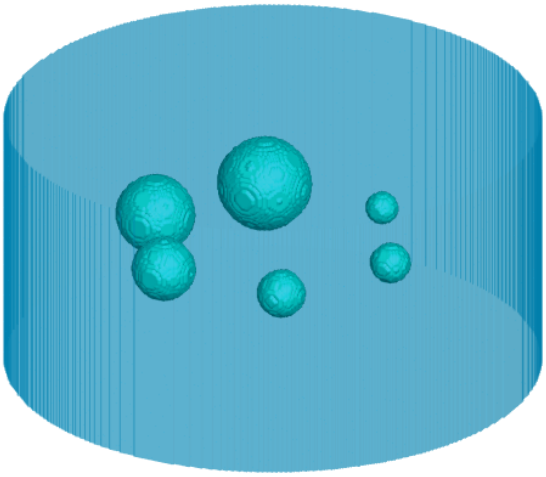

Figure 8.1: Geometry of Jaszczak cylindrical phantom with cold spheres

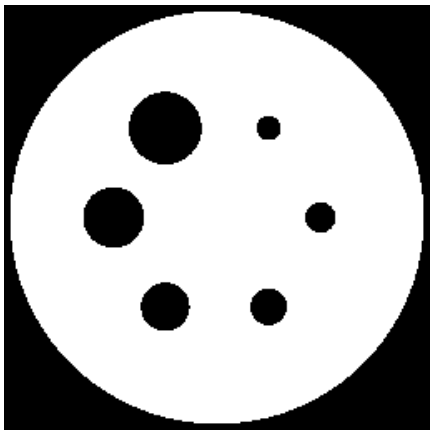

Figure 8.2: Source distribution in center slice of Jaszczak cylindrical phantom with cold spheres

The phantom cylinder has an outer diameter of 22.24 cm and is 11.12 cm tall. The cylinder walls are 0.32 cm thick and made of PMMA (polymethyl methacrylate), as are the cold spheres. The cold spheres have radii of 0.635, 0.795, 0.955, 1.27, 1.59, and 1.9 cm. The phantom is then filled with water mixed with Tc-99m.

A flat source distribution of one is used for the initial guess of all reconstructions. The system matrix is obtained using the Image Reconstruction Toolbox[36] for MATLAB and models attenuation and, where applicable, depth-dependent collimator blur. The SIMIND Monte Carlo code is used to generate the "measured" projection data for three different conditions: i) noiseless projection data with no collimator blur, ii) noisy projection data with no collimator blur, and iii) noisy collimated projection data. Each projection

image is 64×32 pixels with pixel dimensions of $0.3475 \times 0.3475\ cm^2$ and data is obtained at 64 angles over 360° as recommended by AAPM (American Association of Physicists in Medicine) Report No. 52[72] on *Quantitation of SPECT Performance*. The radius of rotation, i.e., distance from the phantom center to the detector normal, is 16 cm. A summary of the Jaszczak phantom parameters is given in Table 8.1

Table 8.1: Summary of Jaszczak phantom parameters

Phantom outer/inner diameter	$22.24\ cm/21.60\ cm$
Phantom height	$11.12\ cm$
Cold sphere radii	$0.635, 0.795, 0.955, 1.27, 1.59, 1.9\ cm$
Detector pixels	64×32
Detector pixel size	$0.3475 \times 0.3475\ cm^2$
Projection angles	64

For the deterministic calculation, cross sections were generated using the CEPXS code[59]. The source energy group is 126.45-154.55 keV to account for a typical SPECT energy window of 20% and the mean free path of photons in the phantom is 6.57 cm. The flux tolerance for the transport calculation in the phantom was 10^{-3}. The origins of the cold spheres and their radii are given in the TITAN-IR input to calculated the contrast. The center of the reconstruction is given as the background origin for contrast and noise calculations. No post-reconstruction filtering is applied so that the results of the TITAN-IR reconstruction can be directly assessed.

8.1.1 Noiseless Projection Data with No Collimator Blur

In Chapter 6, the proper selection of deterministic parameters was considered for a 2-dimensional phantom by examining projections generated with the known source distribution. This analysis is repeated for the 3-dimensional Jaszczak phantom and then extended by determining the impact of deterministic parameters on the reconstruction. The noiseless projection data with no collimator blur is used for these studies.

The deterministic parameters to be examined include the mesh size, quadrature order, differencing scheme, and anisotropic scattering order. The three mesh sizes to be used are referred to as coarse (64 x 64 x 32), base (128 x 128 x 64), and fine (256 x 256 x 128) and are depicted in Fig. 8.3.

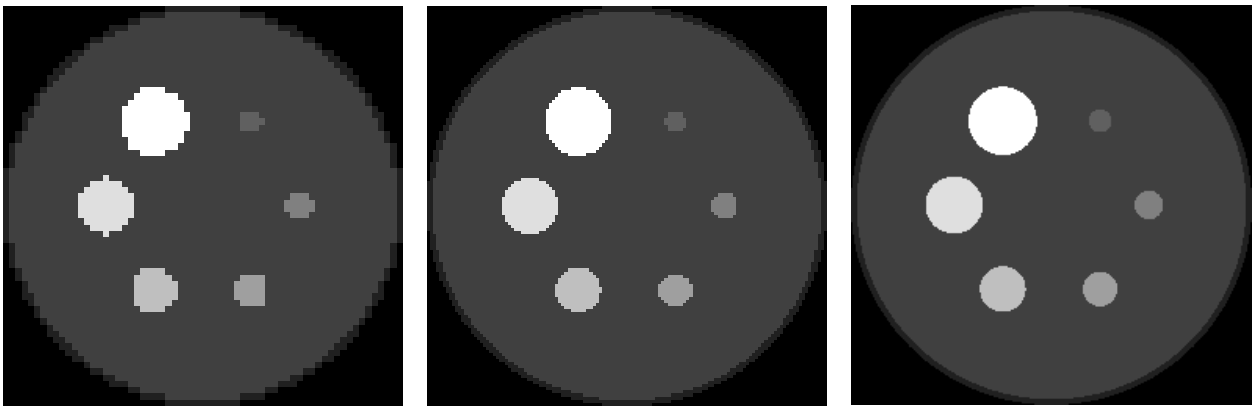

(a) 64 x 64 x 32 meshes (3.475 x 3.475 x 3.475 mm^3)

(b) 128 x 128 x 64 meshes (1.7375 x 1.7375 x 1.7375 mm^3)

(c) 256 x 256 x 128 meshes (0.86875 x 0.86875 x 0.86875 mm^3)

Figure 8.3: Slice through Jaszczak phantom with cold spheres geometry for different mesh sizes with number of meshes and voxel size indicated

Projection image sensitivity studies

For these studies, the actual source distribution, i.e., solution, is used as the input for a TITAN SPECT simulation to examine how the simulated projection images are impacted by deterministic parameter selection as well as how they compare with the SIMIND projection images. The projection images created by TITAN for increasing quadrature order are compared with the TITAN S_{40} solution for the fine meshing and DTW differencing scheme, as given in Table 8.2. The projection images are clearly not strongly impacted by quadrature order and even the S_4 quadrature, with just 3 directions per octant, has a maximum relative difference of only 1% relative to the S_{40} solution. This is due to the widely distributed source and reasonably large amount of scatter in the phantom. The same result was seen for other mesh sizes and the DDZ differencing scheme.

Table 8.2: Maximum relative difference and MSE of TITAN (DTW, fine meshing) sinograms with increasing quadrature order relative to S_{40} solution

Quadrature Order	Directions	Max. Rel. Difference	MSE
S_4	24	1.02%	9.09×10^{-6}
S_6	48	-0.61%	2.25×10^{-6}
S_{10}	120	-0.32%	5.34×10^{-7}
S_{14}	224	-0.21%	1.72×10^{-7}
S_{20}	440	-0.12%	4.48×10^{-8}
S_{28}	840	-0.05%	7.48×10^{-9}

The mesh size was the next parameter considered. The maximum relative difference and mean square error (MSE) of TITAN projections relative to SIMIND for different mesh sizes are given in Table 8.3. As expected, the errors are reduced with mesh refine-

ment. Profiles through projection images were plotted to examine the impact of mesh size in detail. The profiles through row 16 of the projections at 22.5° and 213.75° are given in Fig. 8.4 for TITAN with the coarse, base, and fine meshes and the reference SIMIND solution. The TITAN simulations are for S_{40} and DTW. The profile through the 22.5° projection is an example of a projection where all three meshes follow the SIMIND solution well, but there is clearly improvement with mesh refinement. The profile through the 213.75° projection demonstrates some of the unphysical oscillations that are present when the mesh is too coarse.

Table 8.3: Maximum relative difference and MSE of TITAN (S_{40}, DTW) projections with coarse, base, and fine mesh sizes relative to SIMIND projections

Mesh Type	Max. Rel. Difference	MSE
Coarse (64 x 64 x 32)	-15.3%	3.78×10^{-7}
Base (128 x 128 x 64)	-14.0%	2.54×10^{-7}
Fine (256 x 256 x 128)	-10.7%	2.06×10^{-7}

The TITAN code includes two differencing schemes: diamond differencing with zero fixup (DDZ) and directional theta-weighted (DTW). The DTW scheme generally requires less mesh refinement than DDZ to avoid unphysical oscillations, but, with a fine enough mesh, the DDZ scheme can be more accurate. Also, the DTW simulation takes ~10% longer than the DDZ simulation for this model. Compared with SIMIND, the TITAN DDZ projections have nearly the same maximum relative difference and MSE as the DTW projections for the coarse mesh; however, the DDZ differences are smaller than DTW for the base and fine mesh sizes.

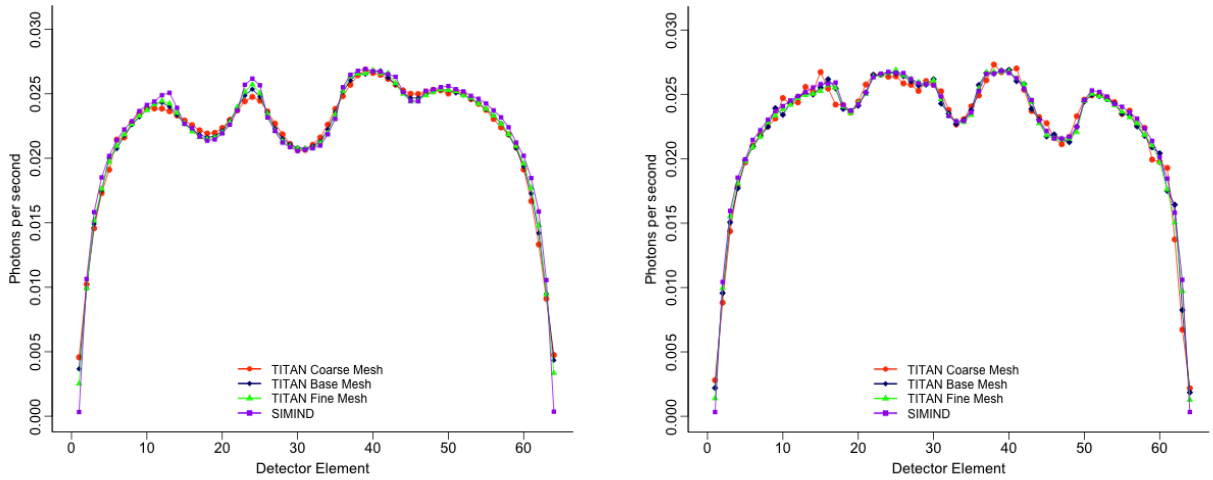

(a) $22.5°$ (b) $213.75°$

Figure 8.4: Profiles through row 16 of projection images generated by SIMIND and TITAN (S_{40}, DTW) with different mesh sizes

Profiles through row 16 of the $67.5°$ projection from SIMIND, TITAN with DDZ, and TITAN with DTW are given in Fig. 8.5 for the coarse and base meshes. In Fig. 8.5a the DDZ scheme clearly results in unphysical oscillations due to the coarse meshing, while the DTW solution is smooth. By doubling the number of meshes, in Fig. 8.5b the DDZ profile has fewer oscillations and in some places matches the SIMIND solution more closely than the DTW profile. These results demonstrate the trade-offs between the DDZ and DTW differencing schemes.

The previous simulations were all done with a P_1 anisotropic scattering order. The maximum relative difference between the P_1 and P_3 projection images was 1.5% for the base meshing with S_{20} and DTW. Based on these studies, a quadrature as low as S_6 or S_4 may be used and the DTW scheme with the coarse mesh is adequate. The base or fine meshing would have to be used if one desired to use the DDZ scheme.

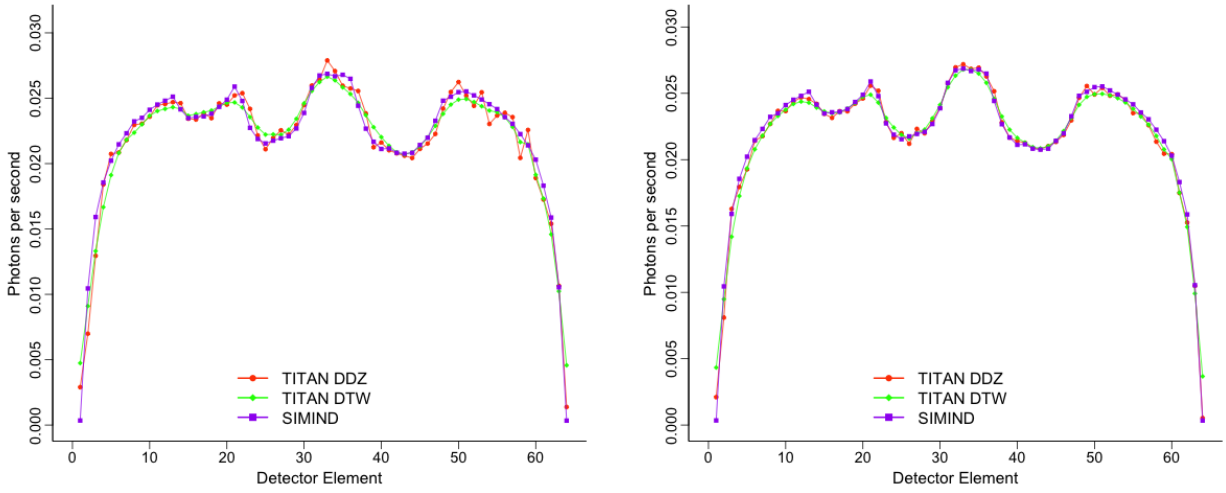

(a) Coarse mesh (b) Base mesh

Figure 8.5: Profiles through row 16 of projection images generated by SIMIND and TITAN using the DDZ and DTW differencing schemes

Reconstruction sensitivity studies

The impact of deterministic parameter selection on image reconstruction was considered in detail. In the reconstructed images, the cold sphere contrast and the log-likelihood function were calculated. The MSE, mean relative error (MRE), and maximum relative difference in the generated sinograms relative to the reference SIMIND sinogram were also calculated. The following studies all use the DTW differencing scheme. The oscillations in the DDZ scheme for the coarse mesh caused the reconstruction to diverge.

The contrast of the largest cold sphere after 40 iterations is given in Table 8.4 for TITAN-IR with different quadratures and meshes. The MSE and MRE of the projections generated by TITAN-IR after 40 iterations relative to the reference SIMIND projections are given in Table 8.5 and Table 8.6, respectively. Tables 8.4, 8.5, and 8.6 indicate that the reconstruction is not sensitive to quadrature order and that a low quadrature order may

be used to reduce computation time. The choice of anisotropic scattering order was also found to result in only small changes in the examined metrics for $P_0, P_1, P_3,$ and P_5. The MSE and MRE are reduced with mesh refinement, but not significantly. The maximum relative difference was approximately -25%, -20%, and -17% for the coarse mesh, base mesh, and fine mesh, respectively. The log-likelihood function was calculated and found to be essentially constant for all three meshes, quadrature orders from S_4 to S_{40}, and anisotropic scattering order.

Table 8.4: Contrast of largest cold sphere after 40 iterations in TITAN-IR

Quadrature Order	Coarse Mesh (64 x 64 x 32)	Base Mesh (128 x 128 x 64)	Fine Mesh (256 x 256 x 128)
S_4	-0.784	-0.774	-0.768
S_6	-0.784	-0.774	-0.767
S_{14}	-0.784	-0.774	-0.767
S_{28}	-0.784	-0.773	-0.767

Table 8.5: MSE of projection images relative to SIMIND after 40 iterations in TITAN-IR

Quadrature Order	Coarse Mesh (64 x 64 x 32)	Base Mesh (128 x 128 x 64)	Fine Mesh (256 x 256 x 128)
S_4	3.38×10^{-7}	2.44×10^{-7}	2.18×10^{-7}
S_6	3.32×10^{-7}	2.39×10^{-7}	2.15×10^{-7}
S_{14}	3.29×10^{-7}	2.36×10^{-7}	2.36×10^{-7}
S_{28}	3.28×10^{-7}	2.35×10^{-7}	2.11×10^{-7}

The center slices (slice 16) of the reconstructed source distributions at 5, 10, 20, and 40 iterations are given in Figs. 8.6, 8.7, and 8.8 for coarse, base, and fine meshes, respectively, for S_6. No significant differences are visible between the coarse, base, and

Table 8.6: MRE of projection images relative to SIMIND after 40 iterations in TITAN-IR

Quadrature Order	Coarse Mesh (64 x 64 x 32)	Base Mesh (128 x 128 x 64)	Fine Mesh (256 x 256 x 128)
S_4	1.88%	1.64%	1.55%
S_6	1.86%	1.63%	1.54%
S_{14}	1.85%	1.61%	1.52%
S_{28}	1.85%	1.61%	1.51%

fine meshes, although the fine mesh image background appears to be smoother. The ring artifact does appear to be reduced in magnitude by mesh refinement.

Profiles through the center of the source distributions are used to examine the reconstructions in more detail. These profiles pass horizontally through the 3.18 cm and 1.59 cm diameter cold spheres. All source distributions were normalized to a total activity of 185 MBq, which was the activity simulated to acquire the SIMIND projections. Fig. 8.9 gives profiles for coarse, base, and fine meshes with S_6 and DTW after 40 iterations along with the reference solution. The ring artifact is largest for the coarse mesh and becomes more narrow with mesh refinement. The coarse and base mesh results show oscillations in the phantom center in particular, while the fine mesh is smoother.

Profiles through the center of the reconstructed source distribution with the coarse mesh, S_6, and DTW are given in Fig. 8.10 for different numbers of iterations. The oscillations in the phantom center develop with increasing iterations, which is consistent with the noisy behavior of the ML-EM algorithm. The maximum relative difference in the image estimate at iteration 40 is -3.13% relative to the previous iteration. Fig. 8.11 gives

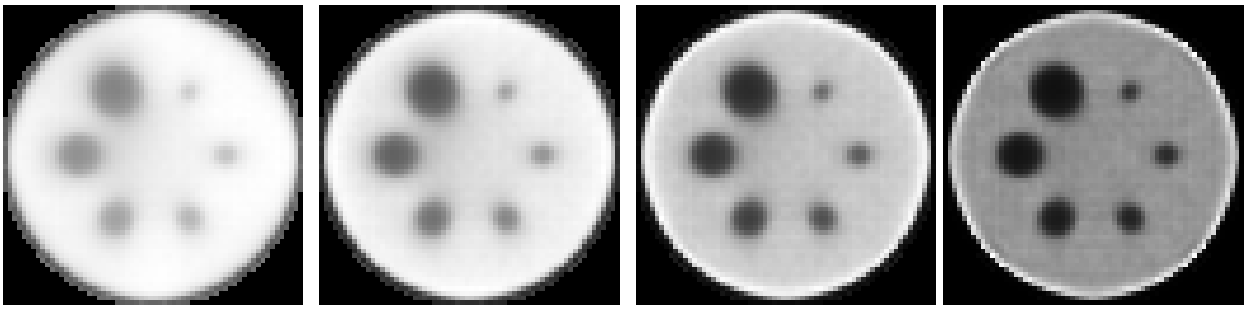

(a) 5 iterations (b) 10 iterations (c) 20 iterations (d) 40 iterations

Figure 8.6: Central slice of source distribution reconstructed with TITAN-IR (S_6) coarse mesh

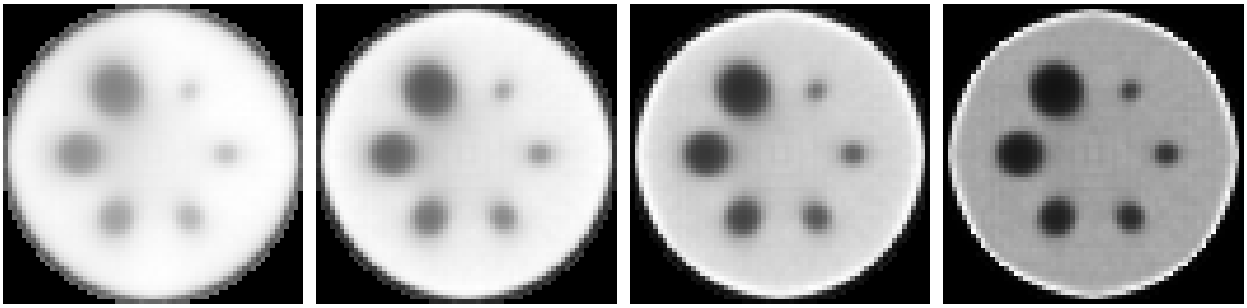

(a) 5 iterations (b) 10 iterations (c) 20 iterations (d) 40 iterations

Figure 8.7: Central slice of source distribution reconstructed with TITAN-IR (S_6) base mesh

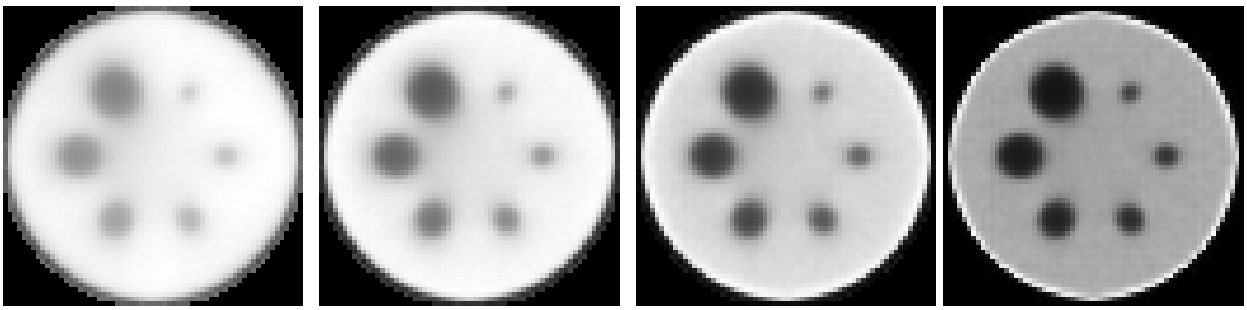

(a) 5 iterations (b) 10 iterations (c) 20 iterations (d) 40 iterations

Figure 8.8: Central slice of source distribution reconstructed with TITAN-IR (S_6) fine mesh

the contrast in each of the cold spheres in the center slice of reconstructed images as a function of iteration number. The MRE of the projection images created in each iteration relative to the reference SIMIND data is given in Fig. 8.12 for each meshing. The MRE has

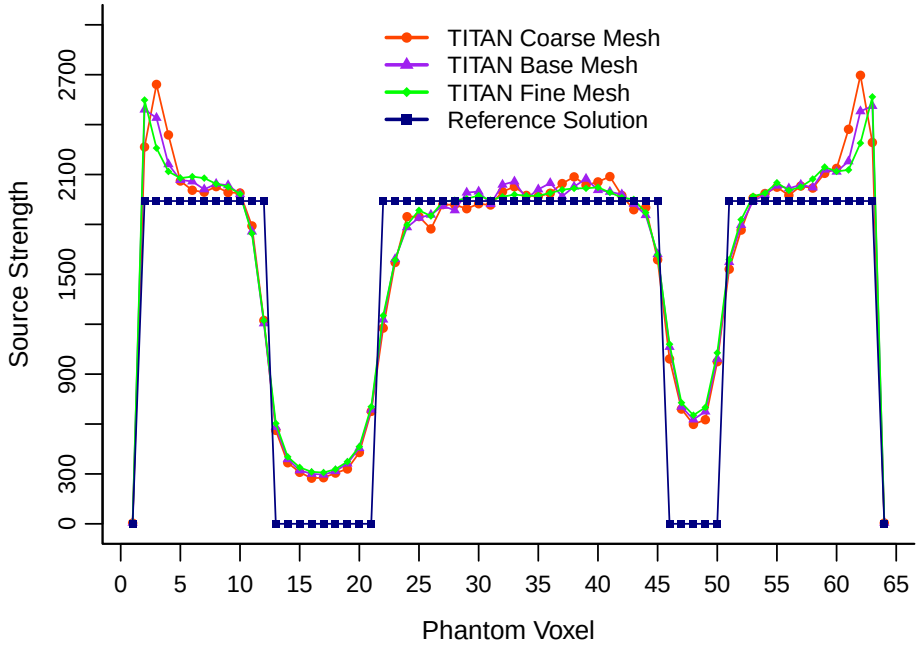

Figure 8.9: Profile through center of reconstructed source distribution with coarse, base, and fine meshes (40 iterations, S_6)

leveled off by around 24 iterations and the slight improvement with mesh refinement is apparent.

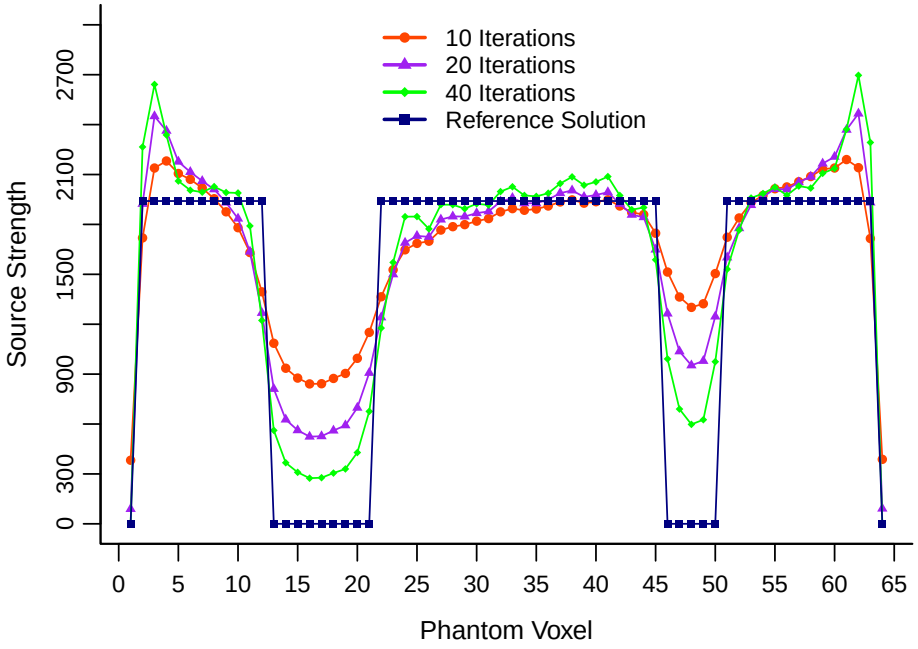

Figure 8.10: Profile through center of reconstructed source distribution for 10, 20, and 40 iterations (S_6, coarse mesh)

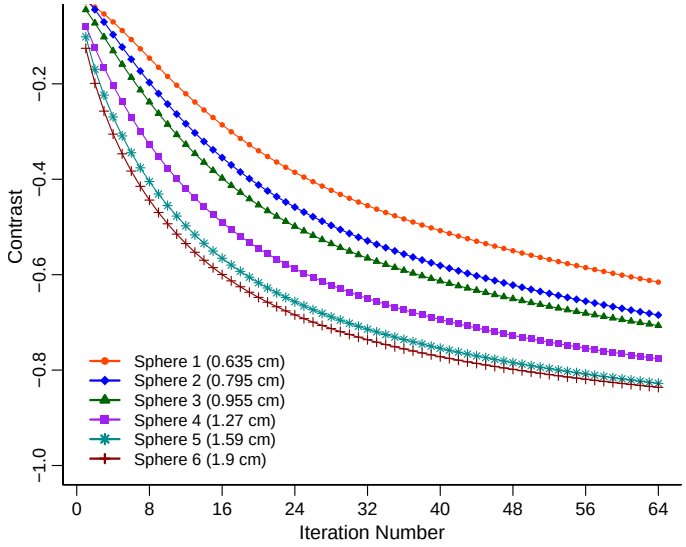

Figure 8.11: Contrast of each cold sphere (radius) in center slice of TITAN-IR (S_6) image

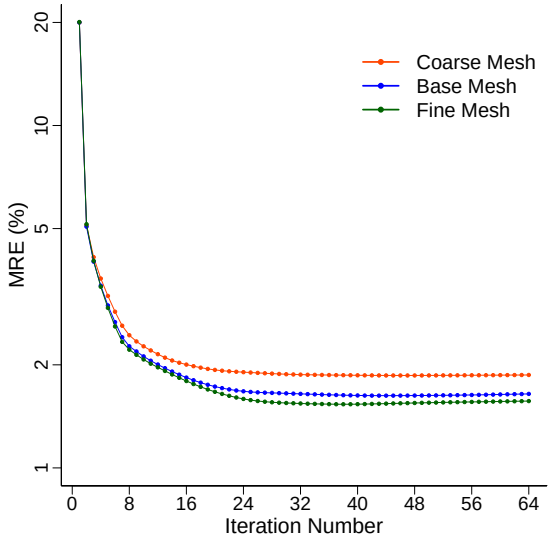

Figure 8.12: MRE in TITAN-IR (S_6) projection data relative to SIMIND data

8.1.2 Noisy Projection Data with No Collimator Blur

SPECT measured projection data tends to be noisy due to the limited counts reaching the detector for a particular activity and acquisition time. The simulated data from SIMIND has been generated essentially free of noise by using long simulation times. A more realistic simulation will have noise typical to a SPECT study.

AAPM Report No. 52[72] on *Quantitation of SPECT Performance* was used to provide guidelines for the number of counts at the detector. For assessing system performance with the Jaszczak phantom, the report recommends a Tc-99m activity of 300-370 MBq and an acquisition time per angle based on the time to 500,000 counts at the first angle. Since this simulation considers only the upper half of the Jaszczak phantom, an activity of 185 MBq is used in the SIMIND simulation and the resulting projection data was scaled to a total of $(2.5 \times 10^5) \times$ `num_angles` or 1.6×10^7 counts. The *poisson()* function from the Image Reconstruction Toolbox[36] was then used to generate Poisson random data with the scaled SIMIND data as the mean. As a comparison, the 90° projection images with no noise and with noise are given in Figs. 8.13 and 8.14, respectively.

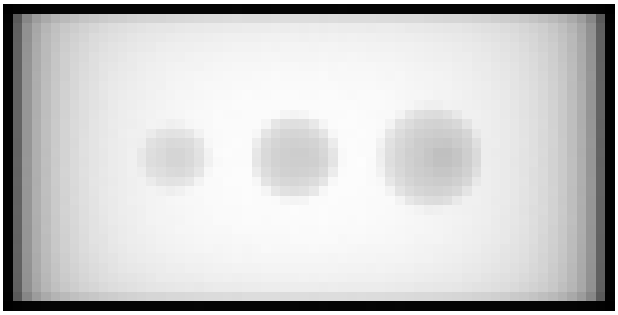

Figure 8.13: SIMIND noiseless projection image at 90°

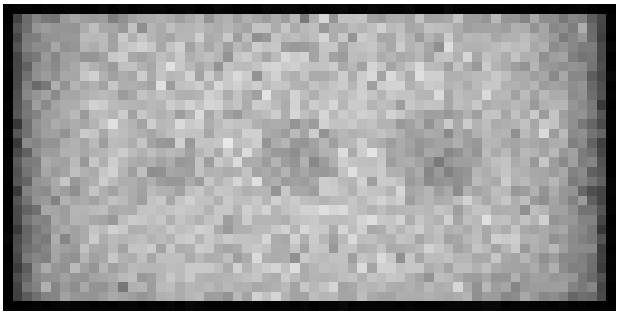

Figure 8.14: SIMIND noisy projection image at 90°

The impact of reconstruction parameters on reconstructed image quality with the noisy projection data with no collimator blur was examined. As with the noiseless projection data, the quadrature order was found to have no impact. The MSE, MRE, and background noise are given in Table 8.7 for 40 iterations with coarse, base, and fine meshes. The mesh refinement in the TITAN model led to a slightly more accurate reconstruction with reduced background noise.

Table 8.7: MSE, MRE, and background noise after 40 iterations in TITAN-IR (S_6) with noisy projection data with no collimator blur

Quality Metric	Coarse Mesh (64 x 64 x 32)	Base Mesh (128 x 128 x 64)	Fine Mesh (256 x 256 x 128)
MSE	1.26×10^2	1.14×10^2	1.08×10^2
MRE	6.88%	6.58%	6.42%
Noise	28.3%	27.5%	26.5%

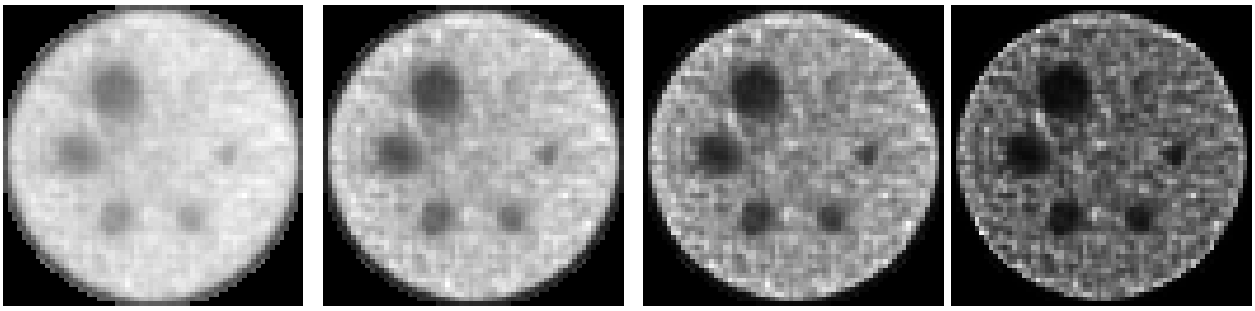

(a) 5 iterations (b) 10 iterations (c) 20 iterations (d) 40 iterations

Figure 8.15: Central slice of source distribution reconstructed with TITAN-IR (S_6, coarse mesh) from noisy projection data with no collimator blur

Given the limited improvement with mesh size, the noisy SIMIND projection data was reconstructed by TITAN-IR for S_6 and coarse meshing. The maximum relative difference in the image estimate at iteration 40 is -2.82% relative to the previous iteration.

The center slices, i.e., slice 16, of the reconstructed images after 5, 10, 20, and 40 iterations are given in Fig. 8.15. The impact of the noisy projection data on the reconstructed images is apparent, and the noise increases with iterations. The smallest cold sphere cannot be clearly identified, but the rest of the spheres are clearly visible in the reconstruction.

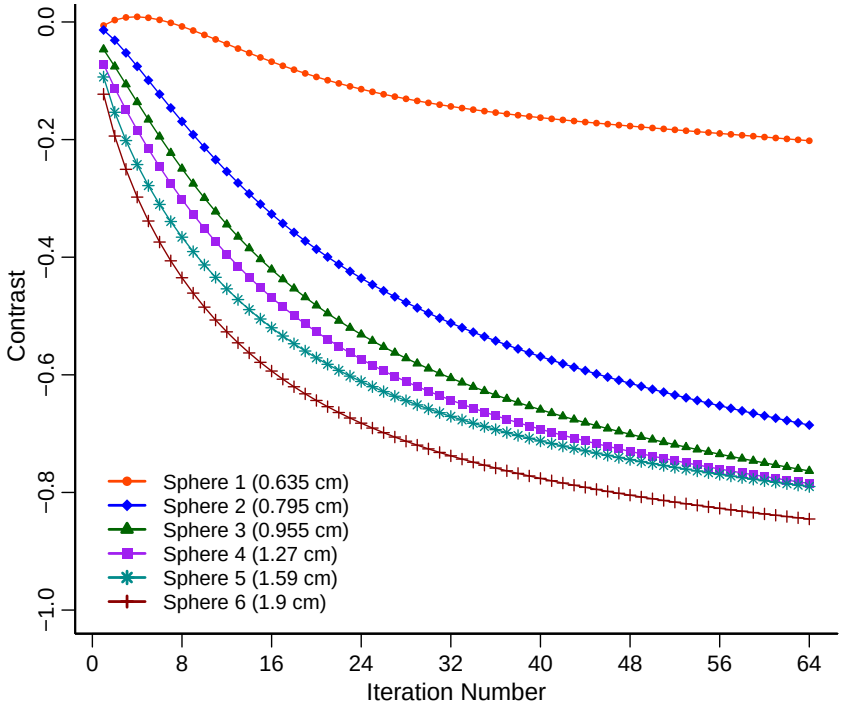

Figure 8.16: Contrast in each sphere (radius) for noisy projection data with no collimator blur (S_6, coarse mesh)

The contrast in each cold sphere is given in Fig. 8.16 as a function of iteration number. The addition of noise to the projection data has not greatly changed the contrast, except for Sphere 1 which the code is struggling to reconstruct. For example, the Sphere 5 contrast is -0.766 for reconstruction with noiseless projection data and -0.712 for noisy data.

8.1.3 Noisy Collimated Projection Data

The General Electric low-energy general purpose (GE-LEGP) and Siemens low-energy high resolution (SE-LEHR) collimators were chosen for reconstruction of collimated projection data. The parameters for these collimators are given in Table 8.8 and they both have hexagonal holes. To allow room for the collimator between the detector and the phantom, the detector radius of rotation was increased from 16 cm to 20.1 cm for the GE-LEGP collimator and 18.2 cm for the SE-LEHR collimator. The reference "measured" projection data is generated by SIMIND and the 90° projections for the GE-LEGP and SE-LEHR collimators are given in Figs. 8.17 and 8.18, respectively, after noise has been added. Poisson noise was added to the projections following the same procedure described in Section 8.1.2. SIMIND produces projection data that correspond to 1 second of acquisition time per projection angle so regardless of the activity simulated the resulting data must be scaled to the recommended value of 2.5×10^5 counts in the first projection. To achieve this number of counts, each projection image would need to be acquired for 20 seconds with the GE-LEGP colllimator and 36 seconds with the SE-LEHR collimator.

Table 8.8: Collimator parameters

Collimator	Hole Diameter	Septa Thickness	Length
GE-LEGP	0.25 cm	0.03 cm	4.10 cm
SE-LEHR	0.111 cm	0.016 cm	2.405 cm

To account for collimator blur in the system matrix, point-spread functions (PSFs) were obtained at different distances from each collimator using SIMIND. A PSF is the image produced at a detector from a single point source and describes the blurring prop-

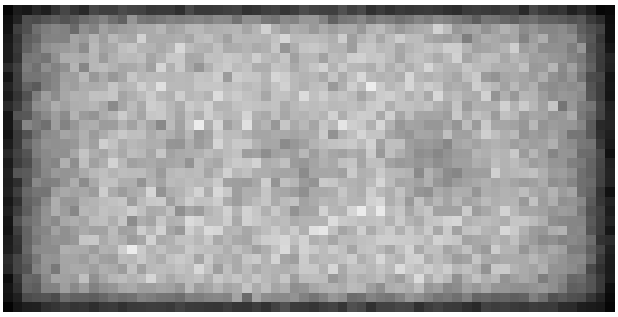

Figure 8.17: SIMIND noisy projection image at 90° for GE-LEGP collimator

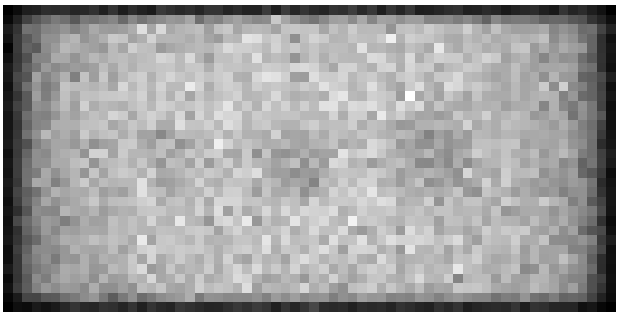

Figure 8.18: SIMIND noisy projection image at 90° for SE-LEHR collimator

erties of an imaging system[3]. The PSF information is then passed to the Image Reconstruction Toolbox[36] to incorporate depth-dependent collimator response into the system matrix it generates.

In TITAN-IR, the formulation described in Section 3.2.3 is used to represent the collimator. It has been shown that the geometric response function, which describes the probability that a photon will pass through the collimator, for hexagonal holes can be approximated using round holes with the same area[73]. Since the collimator representation in TITAN is based on circular collimator holes, the equivalent hole area was used to determine an acceptance angle of 1.83° or 3.20×10^{-2} radians for the GE-LEGP collimator and 1.39° or 2.42×10^{-2} radians for the SE-LEHR collimator. One circle with 6 split directions is used for the both TITAN COS collimator representations.

GE-LEGP collimator

With the addition of collimator blur to the model, the reconstruction remains largely insensitive to quadrature order, anisotropic scattering order, and mesh refinement. For S_6

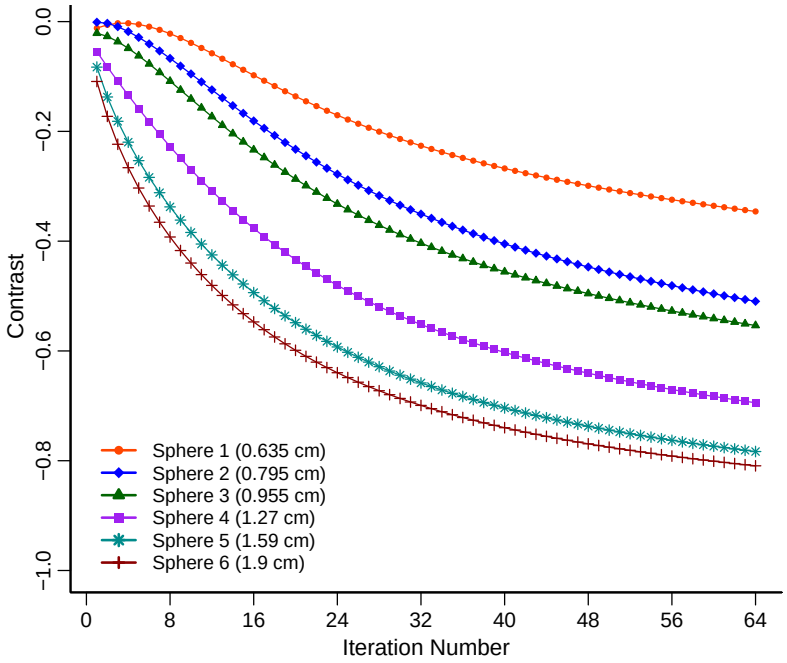

Figure 8.19: Contrast in each sphere (radius) for noisy GE-LEGP projection data (S_6, coarse mesh)

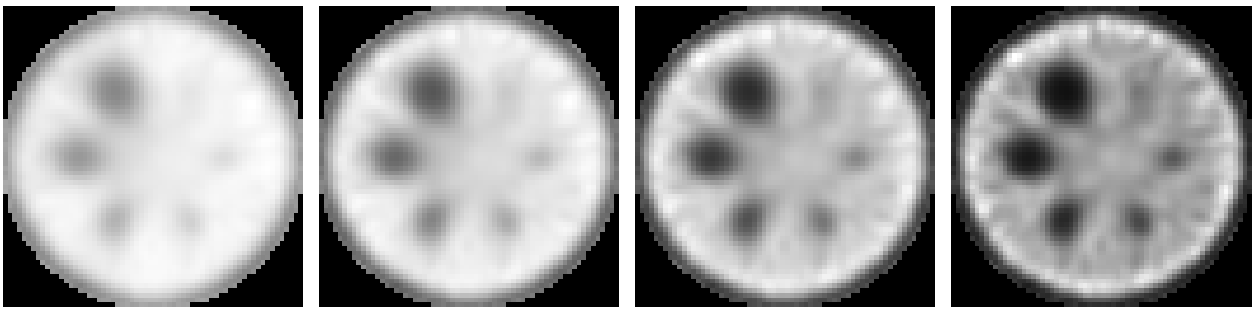

(a) 5 iterations (b) 10 iterations (c) 20 iterations (d) 40 iterations

Figure 8.20: Central slice of source distribution reconstructed with TITAN-IR (S_6, coarse mesh) from noisy GE-LEGP projection data

quadrature, P_1 scattering, and coarse meshing, the projection MRE is 8.64% and the estimated background noise is 5.59% after 40 iterations. The maximum relative difference in the image estimate at iteration 40 is -2.65% relative to the previous iteration. The contrast in each cold sphere for TITAN-IR images from the noisy GE-LEGP collimated projection

data is given in Fig. 8.19 as a function of iteration number. In general, the addition of collimator blur has reduced the contrast in the cold spheres, with the exception of Sphere 1. The center slices of the reconstructed images after 5, 10, 20, and 40 iterations are given in Fig. 8.20. The blur due to the collimator appears to help with the projection noise in the reconstruction, which is significantly less noisy than reconstruction without collimator blur.

SE-LEHR collimator

The SE-LEHR collimator has a smaller acceptance angle than the GE-LEGP collimator and this results in improved contrast, as seen in Fig. 8.21. For S_6 quadrature, P_1 scattering, and coarse meshing, the projection MRE is 8.16% after 40 iterations. The maximum

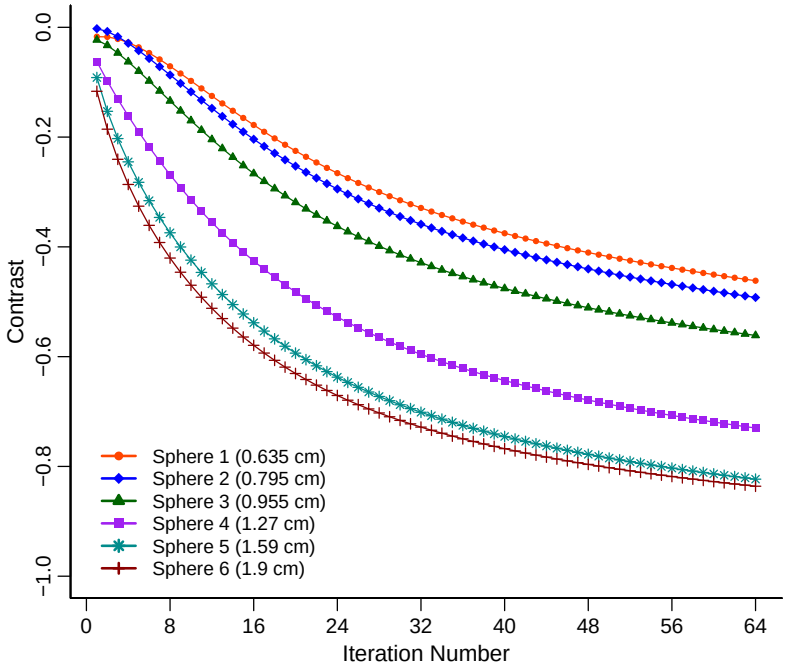

Figure 8.21: Contrast in each sphere (radius) for noisy SE-LEHR projection data (S_6, coarse mesh)

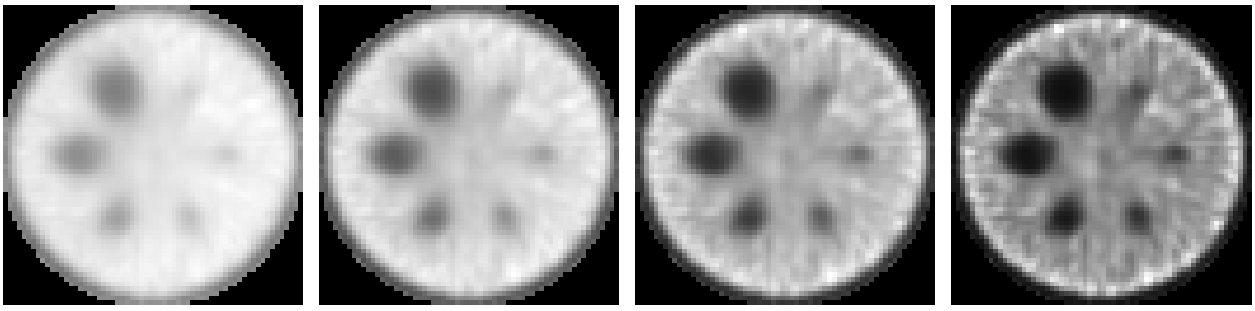

(a) 5 iterations (b) 10 iterations (c) 20 iterations (d) 40 iterations

Figure 8.22: Central slice of source distribution reconstructed with TITAN-IR (S_6, coarse mesh) from noisy SE-LEHR projection data

relative difference in the image estimate at iteration 40 is 3.73% relative to the previous iteration. The central slices of reconstructed images after 5, 10, 20, and 40 iterations are given in Fig. 8.22 for noisy SE-LEHR projection data. Note that all six spheres are now clearly visible with the higher spatial resolution of this collimator. Due to the reduction in collimator blur, these images are noisier than the GE-LEGP images; the background noise was calculated to be 10.2%.

Noise sensitivity

The sensitivity of the reconstruction to projection noise, i.e., the number of counts at the detector, was studied for the GE-LEGP collimated data. Of course, the trade-off with obtaining more counts at the detector is reduced noise for a longer acquisition time. The cases considered are summarized in Table 8.9. The base count case is the AAPM Report No. 52 recommended value described in Section 8.1.2 and this value is doubled for the high count/low noise case and halved for the low count/high noise case.

Table 8.9: Summary of cases with different noise levels

Case	Avg. counts per projection	Acquisition time per projection
Low count	1.25×10^5	10 seconds
Base count	2.5×10^5	20 seconds
High count	5.0×10^5	40 seconds

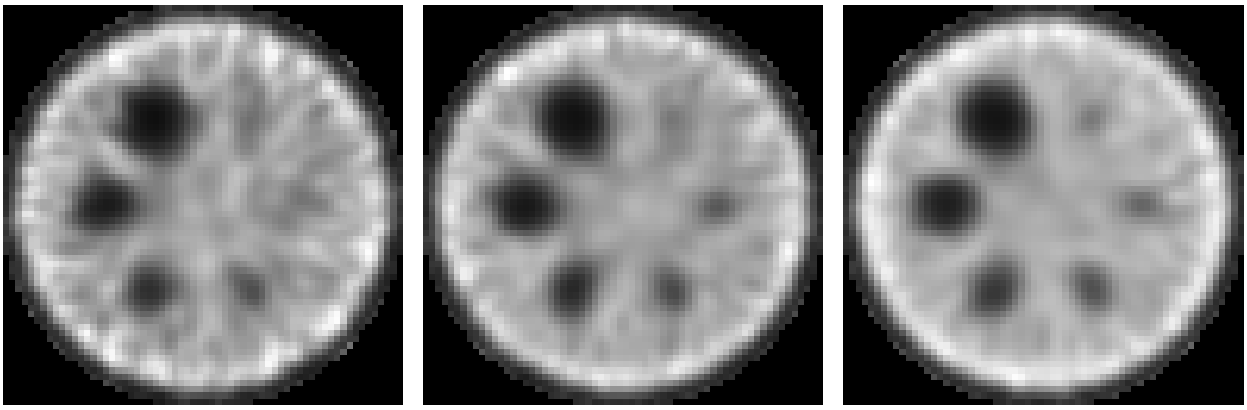

(a) Low count data (b) Base count data (c) High count data

Figure 8.23: Reconstruction central slice after 40 iterations with GE-LEGP (S_6, coarse mesh)

The central slice after 40 iterations is given in Fig. 8.23 for the low count, base count, and high count projection data. The improvement with increasing counts is clear. The background noise in the low count, base count, and high count reconstruction is 6.0%, 5.6%, and 4.4%, respectively, with corresponding MRE of 11.4%, 8.6%, and 6.8%.

8.1.4 Comparison with Other Reconstruction Methods

More traditional methods were also used to reconstruct the Jaszczak phantom and provide a reference for the TITAN-IR images. Filtered backprojection (FBP) was implemented slice-by-slice using the *iradon* function in MATLAB and the Chang attenuation

correction[74]. A standard ML-EM reconstruction algorithm was written in Fortran 90 to use the same system matrix (SM) utilized in TITAN-IR.

The three reconstruction cases examined earlier are compared: i) noiseless projection data with no collimator blur, ii) noisy projection data with no collimator blur, and iii) noisy collimated projection data. The central slice of the images reconstructed by FBP, ML-EM with the SM only, and TITAN-IR are given in Figs. 8.24, 8.25, 8.26, and 8.27 for noiseless projection data, noisy projection data, noisy GE-LEGP projection data, and noisy SE-LEHR projection data, respectively. The iterative reconstructions are shown after 40 iterations and all TITAN-IR reconstructions are for S_6, DTW, and coarse meshing. The SM only reconstruction and the TITAN-IR reconstruction look very similar, while the FBP reconstruction struggles with the noisy projection data.

The contrast in each of the cold spheres for FBP is given in Table 8.10 for noiseless data with no collimator blur, noisy data with no collimator blur, and noisy GE-LEGP collimated projection data. For comparison, TITAN-IR has higher contrast in all six spheres after 53 iterations for the noiseless projection data, 50 iterations for the noisy data excluding the smallest sphere, and 49 for the noisy GE-LEGP collimated data. These numbers would imply that the FBP reconstruction is performing well; however, Figs. 8.25, 8.26, and 8.26 indicate that the noise in the FBP reconstruction is significantly degrading the images. The background noise of the FBP images was 55% for the noisy projections with no collimator blur and 45% for the noisy projections with the GE-LEGP collimator, respectively. Clearly, no single metric can be used to evaluate an image.

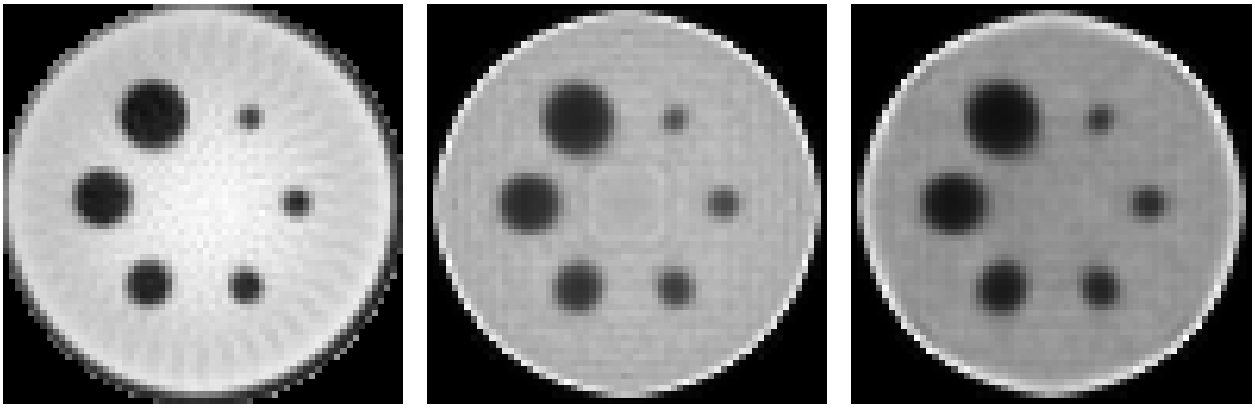

(a) Filtered backprojection (b) System matrix only (c) TITAN-IR

Figure 8.24: Central slice of reconstruction of noiseless projection data

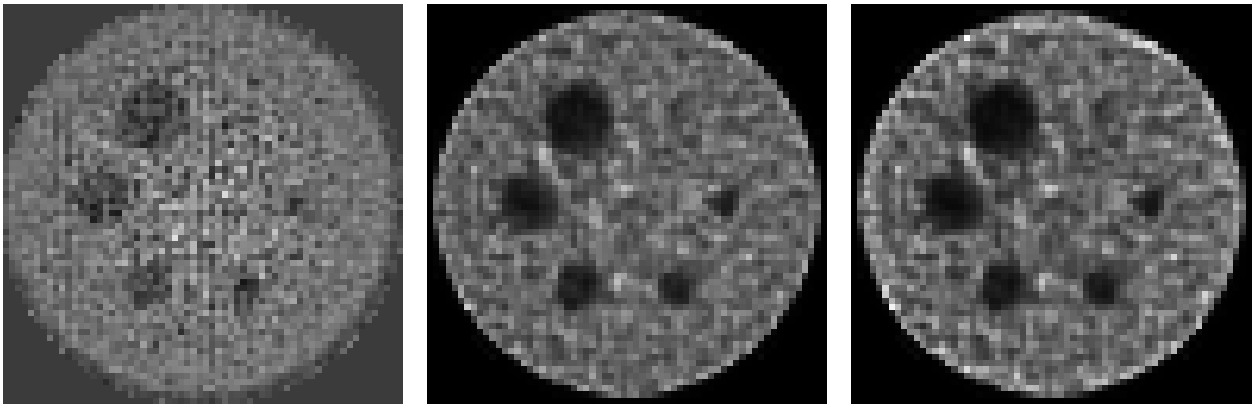

(a) Filtered backprojection (b) System matrix only (c) TITAN-IR

Figure 8.25: Central slice of reconstruction of noisy projection data

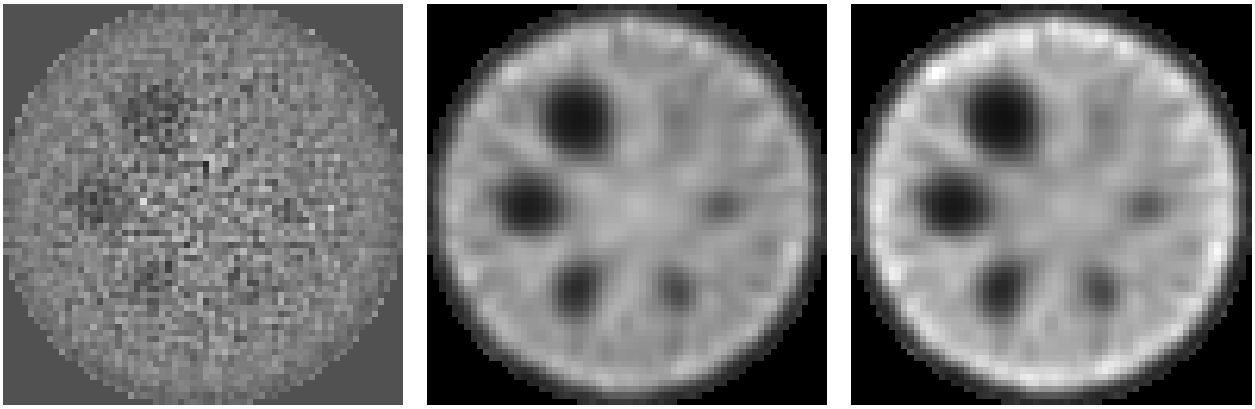

(a) Filtered backprojection (b) System matrix only (c) TITAN-IR

Figure 8.26: Central slice of reconstruction of noisy GE-LEGP collimator projection data

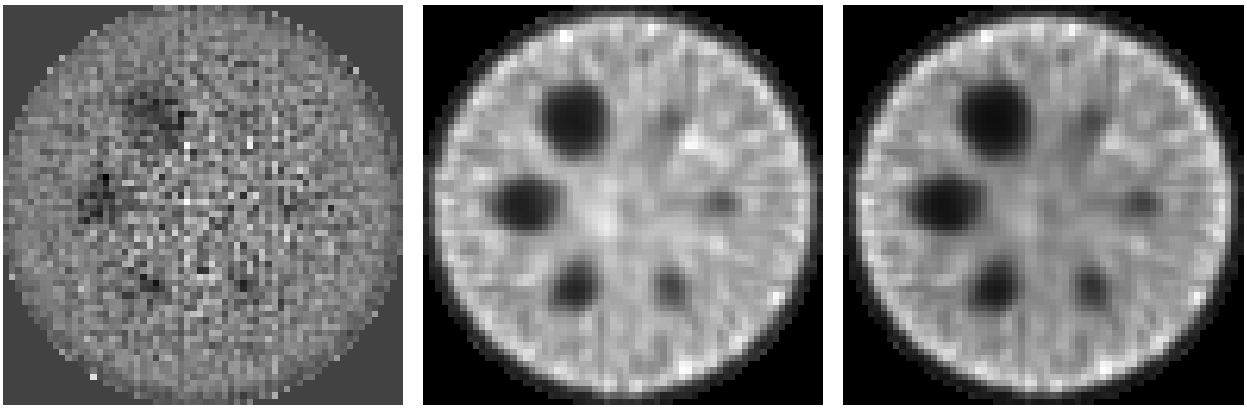

(a) Filtered backprojection (b) System matrix only (c) TITAN-IR

Figure 8.27: Central slice of reconstruction of noisy SE-LEHR collimator projection data

Table 8.10: Contrast in cold spheres after FBP reconstruction of noiseless, noisy, and noisy GE-LEGP collimated projection data

Sphere (radius)	Noiseless projections, no collimator blur	Noisy projections, no collimator blur	Noisy GE-LEGP collimated projections
1 (0.635 cm)	-0.572	-0.351	-0.235
2 (0.795 cm)	-0.616	-0.589	-0.441
3 (0.955 cm)	-0.613	-0.698	-0.484
4 (1.27 cm)	-0.661	-0.633	-0.603
5 (1.59 cm)	-0.730	-0.704	-0.687
6 (1.90 cm)	-0.765	-0.780	-0.713

The cold sphere contrast in the center slice for reconstruction with the SM only and with TITAN-IR (S_6, DTW, and coarse mesh) is compared in Figs. 8.28, 8.29, 8.30, and 8.31. For noiseless projection data with no collimator blur, Fig. 8.28, the contrast improves at a greater rate with TITAN-IR than with the SM only. When noise is added to the projection data, Fig. 8.29, the contrast of the SM only reconstruction no longer shows a smooth and steady improvement and both methods indicate difficulty resolving the smallest sphere. The contrast converges at a slower rate with the addition of collimator

blur in Figs. 8.30 and 8.31. In all cases, the TITAN-IR contrast converges smoothly. In comparison with the SM only results, the TITAN-IR contrast initially converges more slowly but always surpasses the SM only contrast given enough iterations.

To further analyze the reconstructed noisy GE-LEGP projection data, profiles through all six cold spheres are given in Fig. 8.32 for FBP, ML-EM with the SM only, and TITAN-IR after 40 iterations along with the actual source. The noise seen in the FBP image slices is even more apparent in the profiles. The SM only and TITAN-IR reconstructions follow the same shape with some magnitude differences. As seen with the 2-dimensional phantom, the TITAN-IR images appear to have a larger edge effect. Profiles though the cold spheres for reconstruction of the noisy SE-LEHR data are given in Fig. 8.33. The improvement in the profiles due to the smaller collimator acceptance angle is apparent.

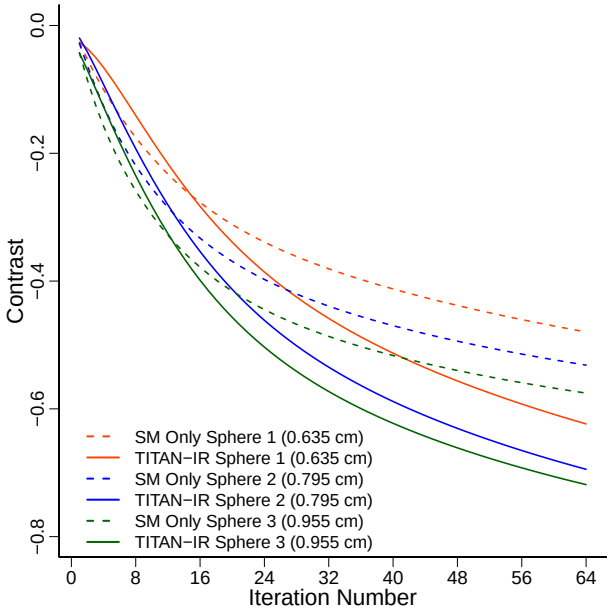

(a) Spheres 1-3

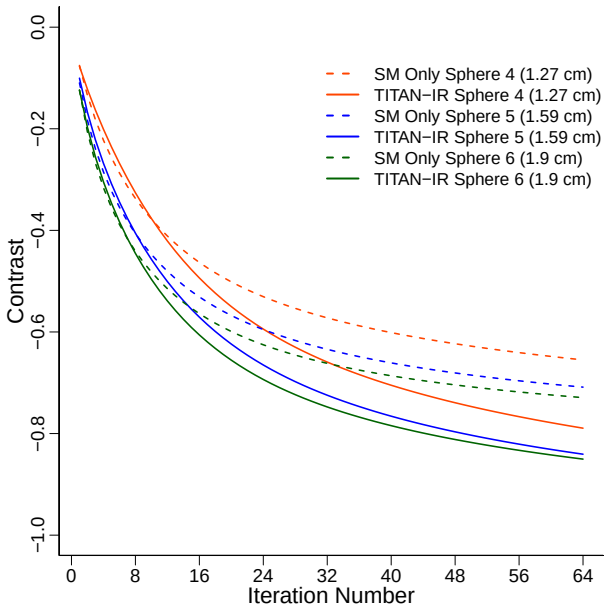

(b) Spheres 4-6

Figure 8.28: Contrast in cold spheres for reconstruction with the system matrix (SM) only and TITAN-IR from noiseless projection data with no collimator blur

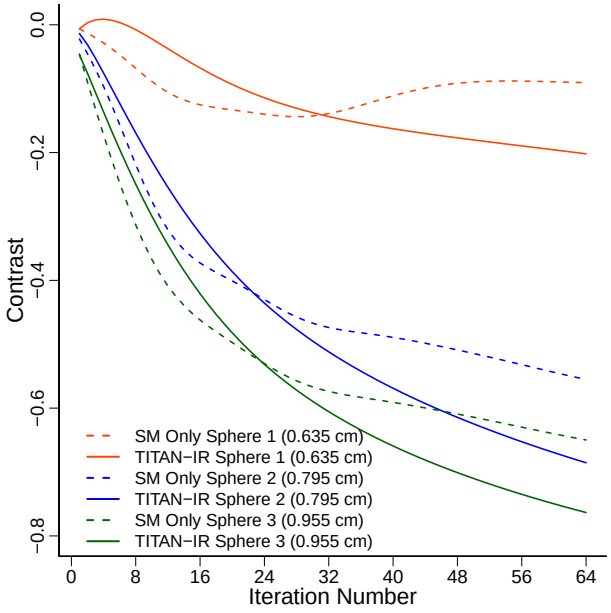

(a) Spheres 1-3

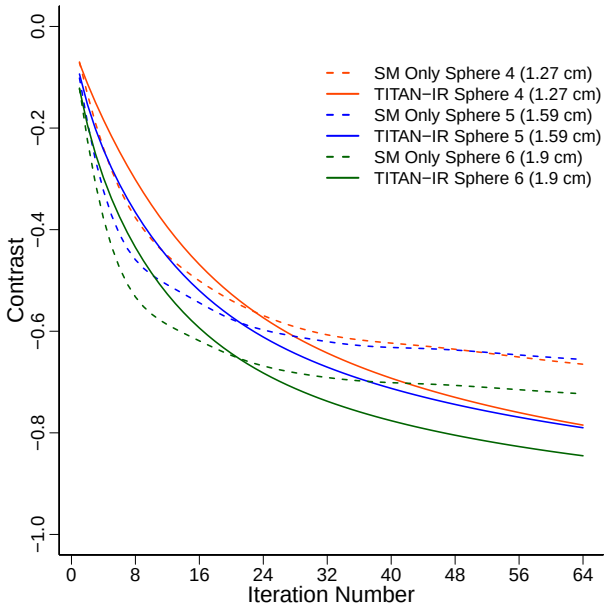

(b) Spheres 4-6

Figure 8.29: Contrast in cold spheres for reconstruction with the system matrix (SM) only and TITAN-IR from noisy projection data with no collimator blur

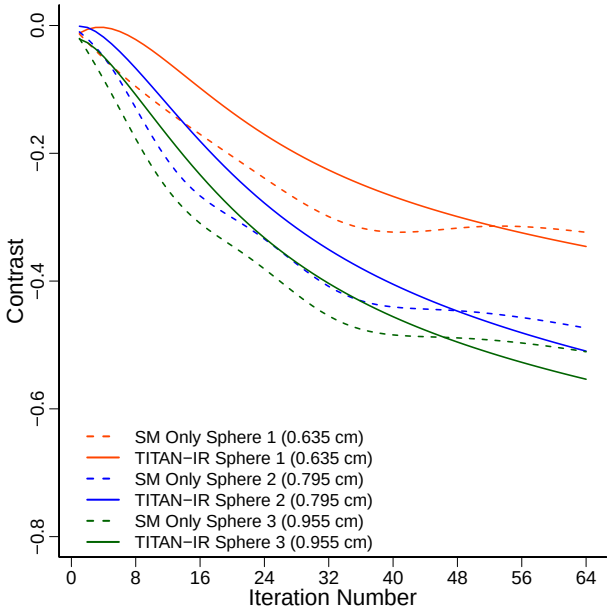

(a) Spheres 1-3

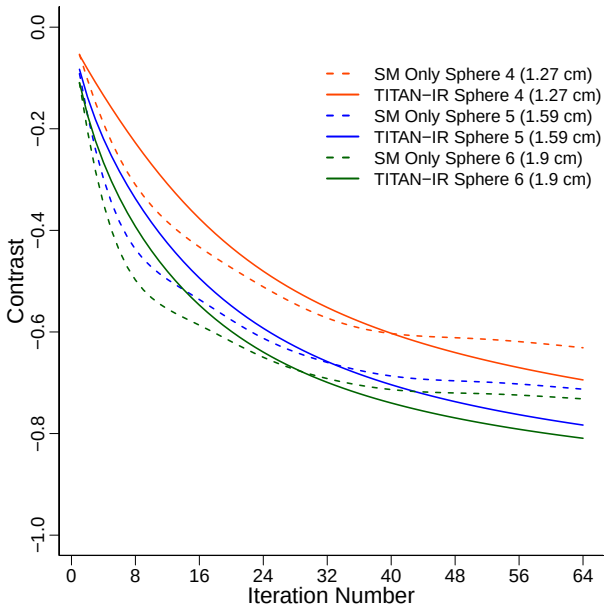

(b) Spheres 4-6

Figure 8.30: Contrast in cold spheres for reconstruction with the system matrix (SM) only and TITAN-IR from noisy GE-LEGP collimator projection data

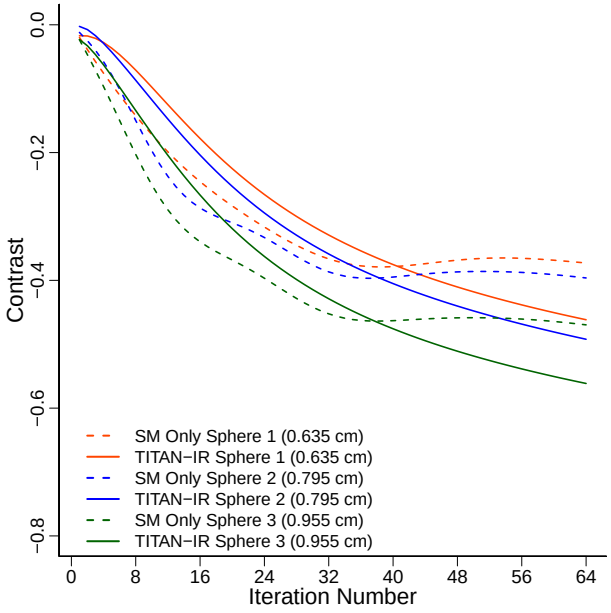

(a) Spheres 1-3

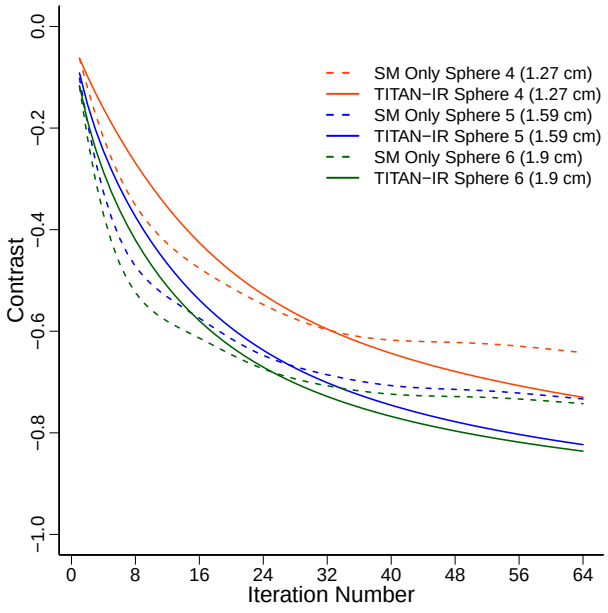

(b) Spheres 4-6

Figure 8.31: Contrast in cold spheres for reconstruction with the system matrix (SM) only and TITAN-IR from noisy SE-LEHR collimator projection data

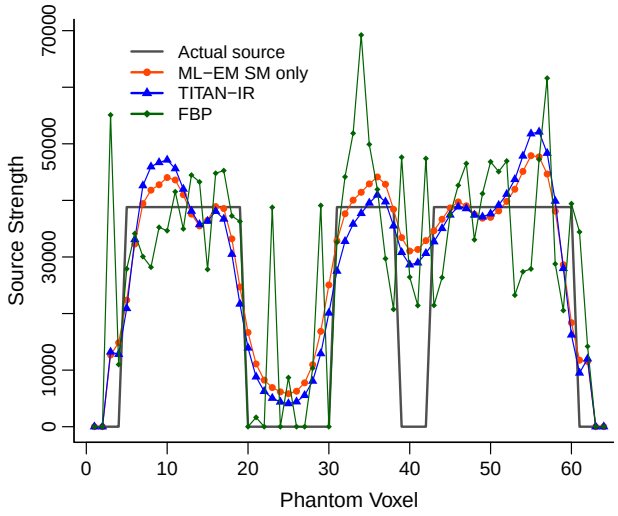

(a) Row 19 through cold spheres 1 and 6

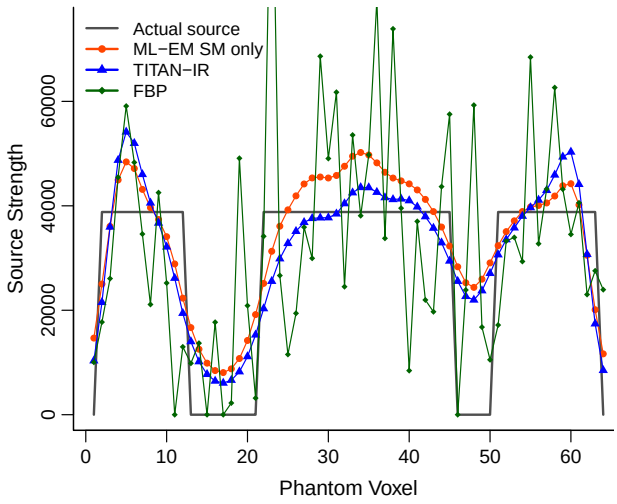

(b) Row 32 through cold spheres 2 and 5

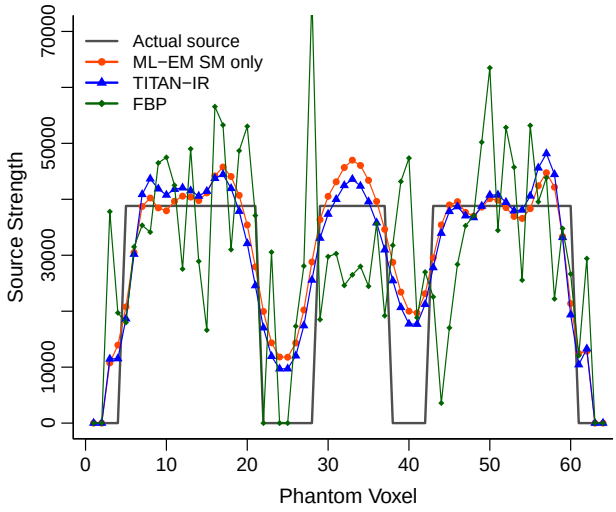

(c) Row 46 through cold spheres 3 and 4

Figure 8.32: Profiles through center slice of reconstruction iteration 40 of noisy GE-LEGP collimator projection data

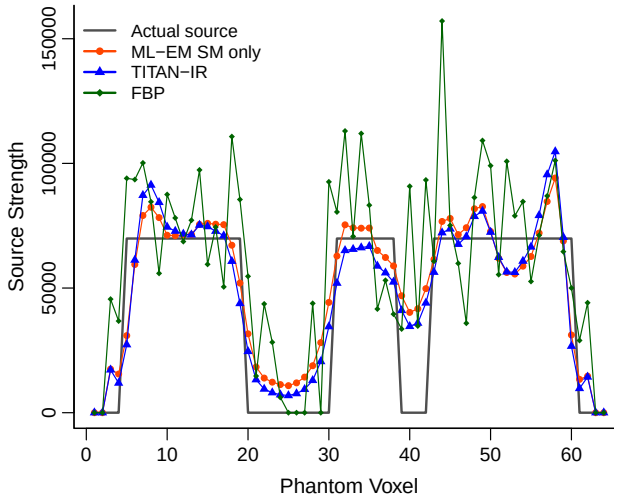

(a) Row 19 through cold spheres 1 and 6

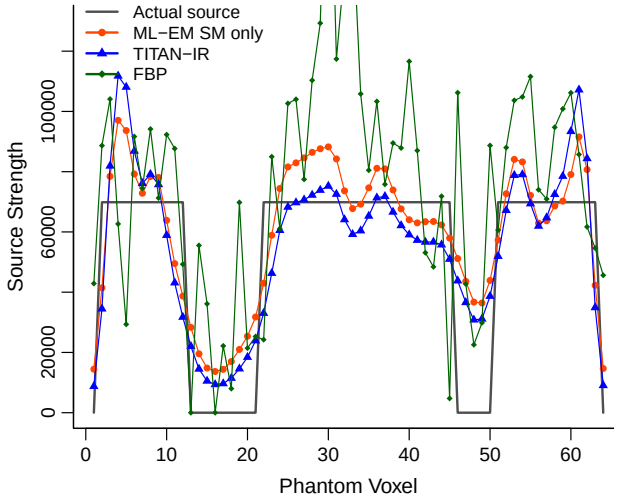

(b) Row 32 through cold spheres 2 and 5

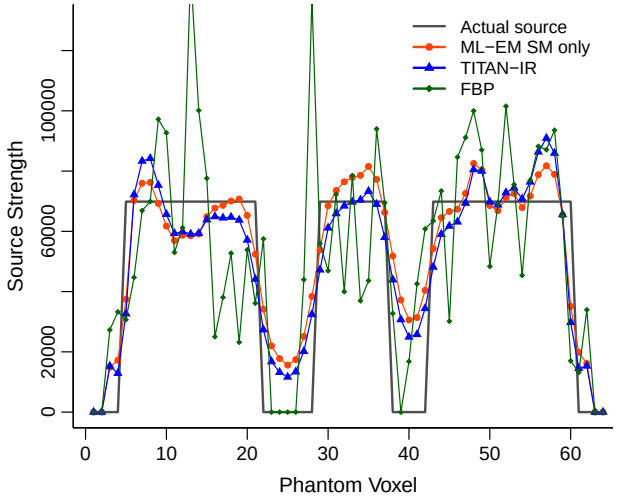

(c) Row 46 through cold spheres 3 and 4

Figure 8.33: Profiles through center slice of reconstruction iteration 40 of noisy SE-LEHR collimator projection data

8.1.5 Computation Time

The computation time for reconstruction with TITAN-IR is an important factor in its performance. The TITAN code was already an efficient parallel transport code and all attempts have been made for TITAN-IR to be fully parallelized. In the following sections, the computation times to reconstruct the Jaszczak phantom and the possibility for improvement through the use of ordered-subsets expectation-maximization (OS-EM) are examined. All calculations are completed on a dedicated computer cluster with Intel Xeon E5 2.6 GHz processors, 16 GB of memory per processor core, and 16 processor cores per compute node. The value of 64 iterations is used so that the number of total iterations can be scaled with increasing subsets for OS-EM.

ML-EM computation time

The time to complete 64 iterations on noiseless projection data with no collimator blur for the coarse, base, and fine meshes is given in Table 8.11. The computation times scale closely with the number of meshes in the model. The computation time for noisy projection data with no collimator blur is the same as the noiseless case. The system matrix for the noisy GE-LEGP collimator projection data is much less sparse, i.e., larger, and so the computation time is $172\ s$ for that case with base meshing. The computation time could be minimized by reducing the system matrix size, i.e., eliminating values below a threshold.

The computation times and parallel speedup for varying numbers of processor cores are given in Table 8.12 for projection data with no collimator blur and in Table 8.13

Table 8.11: Computation time on 16 cores for 64 iterations on noiseless projection data with no collimator blur

Mesh	Time (seconds)
Coarse ($64 \times 64 \times 32$)	36.8
Base ($128 \times 128 \times 64$)	252.1
Fine ($256 \times 256 \times 128$)	2246.7

Table 8.12: Computation time for 64 iterations of noiseless projection data with no collimator blur

Processor Cores	Time (s)	Speedup
1	575.7	-
2	291.5	2.0
4	149.9	3.8
8	81.4	7.1
16	36.8	15.6

Table 8.13: Computation time for 64 iterations on noisy GE-LEGP projection data

Processor Cores	Time (s)	Speedup
1	1665.7	-
2	905.1	1.8
4	524.3	3.2
8	341.4	4.9
16	172.0	9.7

for GE-LEGP collimator projection data. In Table 8.12, the speedup scales well with the number of processor cores. The large system matrix for the noisy GE-LEGP case clearly reduces the speedup achieved.

OS-EM computation time

As discussed in Section 7.2.2, the OS-EM reconstruction algorithm will not result in as significant of speedups in TITAN-IR as it does in standard codes. For this problem, there are 64 projection angles that must be divided evenly into subsets of opposing angles. For example, 4 subsets would each contain 16 projection angles and 16 iterations would

then correspond to 64 iterations with a single subset. Recall that ML-EM is equivalent to OS-EM with 1 subset.

Table 8.14: OS-EM computation time for 64 iterations on noiseless projection data with no collimator blur and noisy GE-LEGP data

Subsets	Angles per subset	Noiseless data Time (s)	Noisy GE-LEGP data Time (s)
1	64	36.8	172.0
2	32	32.4	151.6
4	16	30.6	139.9
8	8	30.9	139.2
16	4	30.9	139.5

The OS-EM computation times for an equivalent of 64 iterations with the noiseless projection data with no collimator blur and the noisy GE-LEGP data are given in Table 8.14. Because TITAN-IR calculates the projections in a subset in parallel, having fewer than 16 angles per subset will leave some processor cores unused. For this situation, 4 subsets is logically the best choice. The noiseless data computation time is reduced by 16% by using 4 subsets and the noisy GE-LEGP data computation time is reduced by 19%. As expected, a large benefit is not seen with OS-EM but a reasonable speedup is observed.

The OS-EM algorithm updates the source distribution more frequently so there are slight differences in the reconstruction images. The MSE and MRE relative to the reference projection data and the background noise in the reconstructed images are given in Table 8.15 for each number of subsets considered. The contrast in the cold spheres

after 64 iterations is given in Table 8.16. Only small changes in these metrics are seen for different numbers of subsets.

Table 8.15: MSE, MRE, and background noise after 64 iterations in TITAN-IR with varying number of subsets

Subsets	MSE	MRE	Background Noise
1	1.27×10^2	8.36%	7.26%
2	1.26×10^2	8.32%	7.25%
4	1.25×10^2	8.30%	7.61%
8	1.23×10^2	8.14%	7.20%
16	1.29×10^2	8.32%	7.80%

Table 8.16: Contrast of cold spheres after 64 iterations in TITAN-IR with varying number of subsets

Subsets	Sphere 1 (0.635 cm)	Sphere 2 (0.795 cm)	Sphere 3 (0.955 cm)	Sphere 4 (1.27 cm)	Sphere 5 (1.59 cm)	Sphere 6 (1.9 cm)
1	-0.346	-0.510	-0.554	-0.694	-0.783	-0.809
2	-0.345	-0.510	-0.553	-0.694	-0.783	-0.809
4	-0.351	-0.512	-0.555	-0.695	-0.785	-0.810
8	-0.362	-0.512	-0.560	-0.698	-0.791	-0.812
16	-0.345	-0.502	-0.556	-0.698	-0.792	-0.811

8.2 NCAT Phantom

The NURBS-based cardiac-torso (NCAT) phantom[61] was used as an anatomical reconstruction case for testing of TITAN-IR. This heterogeneous phantom includes the following materials: air, body tissue (represented as water), intestine, lung, rib bone, liver, kidney, spine bone, muscle, cartilage, spleen, heart, and blood. Axial and lateral views of

the NCAT phantom model used by SIMIND to generate the reference projection data are given in Fig. 8.34. In Fig. 8.34a, the slice is through the center of the heart and shows the rib cage, lungs, and the thick myocardium of the left ventricle. The lateral slice, Fig. 8.34b, is also through the heart and shows the spleen and stomach. To simulated a myocardial perfusion study, a 140.5 keV photon source is located in the heart myocardium (relative strength of 75), body tissue (relative strength of 2), and liver (relative strength of 75). The liver is given a strong source strength because it tends to accumulate Tc-99m. An axial slice through the center of the source distribution used by SIMIND to generate the reference data is given in Fig. 8.35.

(a) Axial view (b) Lateral view

Figure 8.34: Slice through attenuation coefficient distribution of the NCAT phantom in SIMIND model

The NCAT phantom used has overall dimensions of $53.75 \times 28.75 \times 20.0\ cm^3$. The voxel size for the SIMIND model in Fig. 8.34 is $0.10498 \times 0.10498 \times 0.10498\ cm^3$ to be close to the continuous geometry of an actual patient. The voxel size used to generate the

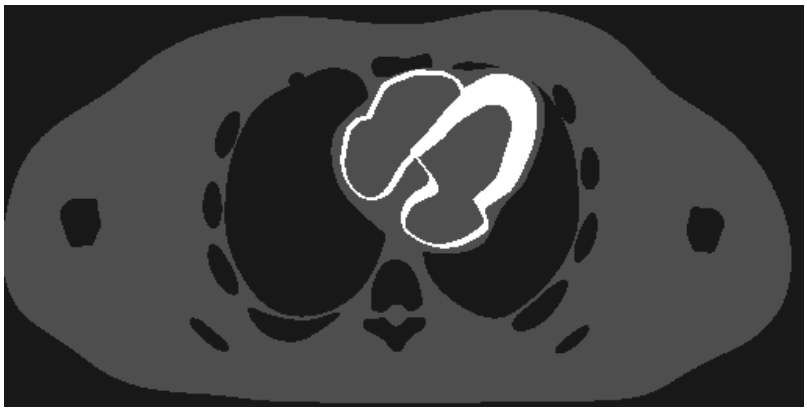

Figure 8.35: Axial slice though source distribution of NCAT phantom in SIMIND model

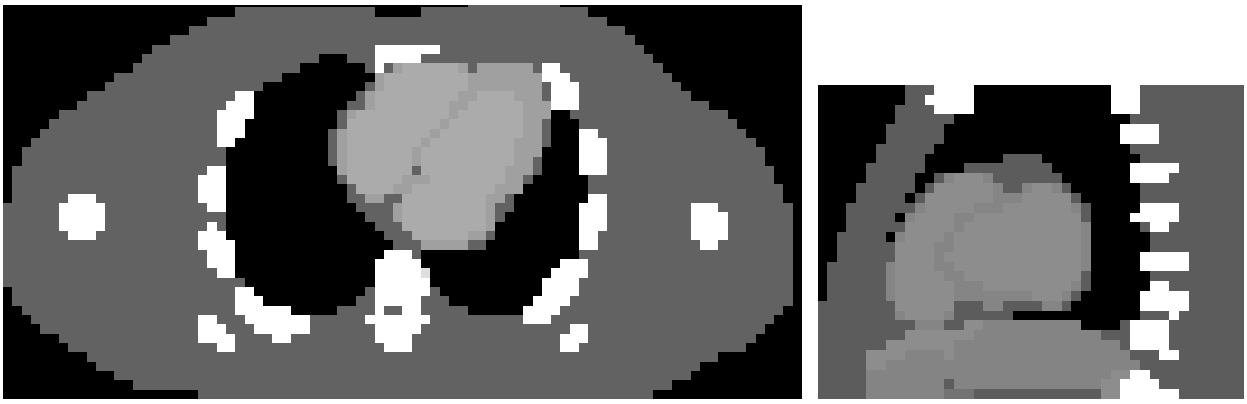

(a) Axial view (b) Lateral view

Figure 8.36: Slice through attenuation coefficient distribution of the NCAT phantom model used for reconstruction

system matrix and by TITAN-IR is $0.625 \times 0.625 \times 0.625\ cm^3$ for $86 \times 46 \times 32$ voxels. Axial and lateral slices through this coarser NCAT phantom model are given in Fig. 8.36.

For the deterministic calculation, cross sections were generated using the CEPXS code[59] with source energy group bounds of 126.45-154.55 keV to account for a typical SPECT energy window of 20%. The transport calculations used a flux tolerance of 10^{-3}, DTW differencing scheme, and anisotropic scatter order of P_1 in the phantom.

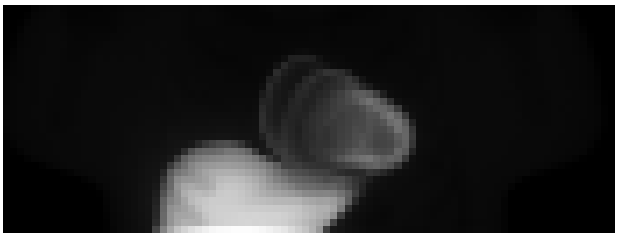

Figure 8.37: Reference frontal projection data

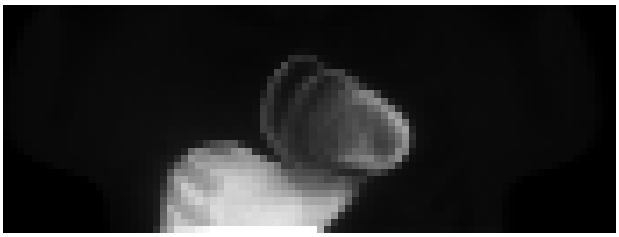

Figure 8.38: TITAN-IR frontal projection data after 40 iterations

A flat source distribution of one is used for the initial guess of all reconstructions and the system matrix is obtained using the Image Reconstruction Toolbox[36] for MATLAB. The NCAT phantom is reconstructed for the cases of noiseless projection data with no collimator blur and noisy collimated projection data. For both cases, the performance of the TITAN-IR code will be evaluated and compared with FBP and ML-EM with SM only reconstruction.

8.2.1 Noiseless Projection Data with No Collimator Blur

Projection data with no noise or collimator blur was reconstructed first. The reference frontal projection data is given in Fig. 8.37 and clearly shows the strong source in the heart wall and liver. The TITAN-IR frontal projection data after 40 iterations is given in Fig. 8.38. The TITAN-IR projection data agrees well visually.

The MSE and MRE in the projections after 40 iterations relative to the reference projection data are given in Table 8.17 for increasing quadrature order and the base meshing. Also given in Table 8.17 is the estimated background noise a region of soft tissue. At iteration 40, the maximum relative difference in the image estimate is -4.02% rela-

Table 8.17: MSE, MRE, and background noise after 40 iterations with the base meshing

S_N	MSE	MRE	Noise
S_6	5.77×10^{-4}	8.88%	13.4%
S_8	5.78×10^{-4}	8.87%	12.2%
S_{16}	5.79×10^{-4}	8.87%	12.4%

Table 8.18: MSE, MRE, and background noise after 40 iterations with the fine meshing

S_N	MSE	MRE	Noise
S_6	4.08×10^{-4}	6.57%	10.1%
S_8	4.09×10^{-4}	6.56%	9.6%
S_{16}	4.09×10^{-4}	6.56%	9.7%

tive to the previous iteration. The number of meshes in the TITAN model was refined to $172 \times 92 \times 64$ voxels to create a fine meshing case. With the fine meshing, the MSE and MRE in the projections after 40 iterations relative to the reference projection data are given in Table 8.18 for increasing quadrature order along with the estimated background noise a region of soft tissue. The maximum relative difference in the image estimate at 40 iterations is 2.65% relative to the previous iteration. The quadrature order, i.e., number of directions in the deterministic model, clearly does not impact the reconstruction significantly, although there is a small reduction in noise. Mesh refinement reduces the MRE by about 2%, but comes at the cost of longer computation time.

Axial and frontal slices through the reconstructed source distribution after 40 iterations with S_8 quadrature and base meshing are given in Fig. 8.39. Fig. 8.39a is through the center of the heart and shows the thick myocardium of the left ventricle. In Fig. 8.39b, the left ventricle is clearly visible as the solid ring of source and the liver is located below the heart.

As a comparison, the NCAT phantom results are reconstructed with FBP in Fig. 8.40 and the SM only in Fig. 8.41. The FBP image has streak artifacts in the axial slice,

(a) Axial slice 16 (b) Frontal slice 18

Figure 8.39: TITAN-IR (S_8, base meshing) reconstructed images from projection data with no noise and no collimator blur after 40 iterations

(a) Axial slice 16 (b) Frontal slice 18

Figure 8.40: FBP reconstructed images from projection data with no noise and no collimator blur

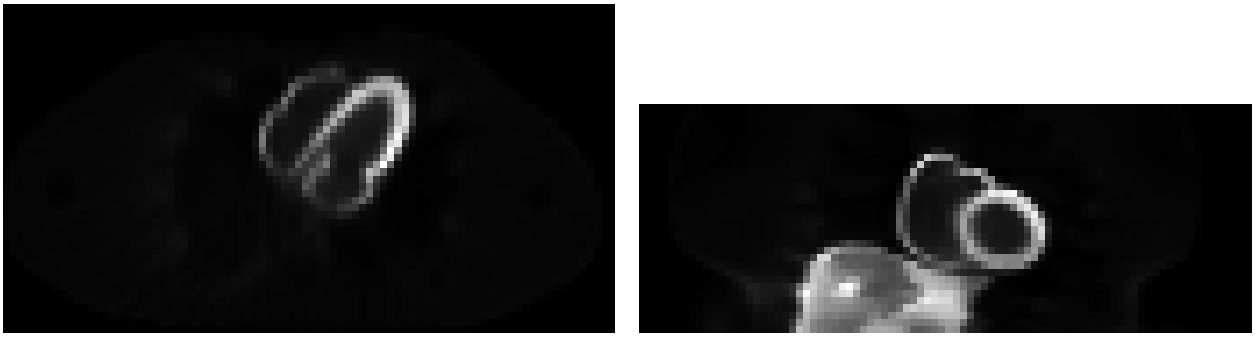

(a) Axial slice 16 (b) Frontal slice 18

Figure 8.41: ML-EM with SM only reconstructed images from projection data with no noise and no collimator blur after 40 iterations

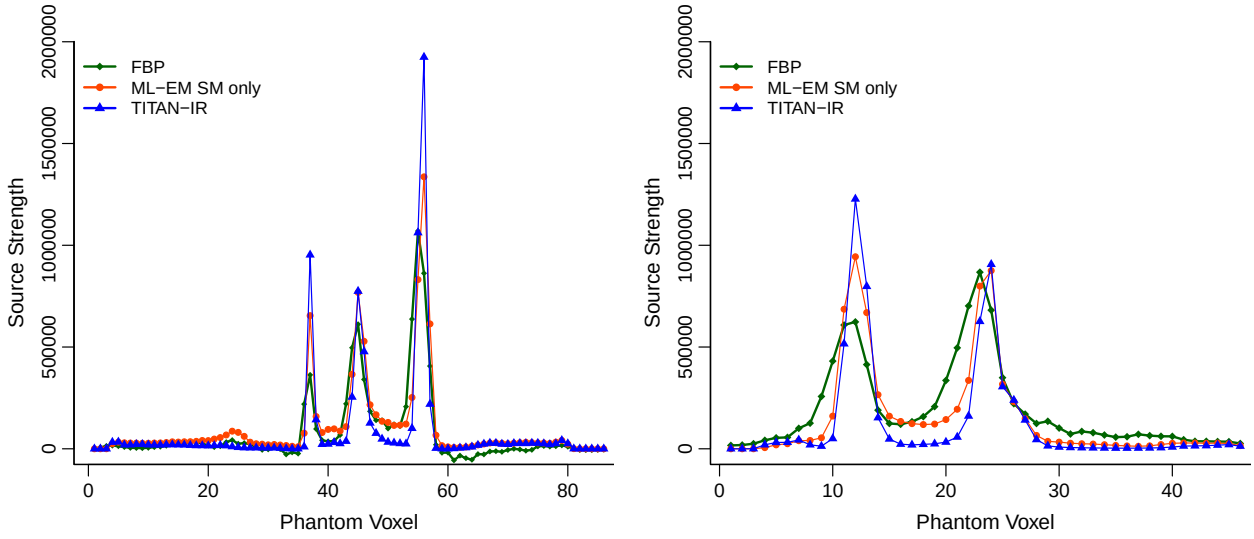

(a) Row 19

(b) Column 53

Figure 8.42: Profiles through heart after reconstruction iteration 40 of noiseless projection data with no collimator blur

but the myocardium is very clear. The SM only image also shows the myocardium well, but suffers from artifacts in the liver. To further compare reconstruction methods, profiles through the axial slice are given in Fig. 8.42. The TITAN-IR profile has the largest differentiation between the myocardium and other tissues. In Fig. 8.42a, the FBP and SM only profiles match well, but in Fig. 8.42b the FBP profile has not resolved the myocardium as well.

8.2.2 Noisy Collimated Projection Data

To examine the reconstruction of the NCAT phantom with noisy collimated data, the GE-LEGP collimator described in Section 8.1.3 was used to create the reference projection data in SIMIND. As explained in Section 8.1.2, Poisson noise was then added to the reference

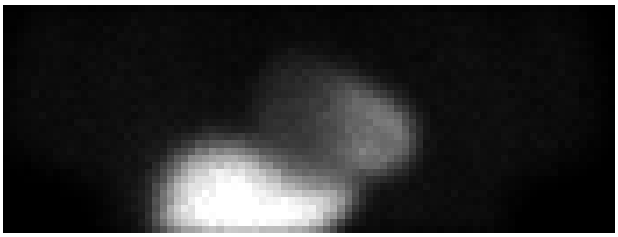

Figure 8.43: Reference frontal projection data

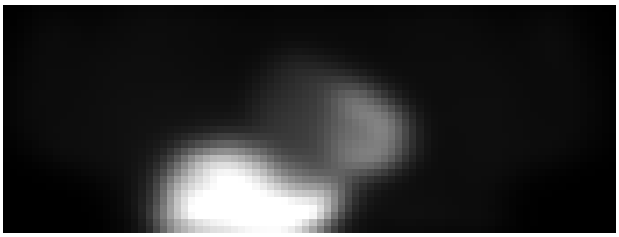

Figure 8.44: TITAN-IR frontal projection data after 40 iterations

data. An average of 3.5×10^5 counts per projection was simulated for an acquisition time of 10.1 s per angle. The reference frontal projection data is given in Fig. 8.43 and clearly shows the strong source in the heart wall and liver. The TITAN-IR frontal projection data after 40 iterations is given in Fig. 8.44 and matches well. The maximum relative difference in the image estimate at iteration 40 is -3.10% relative to the previous iteration.

The MSE and MRE in the projections along with the background noise in the reconstructed image are given in Table 8.19 for increasing quadrature order after 40 iterations. As seen with the noiseless case, the quadrature order does not impact the reconstruction except for a small reduction in noise. Mesh refinement was also considered and found to not improve the reconstruction.

An axial slice through the heart and a frontal slice showing the heart and liver are given in Fig. 8.45 for reconstruction with TITAN-IR after 40 iterations. Compared with

Table 8.19: MSE, MRE, and background noise after 40 iterations

Quadrature	MSE	MRE	Background Noise
S_6	1.63×10^3	8.71%	9.2%
S_8	1.51×10^3	8.48%	6.8%
S_{16}	1.51×10^3	8.48%	7.1%

Fig. 8.39, the image is less sharp and the edge effect noted with previous models is more pronounced in the liver. The projection data was also reconstructed with FBP, Fig. 8.46, and the SM only, Fig. 8.47. The axial FBP image, Fig. 8.46a, shows streaking artifacts and the frontal image, Fig. 8.46b, is blurred. In Fig. 8.47a, the SM only axial image is very similar to the TITAN-IR image, but the frontal image in Fig. 8.47b has large distortions in the liver.

Profiles through the axial slice through the heart are given in Fig. 8.48 for reconstruction by FBP, ML-EM with the SM only, and TITAN-IR. As seen in the images, FBP struggles to resolve the myocardium, while the SM only and TITAN-IR profiles are very similar.

A circular region was defined in the liver of slice 12 to determine the contrast relative to a region of soft tissue. This liver contrast as a function of iteration number is given in Fig. 8.49 for reconstruction with TITAN-IR and ML-EM with the SM only. Initially, both algorithms show similar improvement with iterations, but the contrast with the SM only drops rapidly as the artifacts seen in Fig. 8.47b develop and never fully recovers.

(a) Axial slice 16 (b) Frontal slice 18

Figure 8.45: TITAN-IR (S_8, base meshing) reconstructed images from noisy GE-LEGP projection data after 40 iterations

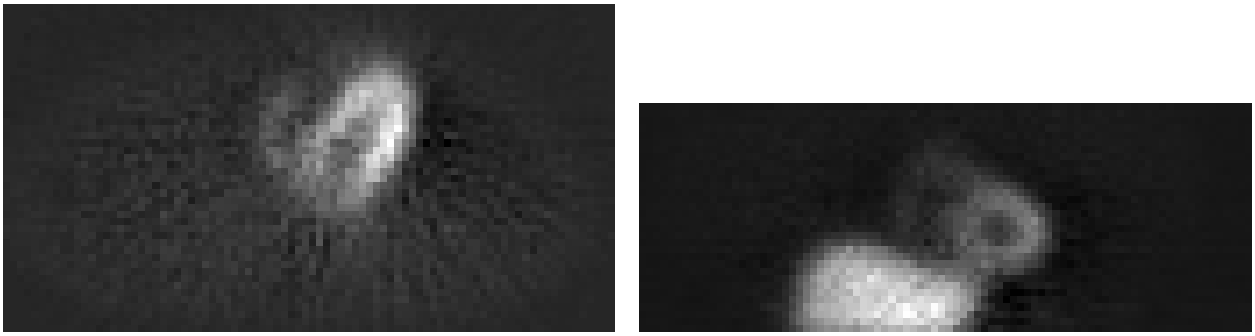

(a) Axial slice 16 (b) Frontal slice 18

Figure 8.46: FBP reconstructed images from noisy GE-LEGP projection data

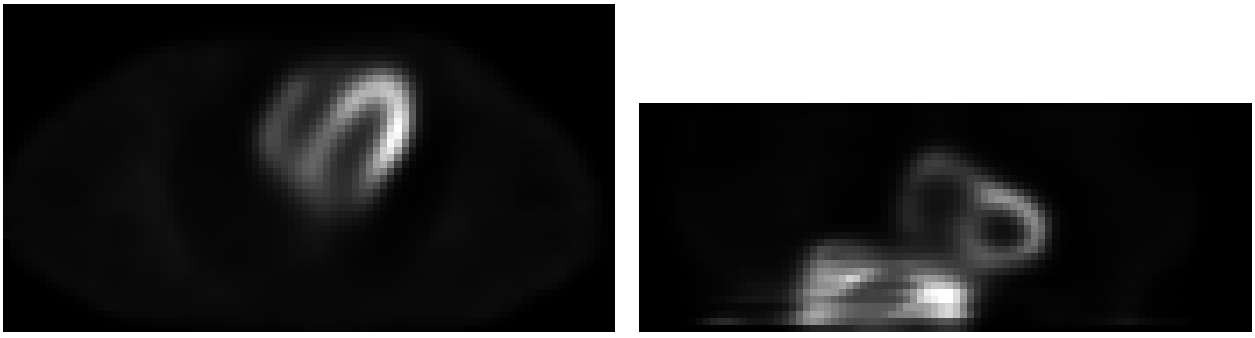

(a) Axial slice 16 (b) Frontal slice 18

Figure 8.47: SM only reconstructed images from noisy GE-LEGP projection data after 40 iterations

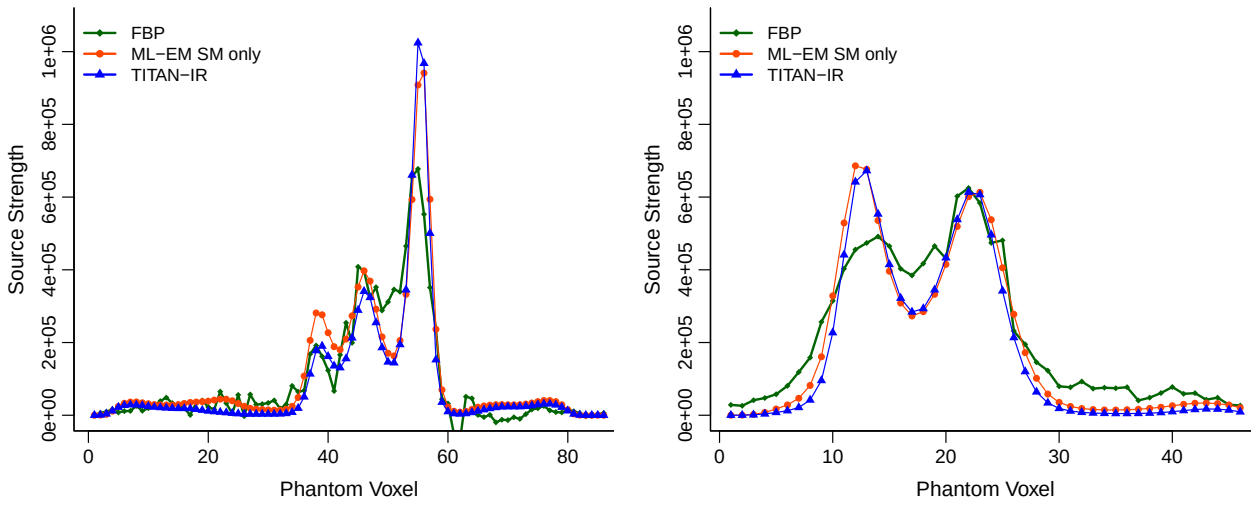

(a) Row 19 (b) Column 53

Figure 8.48: Profiles through heart after reconstruction iteration 40 of noisy GE-LEGP projection data

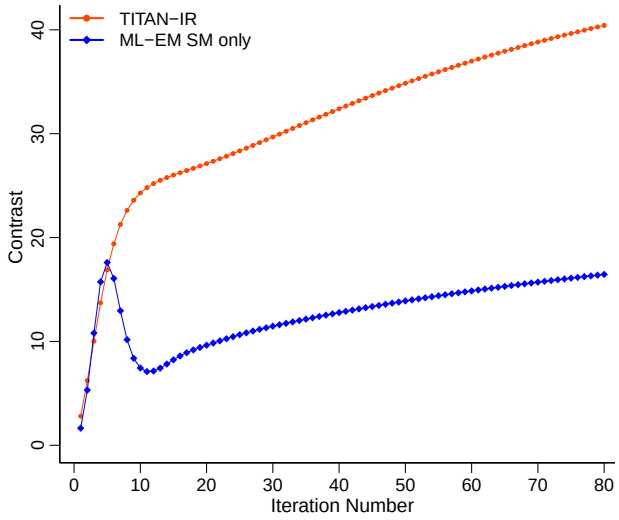

Figure 8.49: Liver contrast in slice 12 as a function of iteration number for reconstruction with TITAN-IR and the SM only

8.2.3 Computation time

All calculations are completed on a dedicated computer cluster running CentOS 5.7 with Intel Xeon E5 2.6 GHz processors, 16 GB of memory per processor core, and 16 processor

cores per compute node. For the following computation times, the deterministic simulation uses S_8 quadrature and base meshing.

The computation time for a standard ML-EM reconstruction of the NCAT phantom by TITAN-IR of noiseless data with no collimator blur on 16 processor cores is 42.0 s for 40 iterations. Of those 42.0 s, 2.8 s are spent loading inputs and initializing the reconstruction. The OS-EM reconstruction times for varying numbers of subsets are given in Table 8.20. Note that the total number of sub-iterations in Table 8.20 remains 40 for all cases, e.g., 10 full iterations with 4 subsets is equivalent to 40 ML-EM iterations. The reduction in computation time with increasing subsets is only 2 to 3 seconds. With the fine meshing deterministic model, the ML-EM computation time becomes 305 s for 40 iterations.

Table 8.20: Computation time for 40 iterations of TITAN-IR (S_8, base meshing) on noiseless projection data with no collimator blur

Subsets	Angles per subset	Time (s)	Speedup
1	64	42.0	-
2	32	39.8	1.06
4	16	39.1	1.07
8	8	38.9	1.08

Table 8.21: Computation time for 40 iterations of TITAN-IR (S_8, base meshing) on noisy GE-LEGP projection data

Subsets	Angles per subset	Time (s)	Speedup
1	64	218.8	-
2	32	204.2	1.07
4	16	194.4	1.13
8	8	195.4	1.12

For reconstruction of GE-LEGP projection data, the sparse system matrix is now over 9 GB instead of the 177 MB required for the projection data with no collimator blur and reading in inputs and initializing the reconstruction takes 143.3 s. Regardless of iterative reconstruction method, reducing the system matrix size can significantly reduce

computation time. The computation time for different numbers of subsets for 40 iterations over-all is given in Table 8.21. The OS-EM algorithm reduces the ML-EM reconstruction time by 24 s or 11%. A larger speedup is seen if the number of iterations is increased.

Chapter 9

Conclusions and Future Work

The TITAN code's ability to generate SPECT projection images has been benchmarked through comparison with results from the SIMIND and MCNP5 Monte Carlo codes as well as an experiment. The TITAN projection images were shown to match well with other methods, in particular for small collimator acceptance angles, and the TITAN code was consistently shown to have the superior computation time. A modified algorithm for representing the collimator called weighted circular ordinate splitting (WCOS) was developed and tested. The parallel behavior of the TITAN SPECT simulation has been studied and improved upon.

The DRS methodology, which reconstructs SPECT projection images using a deterministic transport code, has been developed and tested for ML-EM iterative image reconstruction. The methodology uses a deterministic transport code to fully model the particle transport in a patient during the forward projection step of ML-EM without the

generation of the large system matrix that would be needed to model scatter. DRS was implemented into a script that could be used by anyone with a transport code that creates projection data. The script was tested with a 2-dimensional elliptical water phantom with excellent results; however, computation times are lengthened due to the need to repeatedly read and write files with an external script.

Using the DRS methodology, the TITAN deterministic transport code has been modified for image reconstruction to create the TITAN-IR code. The TITAN-IR code performs ML-EM or OS-EM reconstruction from SPECT projection data in parallel. The user must supply the projection data to reconstruct and a system matrix for backprojection. In addition to iterative image reconstruction, a variety of quality metrics are incorporated into TITAN-IR, including the log-likelihood, relative errors between generated projections and measured data, background noise, and contrast.

TITAN-IR has been used to successfully reconstruct a Jaszczak cold sphere phantom and NCAT phantom from projection data generated using the SIMIND Monte Carlo code. Extensive parameter studies on the Jaszczak phantom examined the dependency of reconstruction quality on deterministic parameters, e.g., quadrature order, mesh size, anisotropic scattering order, and differencing scheme. It was discovered that for these models the reconstruction images are largely insensitive to parameter selection. Deterministic methods tend to be sensitive to parameter selection, so this finding is important to the utility of TITAN-IR.

The ability of TITAN-IR to reconstruct projection data with different degrees of noise and collimator blur was examined in detail with the Jaszczak phantom. The new code demonstrated stable and predictable behavior while handling the addition of these complications. The projection data was also reconstructed using FBP with the Chang attenuation correction and ML-EM with the SM only, i.e., without scatter modeled. With the addition of noise and collimator blur to the Jaszczak phantom projection data, the advantages of TITAN-IR modeling scatter were no longer apparent for this particular case compared with the SM only images. However, the cold sphere contrast had far more stable convergence in TITAN-IR images than the SM only images. The NCAT phantom introduced reconstruction with a heterogeneous phantom and more complicated source distribution. TITAN-IR was able to reconstruct the strong source in both the myocardium and liver, while the SM only images showed severe artifacts in the liver.

Computation time is an important factor in the feasibility of TITAN-IR for application in both a research and a clinical setting. In a deterministic transport code, parameter selection largely drives computation time and so showing a lack of sensitivity of the reconstruction to parameter selection allowed for time to be minimized. The Jaszczak phantom projection data with no collimator blur took 37 s to complete 64 iterations on 16 processor cores with ML-EM. This computation time increased to 172 s for the GE-LEGP projection data, in large part due to the significantly larger system matrix associated with including collimator blur. Using OS-EM with 4 subsets reduced this computation time to 140 s. The same behavior was observed with the NCAT phantom.

The results of this work have indicated that deterministic reconstruction of SPECT data is feasible and opened the door to a wide variety of additional research. Some of these that are particularly interesting to the researcher are the following.

Reconstruction of clinical data

At this point, TITAN-IR has only been used to reconstruct simulated projection data. Collaboration is underway with The Penn State Hershey Cancer Center with the assistance of Michele Ferenci, Chief of Medical Physics, and Karen Brown, Associate Health Physicist, to use TITAN-IR to reconstruct data from a SPECT device. The Hershey Cancer Center is providing projection data acquired from a Jaszczak Phantom with their Siemens Symbia SPECT system as part of their quality assurance program. Reconstruction of data acquired on a clinical SPECT device will be an important step in the validation of TITAN-IR and hopefully be followed by the reconstruction of patient data.

Multi-energy reconstruction

It would be interesting to apply TITAN-IR to cases in which either the radionuclide in the patient emits photons at different energies or multiple radionuclides are present. Down-scatter from higher energy photons to the lower energy photopeak(s) is the primary issue with this type of imaging. Since TITAN already solves the multigroup transport equation, no modification would be needed to the base TITAN code to model multiple photon energies and the down-scatter between them. This is a logical and very promising extension of the capabilities of the TITAN-IR code.

Along the same lines, it may be possible in cases of single-energy emissions to use lower energy groups as part of the reconstruction since TITAN-IR can accurately model the scattering of emitted photons to lower energies. Hutton *et al.* suggested that with accurate modeling of scatter a wider range of energies could be included[43]. Including more counts in the reconstruction could lead to reduced doses and acquisition times, provided those additional counts are modeled properly.

Additional possibilities

The DRS methodology could readily be applied to other iterative reconstruction algorithms besides ML-EM as well as other deterministic codes. In particular, it would improve the utility of TITAN-IR to provide users with a variety of reconstruction algorithms to choose from. Several performance metrics are already calculated in TITAN-IR to facilitate determination of convergence, but this capability should be expanded to improve understanding and give the user more guidance. It would also be interesting to investigate the use of an adjoint methodology with TITAN[75] to calculated the system matrix.

Bibliography

[1] S. R. Cherry, J. A. Sorenson, and M. E. Phelps, *Physics in Nuclear Medicine*, 3rd ed., A. Ross, Ed. Saunders, 2003.

[2] IMV Medical Information Division, Inc., "2011 nuclear medicine market outlook report."

[3] J. T. Bushberg, J. A. Seibert, J. Edwin M. Leidholdt, and J. M. Boone, *The Essential Physics of Medical Imaging*. Lippincott Williams & Wilkins, 2002.

[4] C. Yi, "Hybrid discrete ordinates and characteristics method for solving linear Boltzmann equation," Ph.D. dissertation, University of Florida, 2007.

[5] G. Hevesy, "The absorption and translocation of lead by plants: A contribution to the application of the method of radioactive indicators in the investigation of the change of substance in plants," *Biochem J.*, vol. 17, pp. 439–445, 1923.

[6] E. O. Lawrence and M. S. Livingston, "The production of high speed light ions without the use of high voltages," *Phys. Rev.*, vol. 40, pp. 19–35, April 1932.

[7] H. O. Anger, "Scintillation camera," *Rev. Sci. Instrum.*, vol. 29, no. 1, pp. 27–33, 1958.

[8] P. Harper, R. Beck, D. Charleston, and K. Lathrop, "Optimization of a scanning method using Tc-99m," *Nucleonics*, vol. 22, pp. 50–54, 1964.

[9] W. Tucker, M. Greene, A. Weiss, and A. Murrenhoff, "Methods of preparation of some carrier-free radioisotopes involving sorption on alumina," Brookhaven National Laboratory, BNL 3746, Tech. Rep., 1958.

[10] D. E. Kuhl and R. Q. Edwards, "Cylindrical and section radioisotope scanning of the liver and brain," *Radiology*, vol. 83, pp. 926–936, 1964.

[11] H. O. Anger, "Tomographic gamma-ray scanner with simultaneous read-out of several planes" in *Fundamental Problems of Scanning*. Springfield, IL: Charles C. Thomas, 1968, pp. 195–211.

[12] R. Jaszczak, P. Murphy, D. Huard, and J. Burdine, "Radionuclide emission computed tomography of the head with ^{99m}Tc and a scintillation camera," *J Nucl Med*, vol. 18, no. 4, pp. 373–380, 1977.

[13] J. Keyes, N. Orlandea, W. Heetderks, P. Leonard, and W. Rogers, "The humongotron: a scintillation-camera transaxial tomograph," *J Nucl Med*, vol. 18, pp. 381–387, 1977.

[14] M. Bocher, A. Balan, Y. Krausz, Y. Shrem, A. Lonn, M. Wilk, and R. Chisin, "Gamma camera-mounted anatomical x-ray tomography: technology, system characteristics and first images," *European Journal of Nuclear Medicine*, vol. 27, pp. 619–627, 2000.

[15] M. K. O'Connor and B. J. Kemp, "Single-photon emission computed tomography/computed tomography: Basic instrumentation and innovations," *Seminars in Nuclear Medicine*, vol. 36, no. 4, pp. 258–266, 2006.

[16] M. T. Madsen, "Recent advances in SPECT imaging," *Journal of Nuclear Medicine*, vol. 48, pp. 661–673, 2007.

[17] J. Radon, "Über die bestimmung von funktionen durch ihre integralwerte längs gewisser mannigfaltigkeiten," *Berichte Sächsische Akadamie der Wissenschaften, Leipzig, Math. Phys. Kl.*, vol. 69, pp. 262–277, 1917.

[18] P. P. Bruyant, "Analytic and iterative reconstruction algorithms in SPECT," *Journal of Nuclear Medicine*, vol. 43, pp. 1343–1358, 2002.

[19] A. M. Cormack, "Representation of a function by its line integrals, with some radiological applications," *Journal of Applied Physics*, vol. 34, no. 9, pp. 2722–2727, 1963.

[20] D. E. Kuhl and R. Q. Edwards, "Image separation radioisotope scanning," *Radiology*, vol. 80, pp. 653–662, 1963.

[21] R. Gordon, R. Bender, and G. Herman, "Algebraic reconstruction techniques (ART) for three-dimensional electron microscopy and x-ray photography." *Journal of Theoretical Biology*, vol. 29, no. 3, pp. 471–481, Dec. 1970.

[22] P. Gilbert, "Iterative methods for the three-dimensional reconstruction of an object from projections," *Journal of Theoretical Biology*, vol. 36, no. 1, pp. 105–117, 1972.

[23] L. A. Shepp and Y. Vardi, "Maximum likelihood reconstruction for emission tomography," *IEEE Transactions on Medical Imaging*, vol. 1, no. 2, pp. 113–122, Oct. 1982.

[24] K. Lange and R. Carson, "EM reconstruction algorithms for emission and transmission tomography." *J Comput Assist Tomogr*, vol. 8, pp. 306–316, 1984.

[25] H. Hudson and R. Larkin, "Accelerated image reconstruction using ordered subsets of projection data," *IEEE Transactions on Medical Imaging*, vol. 13, no. 4, pp. 601–609, Dec. 1994.

[26] B. F. Hutton, "Recent advances in iterative reconstruction for clinical SPECT/PET and CT," *Acta Oncologica*, vol. 50, no. 6, pp. 851–858, 2011.

[27] S. Vandenberghe, Y. D'Asseler, R. V. de Walle, T. Kauppinen, M. Koole, L. Bouwens, K. V. Laere, I. Lemahieu, and R. Dierckx, "Iterative reconstruction algorithms in nuclear medicine," *Computerized Medical Imaging and Graphics*, vol. 25, no. 2, pp. 105–111, 2001.

[28] S. Staelens, D. Strul, G. Santin, S. Vandenberghe, M. Koole, Y. D'Asseler, I. Lemahieu, and R. V. de Walle, "Monte carlo simulations of a scintillation camera using GATE: validation and application modelling," *Physics in Medicine and Biology*, vol. 48, no. 18, pp. 3021–42, 2003.

[29] J. C. Yanch, A. B. Dobrzeniecki, C. Ramanathan, and R. Behrman, "Physically realistic monte carlo simulation of source, collimator and tomographic data acquisition for emission computed tomography," *Physics in Medicine and Biology*, vol. 37, no. 4, pp. 853–870, 1992.

[30] R. Harrison, D. Haynor, S. Gillispie, and S. Vannoy, "A public-domain simulation system for emission tomography - photon tracking through heterogeneous attenuation using importance sampling," *The Journal of Nuclear Medicine*, vol. 34, no. 5, May 1993.

[31] M. Ljungberg and S.-E. Strand, "A Monte Carlo program for the simulation of scintillation camera characteristics," *Computer Methods and Programs in Biomedicine*, vol. 29, no. 4, pp. 257–272, 1989.

[32] S. Agostinelli, "Geant4-a simulation toolkit," *Nuclear Instruments and Methods in Physics Research Section A: Accelerators, Spectrometers, Detectors and Associated Equipment*, vol. 506, no. 3, pp. 250–303, 2003.

[33] F. Brown, R. Barrett, T. Booth, J. Bull, L. Cox, R. Forster, T. Goorley, R. Mosteller, S. Post, R. Prael, E. Selcow, A. Sood, and J. Sweezy, "MCNP Version 5," *Trans. Am. Nucl. Soc.*, vol. 87, pp. 273–276, 2002.

[34] T. A. Riauka and Z. W. Gortel, "Photon propagation and detection in single-photon emission computed tomography-an analytical approach," *Med. Phys.*, vol. 21, no. 8, pp. 1311–1321, August 1994.

[35] R. Wells, A. Celler, and R. Harrop, "Analytical calculation of photon distributions in SPECT projections," *IEEE Transactions on Nuclear Science*, vol. 45, no. 6, pp. 3202–3214, 1998.

[36] J. Fessler, "Iterative methods for image reconstruction," 2008. [Online]. Available: http://www.eecs.umich.edu/~fessler/papers/files/talk/08/isbi-notes.pdf

[37] G. K. Loudos, P. Papadimitroulas, P. Zotos, I. Tsougos, and P. Georgoulias, "Development and evaluation of QSPECT open-source software for the iterative reconstruction of SPECT images." *Nuclear Medicine Communications*, vol. 31, no. 6, pp. 558–566, 2010.

[38] K. Thielemans, C. Tsoumpas, S. Mustafovic, T. Beisel, P. Aguiar, N. Dikaios, , and M. W. Jacobson, "STIR: Software for tomographic image reconstruction release 2," *Physics in Medicine and Biology*, vol. 57, no. 4, pp. 867–883, 2012.

[39] B. M. Fuster, C. Falcon, C. Tsoumpas, L. Livieratos, P. Aguiar, A. Cot, D. Ros, and K. Thielemans, "Integration of advanced 3D SPECT modeling into the open-source STIR framework," *Medical Physics*, vol. 40, no. 9, 2013.

[40] S. Pedemonte, A. Bousse, K. Erlandsson, M. Modat, S. Arridge, B. F. Hutton, and S. Ourselin, "GPU accelerated rotation-based emission tomography reconstruction," in *Proc. IEEE MIC 2010*, Knoxville, TN, Oct. 30-Nov. 6 2010.

[41] A. Hara, R. Paden, A. Silva, J. Kujak, H. Lawder, and W. Pavlicek, "Iterative reconstruction technique for reducing body radiation dose at CT: Feasibility study," *American Journal of Roentgenology*, vol. 193, no. 3, pp. 764–771, 2009.

[42] P. Green, "Bayesian reconstructions from emission tomography data using a modified EM algorithm," *IEEE Transactions on Medical Imaging*, vol. 9, no. 1, pp. 84–93, 1990.

[43] B. F. Hutton, I. Buvat, and F. J. Beekman, "Review and current status of SPECT scatter corrections," *Physics in Medicine and Biology*, vol. 56, no. 14, 2011.

[44] C. Kamphuis, F. J. Beekman, P. P. van Rijk, and M. A. Viergever, "Dual matrix ordered subsets reconstruction for accelerated 3D scatter compensation in single-photon emission tomography," *European Journal of Nuclear Medicine and Molecular Imaging*, vol. 25, pp. 8–18, 1998.

[45] E. Frey, K. Gilland, and B. Tsui, "Application of task-based measures of image quality to optimization and evaluation of three-dimensional reconstruction-based compensation methods in myocardial perfusion SPECT," *IEEE Transactions on Medical Imaging*, vol. 21, no. 9, pp. 1040–1050, 2002.

[46] J. Xiao, F. Verzijlbergen, M. Viergever, and F. Beekman, "Small field-of-view dedicated cardiac SPECT systems: impact of projection truncation," *European Journal of Nuclear Medicine and Molecular Imaging*, vol. 37, pp. 528–536, 2010.

[47] E. C. Frey and B. Tsui, "A new method for modeling the spatially-variant, object-dependent scatter response function in SPECT," in *Nuclear Science Symposium, 1996 Conference Record*, vol. 2, 1996, pp. 1082–1086.

[48] F. Beekman, H. de Jong, and S. van Geloven, "Efficient fully 3-D iterative SPECT reconstruction with monte carlo-based scatter compensation," *IEEE Transactions on Medical Imaging*, vol. 21, no. 8, pp. 867–877, 2002.

[49] F. J. Beekman, H. W. de Jong, and E. T. Slijpen, "Efficient SPECT scatter calculation in non-uniform media using correlated monte carlo simulation," *Physics in Medicine and Biology*, vol. 44, no. 8, pp. N183–92, 1999.

[50] G. Zeng and G. Gullberg, "Unmatched projector/backprojector pairs in an iterative reconstruction algorithm," *IEEE Transactions on Medical Imaging*, vol. 19, no. 5, pp. 548–555, May 2000.

[51] J. J. Duderstadt and L. J. Hamilton, *Nuclear Reactor Analysis*. John Wiley and Sons, 1976.

[52] E. E. Lewis and W. F. Miller, *Computational Methods of Neutron Transport*. John Wiley and Sons, 1984.

[53] B. G. Petrovic and A. Haghighat, "Analysis of inherent oscillations in multidimensional solutions of the neutron transport equation," *Nuclear Science and Engineering*, vol. 124, pp. 31–62, 1996.

[54] C. Yi and A. Haghighat, "A three-dimensional block-oriented hybrid discrete ordinates and characteristics method," *Nuclear Science and Engineering*, vol. 164, no. 3, pp. 221–247, 2010.

[55] G. I. Bell and S. Glasstone, *Nuclear Reactor Theory*. Malabar, FL: Robert E. Kreiger Publishing, 1985.

[56] B. Petrovic and A. Haghighat, "New directional theta-weighted Sn differencing scheme and its application to pressure vessel fluence calculations," *Proc. Radiation Protection and Shielding Topical Meeting*, vol. I, pp. 3–10, 1996.

[57] C. Yi and A. Haghighat, "Hybrid SN and ray-tracing with fictitious quadrature for simulation of SPECT," in *Proc. M&C 2009*. Saratoga Springs, New York: American Nuclear Society, May 3-7 2009, [CD-ROM].

[58] G. Longoni and A. Haghighat, "Development of the regional angular refinement and its application to the CT-scan device," *Transactions of the American Nuclear Society*, vol. 86, pp. 246–248, 2002.

[59] L. J. Lorence, J. E. Morel, and G. D. Valdez, *User's Guide to CEPXS/ONELD: A One-Dimensional Coupled Electron-Photon Discrete Ordinates Code Package Version 1.0*, Sandia National Laboratory, SAND89-1161, 1989.

[60] K. Royston, A. Haghighat, C. Yi, A. Cebula, and D. Gilland, "Validation of a new deterministic transport code for SPECT simulation," in *Proc. IEEE MIC 2010*, Knoxville, TN, Oct. 30-Nov. 6 2010, [CD-ROM].

[61] W. P. Segars, "Development and application of the new dynamic NURBS-based cardiac-torso (NCAT) phantom," Ph.D. dissertation, University of North Carolina, 2001.

[62] K. Royston, A. Haghighat, and C. Yi, "Comparison of TITAN hybrid deterministic transport code and MCNP5 for simulation of SPECT," *Progress in Nuclear Science and Technology*, vol. 2, pp. 201–206, 2011.

[63] M. Studenski, D. Gilland, J. Parker, B. Hammond, S. Majewski, A. Weisenberger, and V. Popov, "Performance evaluation of a bedside cardiac SPECT system," *IEEE Transactions on Nuclear Science*, vol. 56, no. 3, pp. 625–632, 2009.

[64] K. K. Royston and A. Haghighat, "Sensitivity analysis of the TITAN hybrid deterministic transport code for SPECT simulation," in *Proc. M&C 2011*. Rio de Janeiro, RJ, Brazil: Latin American Section/American Nuclear Society, May 8-12 2011, [CD-ROM].

[65] G. M. Amdahl, "Validity of the single processor approach to achieving large scale computing capabilities," in *Proceedings of AFIPS, April 18-20, 1967*, vol. 30, New York, NY, USA, 1967, pp. 483–485.

[66] K. Royston, A. Haghighat, and C. Yi, "Application of TITAN for simulation of particle streaming in a duct," in *Proc. 15th ISRD*, Aix en Provence, France, May 18-23 2014.

[67] K. Royston and A. Haghighat, "Development of a collimator representation in the TITAN transport code for SPECT simulation," in *Proc. IEEE MIC 2012*, Anaheim, CA, Oct. 29-Nov. 3 2012, [CD-ROM].

[68] K. Royston and A. Haghighat, "Performance of the new WCOS technique for the TITAN SPECT formulation," in *Proc. SNA+MC 2013*, Paris, France, Oct. 27-31 2013.

[69] B. Petrovic and A. Haghighat, "New directional theta-weighted (DTW) differencing scheme and reduction of estimated pressure vessel fluence uncertainty," Prague, Czech Republic, September 2-6 1996.

[70] D. L. Snyder, M. I. Miller, L. J. Thomas, and D. G. Politte, "Noise and edge artifacts in mazimum-likelihood reconstructions for emission tomography," *IEEE Transactions on Medical Imaging*, vol. MI-6, no. 3, pp. 228–238, 1987.

[71] M. Frigo and S. G. Johnson, "The design and implementation of FFTW3," *Proc. of IEEE*, vol. 93, no. 2, pp. 216–231, 2005.

[72] L. S. Graham, F. H. Fahey, M. T. Madsen, A. van Aswegen, and M. V. Yester, "Quantitation of SPECT performance: report of task group 4, nuclear medicine committee," *Medical Physics*, vol. 22, no. 4, pp. 401–409, 1995.

[73] C. E. Metz, F. B. Atkins, and R. N. Beck, "The geometric transfer function component for scintillation camera collimators with straight parallel holes," *Physics in Medicine and Biology*, vol. 25, no. 6, 1980.

[74] L.-T. Chang, "A method for attenuation correction in radionuclide computed tomography," *IEEE Transactions on Nuclear Science*, vol. 25, no. 1, pp. 638–643, 1978.

[75] K. Royston, A. Haghighat, and C. Yi, "Verification of a hybrid adjoint methodology in TITAN for single photon emission computed tomography," in *Proc. PHYSOR 2010*, Pittsburgh, PA, May 9-14 2010, [CD-ROM].

Appendices

Appendix A

Reconstruction Script

The reconstruction script for calling TITAN in parallel follows.

```
#!/bin/bash

# Get the path
abspath=$(cd ${0%/*} && echo $PWD/${0##*/})
path_only=`dirname "$abspath"`
date1=$(date +"%s")
test=0
n_iter=20
filebase="titan.o"

# Initialize
cp ones_2d_base.bin x.bin
conFile="contrast.txt"
mseFile="mse.txt"
echo "      Contrast       Il          nIl       Io          nIo" >> $conFile
echo "MSE calculation for each iteration" > $mseFile

if [ $test -eq 0 ]
then
  # Add initial src dist guess to TITAN input file
  sed -e '/srcdis=1/r ones_2d_base.txt' 2circ_base.tmp > 2circ.tan
  # ML-EM iterations
  for (( i_iter=1; i_iter<=$n_iter; i_iter++ ))
  do
    echo "Iteration $i_iter"
```

```
    # Run TITAN
    jobid=`qsub titan_1_16.sh`
    echo $jobid
    jobnum=$(echo "$jobid" | grep -Po '^[^.]*')
    fileName=$filebase$jobnum
    echo $fileName
    # Wait for TITAN to finish
    while [ ! -f $fileName ]
    do
      echo "Sleeping"
      sleep 10s
    done
    # ML-EM algorithm with TITAN forward projections
    ./mlem.exe < shepp.inp
    # Update TITAN input file with latest src distribution estimate
    sed -e '/srcdis=1/r x.txt' 2circ_base.tmp > 2circ.tan

    echo "x_$i_iter.bin"
    cp x.bin "x_$i_iter.bin"
    cp sino.bin "sino_$i_iter.bin"
  done
else
  # ML-EM algorithm testing
  ./mlem.exe < shepp.inp
fi

date2=$(date +"%s")
diff=$(($date2-date1))
echo "$(($diff / 60)) minutes and $(($diff % 60)) seconds elapsed."
```

The script sets the initial guess of the source distribution (`x.bin`) and checks if this is a test. The test option reconstructs the source with only the system matrix to verify that the `mlem.exe` code is working properly. If the test option is false, the script procedure described in Section 6.2.1 is followed. The initial source distribution is added to the TITAN input file and the reconstruction loop is started. For each iteration a parallel TITAN simulation is completed, the ML-EM code is called, and the new source distribution is added to the TITAN input file. The `mlem.exe` code follows.

```
MODULE inpData
```

```
  IMPLICIT NONE
  INTEGER :: bx, by, bz         ! Phantom dimensions
  INTEGER :: dx, dy, da         ! Detector x & y dimensions, number of angles
  INTEGER :: n_iter             ! Max number of iterations
  REAL, ALLOCATABLE :: pbd(:,:) ! Prob emission in box b is detected in detector unit d
  REAL, ALLOCATABLE :: proj(:)  ! Actual projection data
  REAL, ALLOCATABLE :: sca(:)   ! Scaling information
  CHARACTER(50) :: projFile
  CHARACTER(50) :: sysFile
  CHARACTER(50) :: titanFile
  LOGICAL :: test
  REAL, DIMENSION(3) :: ol, oo ! Contrast origins
  REAL :: rad                       ! Contrast radius
  INTEGER :: tx, ty, tz
END MODULE

MODULE mlemData
  IMPLICIT NONE
  REAL, ALLOCATABLE :: xi(:)  ! Initial guess
  REAL, ALLOCATABLE :: x(:)   ! Current estimate of solution
  REAL, ALLOCATABLE :: sj(:)  ! Sum of system matrix over detector bins
  REAL, ALLOCATABLE :: den(:) ! TITAN projection data
END MODULE

MODULE outData
  IMPLICIT NONE
  CHARACTER(50) :: logFile='mlem.log'
  INTEGER :: logID=10
  CHARACTER(50) :: contrastFile='contrast.txt'
  INTEGER :: conID=11
  CHARACTER(50) :: likeFile='likelihood.txt'
  INTEGER :: likID=12
  CHARACTER(50) :: mseFile='mse.txt'
  INTEGER :: mseID=13
END MODULE

PROGRAM shepp
  use inpData
  use outData
  IMPLICIT NONE

  REAL, ALLOCATABLE :: mu(:)    ! TITAN forward projection
  REAL, ALLOCATABLE :: lam(:)   ! Estimated emissions in box b
  REAL :: maxDet
  INTEGER :: det                ! Detector dimensions (da=angles)
  INTEGER :: box                ! Phantom dimensions
  INTEGER :: id, b, d, k, maxIter, IOS

  OPEN(logID,file=trim(logFile))
  call readInp()
  maxIter=1
```

```
det=dx*dy*da
box=bx*by*bz
ALLOCATE(pbd(box,det),mu(det),lam(box),proj(det),sca(da))

write(logID,*) 'mlem version 4'

OPEN(1,file=projFile,FORM='binary',IOSTAT=IOS)
WRITE(logID,*) 'Status of reading in measured data:', IOS
READ(1) proj
CLOSE(1)
! Scaling information based on measured data
do id=1,da
  sca(id)=sum(proj(((id-1)*dx*dy)+1:id*dx*dy))
end do
write(*,*) 'scale:', sca
OPEN(1,file=sysFile,FORM='binary',IOSTAT=IOS)
WRITE(logID,*) 'Status of reading in system matrix:', IOS
READ(1) pbd
CLOSE(1)

write(logID,*) 'Is this a test run? ', test
if (test) then
  call mlem_test()
else
  call mlem()
end if

DEALLOCATE(pbd,mu,lam,proj)
CLOSE(logID)

END PROGRAM shepp

subroutine readInp
  use inpData
  use outData
  IMPLICIT NONE

  read(*,*)
  read(*,*)
  read(*,*) bx, by, bz
  write(logID,*) 'bx, by, bz', bx, by, bz
  read(*,*)
  read(*,*) dx, dy, da
  write(logID,*) 'dx, dy, da', dx, dy, da
  read(*,*)
  read(*,*) projFile
  write(logID,*) 'projFile:', trim(projFile)
  read(*,*)
  read(*,*) sysFile
  write(logID,*) 'sysFile:', trim(sysFile)
  read(*,*)
```

```
    read(*,*) n_iter
    read(*,*)
    read(*,*) titanFile
    write(logID,*) 'titanFile:', trim(titanFile)
    read(*,*)
    read(*,*) test
    read(*,*)
    read(*,*) ol(1), ol(2), ol(3), oo(1), oo(2), oo(3), rad
    write(logID,*) 'Contrast parameters:', ol(:), oo(:), rad
    read(*,*)
    read(*,*) tx, ty, tz

  end subroutine readInp

  subroutine mlem
    use inpData
    use mlemData
    use outData
    IMPLICIT NONE

    logical :: isnanf, isinff
    INTEGER :: ib, id, ia, idx, idy
    INTEGER :: box, det
    INTEGER :: i_iter, IOS
    REAL :: dsum, maxTmp

    box=bx*by*bz
    det=dx*dy*da
    allocate(xi(box),x(box),sj(box))
    allocate(den(det))

    OPEN(1,file='x.bin',form='binary',IOSTAT=IOS)
    READ(1) xi
    CLOSE(1)
    den(:)=0.0
    sj(:)=0.0
    do ib=1,box
      sj(ib)=sum(pbd(ib,:))
    end do

    i_iter=0
      i_iter=i_iter+1
    OPEN(2,file=trim(titanFile),form='binary',iostat=IOS)
    WRITE(logID,*) 'Read TITAN sinogram status:', IOS
    do ia=1,da
      do id=1,dx*dy
        READ(2) den(det-(ia*dx*dy)+id)
      end do
    end do
    CLOSE(2)
! Scale TITAN sinogram to match projection data
```

```
  do ia=1,da
    maxTmp=sum(den(((ia-1)*dx*dy)+1:ia*dx*dy))
    den(((ia-1)*dx*dy)+1:ia*dx*dy)=sca(ia)*den(((ia-1)*dx*dy)+1:ia*dx*dy)/maxTmp
  end do

  OPEN(2,file='sino.bin',form='binary',iostat=IOS)
  WRITE(2) den
  CLOSE(2)
    do ib=1,box
      dsum=0.0
      do id=1,det
        if(den(id).GT.0.0) then
          dsum=dsum+(pbd(ib,id)*proj(id)/den(id))
        end if
      end do
      if(sj(ib).GT.0.0d0) then
        x(ib)=xi(ib)*dsum/sj(ib)
      else
        x(ib)=0.0d0
      end if
      if(isnanf(x(ib))) then
        write(logID,*) 'isnan at x(', ib, ')'
        stop
      elseif(isinff(x(ib))) then
        write(logID,*) 'isinf at x(', ib, ')'
        stop
      end if
    end do
    xi(:)=x(:)

  OPEN(1,file='x.bin',FORM='binary',IOSTAT=IOS)
  WRITE(logID,*) 'Status of x data:', IOS
  WRITE(1) x
  CLOSE(1)

  ! write output for TITAN
  call writeTITAN()

  call contrast()
  call calcMSE()
end subroutine mlem

subroutine mlem_test
  use inpData
  use mlemData
  use outData
  IMPLICIT NONE

  INTEGER :: ib, id, ia
  INTEGER :: box, det
  INTEGER :: i_iter, IOS
```

```
  REAL :: dsum

  box=bx*by*bz
  det=dx*dy*da
  allocate(xi(box),x(box),sj(box))
  allocate(den(det))
  xi(:)=1.0
  den(:)=0.0
  sj(:)=0.0
  do ib=1,box
    sj(ib)=sum(pbd(ib,:))
  end do
  i_iter=0
  do while (i_iter.lt.n_iter)
    i_iter=i_iter+1
    write(logID,*) 'Iteration:', i_iter
    do id=1,det
      do ib=1,box
        den(id)=den(id)+(pbd(ib,id)*xi(ib))
      end do
    end do
    do ib=1,box
      dsum=0.0
      do id=1,det
        dsum=dsum+(pbd(ib,id)*proj(id)/den(id))
      end do
      x(ib)=xi(ib)*dsum/sj(ib)
    end do
    xi(:)=x(:)
  end do ! while loop

  OPEN(1,file='x.bin',FORM='binary',IOSTAT=IOS)
  WRITE(logID,*) 'Status of x data:', IOS
  WRITE(1) x
  CLOSE(1)

end subroutine mlem_test

  subroutine contrast
  use mlemData
  use inpData
  use outData
  IMPLICIT NONE

  REAL(4) :: xpos(bx), ypos(by), zpos(bz)
  REAL(4) :: cl, Il, Io, distl, disto
  INTEGER :: ix, iy, iz, nIl, nIo, IOS

  do iz=1,bz
    zpos(iz)=iz-0.5d0
  end do
```

```
  do iy=1,by
    ypos(iy)=iy-0.5d0
  end do
  do ix=1,bx
    xpos(ix)=ix-0.5d0
  end do

  Il=0.0d0
  Io=0.0d0
  nIl=0
  nIo=0
  do iz=1,bz
    do iy=1,by
      do ix=1,bx
        distl=sqrt(((xpos(ix)-ol(1))*(xpos(ix)-ol(1)))+ &
                   ((ypos(iy)-ol(2))*(ypos(iy)-ol(2)))+ &
                   ((zpos(iz)-ol(3))*(zpos(iz)-ol(3))))
        disto=sqrt(((xpos(ix)-oo(1))*(xpos(ix)-oo(1)))+ &
                   ((ypos(iy)-oo(2))*(ypos(iy)-oo(2)))+ &
                   ((zpos(iz)-oo(3))*(zpos(iz)-oo(3))))
        if(distl.LE.rad) then
          Il=Il+x(ix+((iy-1)*bx)+((iz-1)*bx*by))
          nIl=nIl+1
        else if(disto.LE.rad) then
          Io=Io+x(ix+((iy-1)*bx)+((iz-1)*bx*by))
          nIo=nIo+1
        end if
      end do
    end do
  end do

  cl=(Il-Io)/Io
  OPEN(conID,file=trim(contrastFile),position='append')
  write(conID,*) cl, Il, nIl, Io, nIo
  CLOSE(conID)

end subroutine contrast

subroutine calcMSE
  use mlemData
  use outData
  use inpData
  IMPLICIT NONE

  CHARACTER(50) :: xtrueFile='xtrue_2d.bin'
  REAL, ALLOCATABLE :: xtrue(:), xscale(:)
  REAL :: mseX, mseP, xcnt
  INTEGER :: IOS, ib, id, box, det

  box=bx*by*bz
  det=dx*dy*da
```

```
    mseX=0
    mseP=0
    ALLOCATE(xtrue(box),xscale(box))
    OPEN(1,file=trim(xtrueFile),form='binary',IOSTAT=IOS)
    READ(1) xtrue
    CLOSE(1)
    xcnt=sum(xtrue)
    xscale(:)=x(:)*xcnt/sum(x)
    do ib=1,box
      if(xtrue(ib).ne.0.AND.xscale(ib).ne.0) then
        mseX=mseX+((xscale(ib)-xtrue(ib))*(xscale(ib)-xtrue(ib)))
      end if
    end do
    mseX=mseX/box
    do id=1,det
      if(proj(id).ne.0.AND.den(id).ne.0) then
        mseP=mseP+((den(id)-proj(id))*(den(id)-proj(id)))
      end if
    end do
    mseP=mseP/det
    OPEN(mseID,file=trim(mseFile),position='append')
    WRITE(mseID,*) mseX, mseP
    CLOSE(mseID)

  end subroutine calcMSE
```

Appendix B

TITAN-IR Input and Features

B.1 Reconstruction Input Block

The standard TITAN input file consists of input blocks for transport parameters, geometry, material distribution, source distribution, cross-section data, boundary conditions and tolerances, and SPECT parameters. A new input block was added to the TITAN-IR input file to allow the user to specify reconstruction parameters and is shown in Fig. B.1 with example parameters. The first keyword, *rectyp*, specifies the maximum number of iterations to be done and the number of subsets for OS-EM reconstruction. *phadim* contains the x, y, and z voxel dimensions of the reconstruction phantom. The *phadim* keyword matches the relevant dimensions of the system matrix, but does not have to match the dimensions of the TITAN phantom model. This allows for a more refined meshing in the SPECT simulation, which numerics may require for some cases, while maintaining

```
/*************************************************************************
#11  /Section 11 (Optional) : SPECT Reconstruction
/acceptable keywords: rectyp, phadim, measur, sysmat, recout, contra, filter
/ rectyp: number of iterations, number of OS-EM subsets
/ phadim: phantom dimensions, may be different from TITAN model
/ measur: measured data file name, NumOfEntry=3
/ sysmat: system matrix file name
/ recout: reconstruction output
/ contra: contrast calc parameters, lesion origin, base origin, radius (voxel units)
/ filter: filtyp (0=none,1=sinograms,2=post-reconstruction), filord, filcfq, unused variable
rectyp=5 8
phadim=64 64 32
measur=sino_320m.bin
sysmat=pm_jas.bin
recout=1
contra=6 39.77 18.54 16.00  47.54 32.00 16.00  39.77 45.46 16.00
         24.23 45.46 16.00  16.46 32.00 16.00  24.23 18.54 16.00
         32.00 32.00 16.00  1.827 2.288 2.748 3.655 4.576 5.468
filter=0 10 0.55 1
```

Figure B.1: Section 11 Block

a coarser system matrix and reconstruction image. The *phadim* dimensions must divide evenly into the TITAN phantom dimensions so that the reconstruction image can be expanded into the appropriate dimensions for the input source on the next iteration.

The *measur* and *sysmat* keywords give the file names of the measured projection data and system matrix, respectively. Note that the system matrix must be in the sparse matrix format described later in this appendix. The *recout* keyword allows the user to control which files are written out during reconstruction. A value of 0 will only write out the final reconstructed image, 1 will write out the reconstructed image after each iterations, and 2 will write out the reconstructed image and the sinogram after each iteration. Contrast can be calculated using the *contra* keyword as described in Section B.2. The sinograms or reconstructed images can also be filtered by using the *filter* keyword, which enables the use of a low-pass filter as described in Section 7.2. *Section 11* for SPECT recon-

struction can only be used if *Section 10* for SPECT simulation is also present in the input file.

B.2 Contrast

Contrast is important in determining if an observer can properly interpret the medical image and can assist in determining reconstruction convergence. The *contra* keyword allows the user to specify contrast calculations for a variable number of circular lesions. The first entry gives the number of lesions and is followed by the origin, in units of voxels, of each lesion. Next the origin of the reference background intensity is given and finally the radius, in units of voxels, corresponding to each lesion is listed. The reference background origin is used for calculating the contrast of all lesions, but the background region radius is adjusted to match the each lesion. The contrast is calculated using Eq. B.1

$$C_l = \frac{\bar{I}_l - \bar{I}_0}{\bar{I}_0} \tag{B.1}$$

where $\bar{I}_l$ is the average image intensity in a region of interest, e.g., a lesion, and $\bar{I}_0$ is the average reference background intensity, e.g., normal tissue. The largest reference background region is also used to estimate the background noise in the image. The contrast of each lesion and the background noise are printed out for every iteration.

B.3 Sparse System Matrix Format

The primary additional memory requirement from adding reconstruction to TITAN is the system matrix which has dimensions of the number of phantom voxels by the number of detector elements. Even for a small model this can become a very large matrix. For example, the 2-dimensional test case in Section 6.2.2 uses a 64 by 64 voxel phantom and 64 by 60 detector elements, which results in a 4096 by 3840 system matrix or about 1.57×10^7 values. By storing this matrix as a sparse matrix, the required memory was reduced from 62.9 MB to 3.6 MB.

A general system matrix can be converted to the sparse matrix format used by TITAN-IR using the following Fortran 90 code. For each detector element, $numvox$ specifies the number of corresponding non-zero phantom voxels, pos is the array of non-zero voxel positions, and aij is the array of system matrix values at the positions specified in pos.

```
module mProjMatrix
  implicit none
!Define proj matrix type for TITAN
  type sparseMatrix
    integer :: numvox
    integer*4, dimension(:), allocatable :: pos
    real, dimension(:), allocatable :: aij
  end type
  type(sparseMatrix), dimension(:), allocatable :: sysMatrix
end module mProjMatrix

program readPM
  use mProjMatrix
  implicit none

  integer :: seg_num, numv, dum
```

```
integer :: IOS, nbin, i, j, ix, iy, iz, idx
integer :: det, box, pix_det(2), phan_dim(3), num_ang
real, dimension(:), allocatable :: pbd
character (len=30) :: fileIn

write(*,*) 'Enter the phantom dimensions (x,y,z):'
read(*,*) phan_dim
write(*,*) 'Enter the detector dimensions (x,y,angles):'
read(*,*) pix_det, num_ang
write(*,*) 'File to be converted:'
read(*,*) fileIn

det=pix_det(1)*pix_det(2)*num_ang
box=phan_dim(1)*phan_dim(2)*phan_dim(3)
ALLOCATE(pm(det))
ALLOCATE(pbd(box))

OPEN(1,file=trim(fileIn),FORM='binary',IOSTAT=IOS)

DO j=1,det
  pbd(:)=0.0
  numv=0
  DO i=1,box
    READ(1) pbd (i)
    IF(pbd(i).GT.0) THEN
      numv=numv+1
    END IF
  END DO
  pm(j)%numvox=numv
  write(*,*) 'det:', j, ' numv:', numv
  ALLOCATE(pm(j)%pos(numv),pm(j)%aij(numv))
  dum=0
  DO iz=1,phan_dim(3)
    DO iy=1,phan_dim(2)
      DO ix=1,phan_dim(1)
        idx=((iz-1)*phan_dim(1)*phan_dim(2))+((iy-1)*phan_dim(1))+ix
        IF(pbd(idx).GT.0) THEN
          dum=dum+1
          pm(j)%pos(dum)=((phan_dim(3)-iz)*phan_dim(1)*phan_dim(2))+((iy-1)*phan_dim(1))-
          pm(j)%aij(dum)=pbd(idx)
        END IF
      END DO
    END DO
  END DO
END DO
CLOSE(1)

OPEN(1,file='sparse.bin',FORM='binary',IOSTAT=IOS)
DO j=1,det
  WRITE(1) pm(j)%numvox
  DO i=1,pm(j)%numvox
```

```
      WRITE(1) pm(j)%pos(i), pm(j)%aij(i)
    END DO
  END DO
  CLOSE(1)

  DEALLOCATE(pbd,pm)

end program readPM
```